Growth and Characterization of Thin Film Nanocrystalline Silicon Materials and Solar Cells

Solomon Nwabueze Agbo

Growth and Characterization of Thin Film Nanocrystalline Silicon Materials and Solar Cells

Proefschrift

ter verkrijging van de graad van doctor
aan de Technische Universiteit Delft,
op gezag van de Rector Magnificus prof. ir. K.C.A.M. Luyben,
voorzitter van het College voor Promoties,
in het openbaar te verdedigen

op dinsdag 27 maart 2012 om 10:00 uur

door

Solomon Nwabueze AGBO

Master of Science in Solar energy Physics
University of Nigeria, Nsukka

geboren te Nsukka, Nigeria.

Dit proefschrift is goedgekeurd door de promotor:
Prof. dr. M. Zeman

Copromotor Dr. R. A. C. M. M. van Swaaij

Samenstelling promotiecommissie:

Rector Magnificus,	voorzitter
Prof. dr. M. Zeman,	Technische Universiteit Delft, promotor
Dr. R.A.C.M.M. van Swaaij,	Technische Universiteit Delft, copromotor
Prof. dr. ir. W.M.M. Kessels,	Technische Universiteit Eindhoven
Prof. dr. B. Dam,	Technische Universiteit Delft
Prof. dr. R.E.I. Schropp,	Utrecht Universiteit
Prof. dr. eng. J.A. Ferreira,	Technische Universiteit Delft
Dr. F. Finger,	Institute for Energy (IEF-5), Forschungszentrum Jülich

This research work was financially supported by the Dutch Ministry of Foreign Affairs under the Netherlands Fellowship Programme (NFP) for development cooperation.

ISBN: 978-90-8570-985-5
Cover page image: nasaimages.org

Published and distributed by CPI, WÖhrmann PrintService, Zutphen, the Netherlands

This dissertation is dedicated to:

The almighty God by whom all things consist and to my wife Oge for being all she is to me

Contents

Chapter 1

Introduction

1.1 Photovoltaic technology and the current world energy scenario

Human life generally revolves around energy generation and utilization, which largely affects living standard. The current energy demand trend has shown that energy requirement to sustain human life and activities has always increased due to the increasing human population and modernization. According to the US Energy Information Administration, it is expected that world energy use which is put at 532 quadrillion kilojoule as at 2008 will increase by 53% in 2035 [1]. Generating sufficient energy to meet this growing demand has been of a major global concern. For most developing countries, the draw back in both economic and technological development can largely be attributed to the very limited and unsustainable energy supply.

Various energy sources are in use for energy generation. On a global scale, fossil fuel is the main energy source today that accounts for over 70% of the global energy consumption [2]. As shown in figure 1.1 [3], the dominance of fossil fuel in the world energy scenario still holds strongly. Fossil fuels are hydrocarbons, which are burnt to release energy. It is projected that other energy sources like wind, solar and biomass are going to play significant roles in the world energy mix in coming decades.

Energy generation from fossil fuel has not been without effects on human lives and on the environment. The burning of fossil fuel releases greenhouse gases into the atmosphere and these gases today are believed to account for global warming. Another major challenge with the use of fossil fuel is that it is only available in very few countries and as such has led to the dependence of many countries of the world on these few oil-producing countries. A direct consequence of this is the ever-existing political and economic tension between the oil-producing nations and the rest of the world. On another hand,

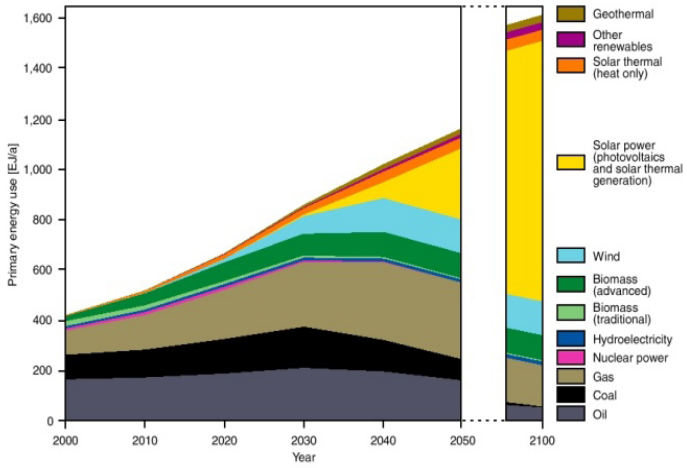

Figure 1.1: Current and projected world energy production scenario [3].

over-dependence on oil can be linked to the conspicuous under-development of some of the oil producing nations whose economic policies are mainly oil-based. Typical examples include countries like Nigeria and Libya. Energy generation from other energy sources such as nuclear energy and energy from coal also affect human life and the environment.

The current world energy scenario paints a picture of an energy supply system that is not sustainable, not reliable, not sufficient, not cost-effective, and not environmentally friendly. In view of this it is only imperative that both alternative and supplementary energy sources to the depleting fossil and nuclear sources are sought. This will be a long-term roadmap to emancipating this generation from its current energy crisis and securing a better environment and future for generations to come. Energy production from renewable sources is considered sustainable. Options such as solar and wind energy are environmentally friendly and can be harnessed in most parts of the world. Energy from the sun can be harnessed directly by a thermal conversion using solar collectors or by electrical conversion using solar cells or solar power concentrators. The direct conversion of solar energy into electricity in solar cells is based on photovoltaic (PV) effect.

Solar cells are semiconductor devices consisting of doped layers that are put together to form a p-n junction. On illumination by sunlight, charge carriers are generated. These carriers are separated so

that they do not recombine and are then collected via the electrodes of the cell. As of this day, photovoltaic accounts for less than 2% of the renewable energy make-up of the global energy production chain [2]. However, the PV industry has been experiencing a great boom since the wake of a global renewed interest in renewable energy within the last decade. The PV market production capacity has speedily grown and the prize also dropping; though still not comparable to the cost of energy from fossil fuel. Crystalline silicon-based solar panels account for over 90% of the PV industry [4]. The cost of this solar panels largely accrues from the material usage during production. A typical crystalline silicon solar cell for instance consists of about 200 micrometer thick silicon material.

A step towards making PV competitive in the current global energy scenario will result from reducing its production cost and in turn its market viability. It is in an effort to achieve this that has resulted to what is commonly called the second generation solar cell. Thin film photovoltaic technology makes up the second generation solar cells. As its name implies, it involves 'thinning' down on the amount of material used for solar cell production with the main aim of making PV cost-effective. Thin film silicon is one of the thin film solar cell technologies that are today being investigated and utilized for energy production.

Thin film-based solar cells have generally received a lot of attention in recent times and have been considered the most widespread alternative to bulk crystalline solar cell [5]. This interest is based on the low material consumption, the relatively low cost and large-area deposition possibilities at relatively low substrate temperature [5-7]. This low temperature deposition offers the possibility to produce flexible and light-weight solar panels which can be used to cover the roof of factory buildings for instance. Deposition at low temperature allows for the use of cost-effective substrate materials such as glass, stainless steel and plastic.

1.2 Thin Film Silicon

1.2.1 Hydrogenated amorphous silicon (a-Si:H)

In crystalline silicon, each silicon atom is covalently bonded to four neighbouring atoms. The bond length of all the bonds are equal and the angles between the bonds are also equal. This gives rise to a

regular atomic arrangement with a long-range order. In thin film amorphous silicon, there is no regular atomic arrangement over a long range. The deviations in bond angles and bond lengths between neighbouring atoms result in weak and strained bonds. The main defects are the so-called dangling bonds. Dangling bonds are silicon atoms that are bonded to only three silicon atoms and have an unpaired electron, hence are unsaturated [8]. By hydrogen incorporation into the amorphous silicon atomic network, the dangling bonds are passivated when the hydrogen atoms form bonds with the dangling silicon atoms. This way, the defect density in amorphous silicon is reduced hence making the material more useful for opto-electronic application.

Hydrogenated thin film amorphous silicon (a-Si:H) has been widely used as an absorber material in solar cells since its emergence in the mid 70s. The interest in a-Si:H is based on its high absorption coefficient in the visible range of the solar spectrum and low processing temperature hence the possibility of using low cost substrates [7, 9]. The high absorption profile stems from the inherent structural disorder and the associated defects/dangling bonds. The ability to hydrogenate and dope this material resulted in its application in other electronic technologies like transistors and sensors.

Today, one of the greatest challenges of research and development in thin film amorphous silicon is the Staebler-Wronski effect [10] observed with a-Si:H solar cells. It is the degradation in performance of the cell upon illumination which is attributed to the creation of additional metastable defects acting as trap/recombination centers in the absorber layer [11]. Research efforts in this regard have geared towards improved understanding of the mechanism of the process. Examples of such mechanisms include specific effects of hydrogen dilution, weak Si-Si bonds and Si-H bonds, and complexes in the creation of the defects [9]. Also research efforts are directed towards reducing the thickness of the film expected to result from improved light-trapping schemes into the solar cell [12]. By diluting the silane with hydrogen during the growth of the a-Si:H absorber layer, more stable devices have been made [13]. Thinner absorber layers (~ 250 nm) have also been used by incorporating light scattering schemes [14].

1.2.2 Hydrogenated nanocrystalline silicon (nc-Si:H)

Hydrogenated thin film nanocrystalline silicon (nc-Si:H) evolved as an off-shut of research in amorphous silicon. In the beginning, it was referred to as microcrystalline silicon (μc-Si:H) mainly because of the size of the crystal grains. However, research in μc-Si;H has evolved over time so also the name. Nomenclatures such as protocrystalline, polymorphous and nanocrystalline silicon are used variously depending on the size of the crystals and the growth phase of the material. In this thesis, we use the term 'nanocrystalline' as is most commonly used now. The crystal sizes in the films deposited for this work are indeed within the nano-scale in size. Nanocrystalline silicon film can be composed mainly of crystalline columns in films with high crystalline portion or as small crystal grains embedded in an amorphous matrix for films with low crystalline portion. Hence, nc-Si:H is often characterized in terms of the fraction of the film that is crystalline (crystalline mass fraction). In this thesis, we also refer to this as the *crystallinity*.

At a given hydrogen dilution during plasma enhanced chemical vapor deposition, the film growth evolves first from an amorphous incubation layer. From this phase, film growth further evolves to the nucleation phase through to the full crystalline regime. First μc-Si:H layers were deposited by Veprek and Marack [15]. In 1979 Usui and Kikichi [16] doped the first microcrystalline layer using strongly hydrogen-diluted silane in a plasma induced microcrystalization at a deposition rate of less than 10^{-3} nm/s.

1.2.3 Hydrogenated nanocrystalline silicon solar cell

The first substrate and superstrate-type solar cells of entirely thin film nanocrystalline layers with efficiency above 7% were made at the Université de Neuchâtel in 1996 [17]. Since then, research effort has been put into utilizing and optimizing the inherent advantages of this cell such as its stability against light-induced degradation and the extension of its spectral response to the near infrared light region. Today, thin film nanocrystalline solar cells are used as bottom cell in tandem and triple junction cells. In tandem cells, they are particularly used as the bottom cell to collect the less energetic photons transmitted through the top cell and to aid tunnel/recombination

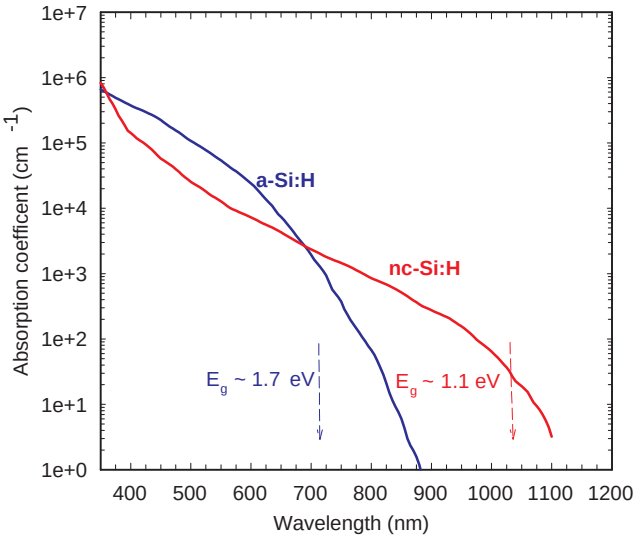

Figure 1.2: The absorption as a function of wavelength of thin film nanocrystalline silicon compared to that of a-Si:H. The band gaps, E_g, of the two materials are shown.

junctions that form the connection between individual cells. The absorption of the nc-Si:H material covers also the near infra red region of the solar spectrum (up to wavelengths of 1100 nm) and its band gap ($E_g \approx 1.1$ eV) make it a near-perfect match for amorphous silicon/nanocrystalline silicon tandem (micromorph) solar cell. Its low absorption at this spectral region (see figure 1.2) requires a relatively thick absorber layer and an efficient light trapping scheme for sufficient current generation to ensure current matching in the tandem cell.

Operation: A typical nc-Si:H solar cell just like an a-Si:H solar cell consists primarily of the intrinsic absorber layer sandwiched between a p- and n-doped layer. The solar radiation, which enters the solar cell from the p-layer, is absorbed in the intrinsic layer for the generation of electron-hole pairs that are subsequently separated and collected at the contacts of the solar cell. Carrier separation and collection is driven by the internal electric field within the absorber layer arising due to the built-in potential between the doped layers. This requires that both the lifetime and the drift length of the photo-generated carriers are

reasonably high within the absorber layer. Ideally, the drift length is longer than the thickness of the absorber layer for optimum performance. The electric field within the intrinsic layer depends on its material properties such as the mobility band gap, defect density distribution and thickness, and on the doping level and mobility band gaps of the doped layers [18]. Owing to the spatial distribution of defects within the solar cell and especially at the p-i and i-n interfaces, the electric field is non-uniform as it shows relatively higher values at the regions near the doped layers where the space charge density is also higher compared to the middle part of the i-layer.

Structural components: The main components of nc-Si:H solar cell include the p-layer, absorber layer, n-layer, and the external contacts. The p-layer serves as the window layer from where solar radiation gets to the active part of the solar cell. It transmits maximum available radiation to the absorber layer with minimal absorption within it. This role requires that the p-layer has a wide band gap, and is made as thin as possible so as to maintain low series resistance and further reduce the chances of absorption of the incident photons. The high conductivity ensures low series resistance and the high doping/charge makes for high electric field across the absorber layer. These features enhance the separation and collection of charge carriers generated in the absorber layer [19]. P-layer crystallinity is required to be reasonably high so that it can promote the nucleation of nanocrystalline i-layer deposited on it. The absorber layer is intrinsic and it is here that electron-hole pairs are generated. For the n-layer, a good conductivity is also required. Poor conductivity of the doped layers results mainly in low fill factor of the solar cell. In nanocrystalline silicon solar cell, a-Si:H is often used for the n-layer because it gives better results. Simulations (not shown) have also indicated that the properties of this layer have negligibly effect on nc-Si:H solar cell performance when compared with the p- and the i-layers.

Transparent conducting oxides (TCOs) are essential components of a solar cell. They play the role of electrical contacts to the solar cell and are also adapted for light trapping within the solar cell. TCOs are generally semiconductors with good electrical conductivity and high transparency in the visible spectrum [4]. The front TCO is textured to efficiently couple in light into the active layer of the solar cell via the p-layer. At the rear of the cell, the TCO is also used as a back contact and back reflector either alone or in

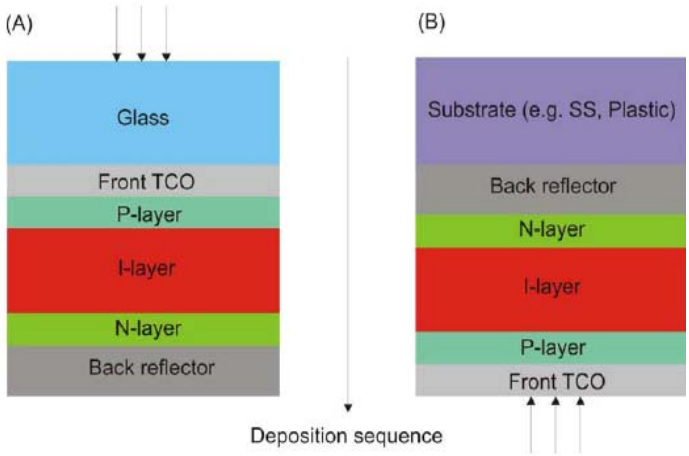

Figure 1.3: Schematic representation of the two solar cell configurations: (A) Superstrate Configuration, (B) Substrate Configuration.

combination with a metal (usually Al or Ag). Other properties of a good TCO include high carrier mobility, low contact and sheet resistance and high thermal, chemical and mechanical stability [20]. Commonly used TCOs include tin dioxide (SnO_2), indium-tin oxide (ITO) and zinc oxide (ZnO). Aluminium-doped zinc oxide (ZnO:Al) has gained wide interest because of its stability against hydrogen plasma. Current efforts in thinning down the thickness of both amorphous and nanocrystalline solar cells as a way of reducing both production cost and the degradation effect generally results in a decrease in short circuit current. This loss is compensated by effective light management schemes through the use of textured front TCOs. In tandem solar cells (e.g. micromorph), ZnO:Al is sometimes used between the top and bottom cells as an intermediate-reflector layer to enhance light absorption in the top a-Si:H solar cell.

Configuration: Nanocrystalline silicon solar cells just like amorphous silicon solar cells are deposited in two possible configurations: substrate and superstrate configurations. In the superstrate configuration, the substrate is usually a transparent glass on which a TCO layer is deposited as the front contact. The sequence of deposition (commonly abbreviated as p-i-n) is first the p-layer on the glass/TCO substrate, then the absorber layer, n-layer and the back contact/reflector. For the substrate configuration, the back reflector is

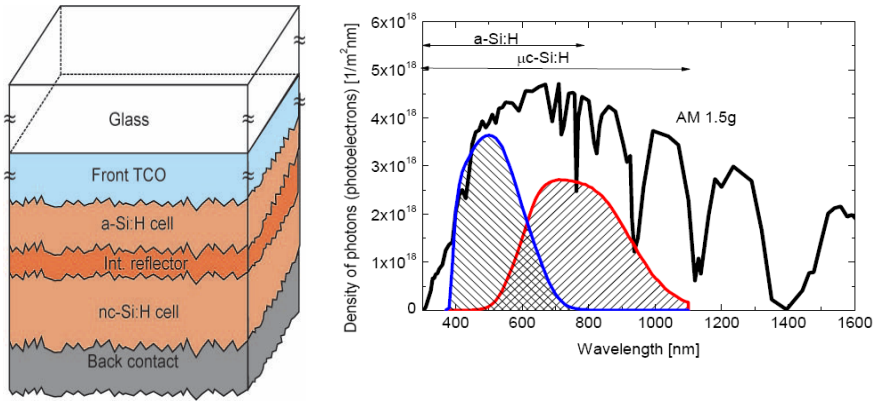

(a) (b)

Figure 1.4: Schematic of (a) the structure and (b) the spectral response of top a-Si:H cell and bottom nanocrystalline cell in a 'micromorph' tandem cell. Fig 1.4(b) is taken from Ref. [21].

deposited first on the substrate, which in this case does not need to be transparent, for example stainless steel, foil, or plastic. This configuration, commonly referred to as n-i-p follows the deposition sequence: substrate/back TCO/n-layer/i-layer/p-layer/front TCO. The nature of the substrate requires that the deposition temperature is maintained at a level that keeps the substrate mechanically and thermally stable. For both configurations as shown in Figure 1.3, light enters the solar cell through the p-layer.

Multiple junction application: A multi-junction solar cell is formed when two or more single junction cells are stacked together. With this device the conversion efficiency can be increased resulting from efficient utilization of the photon energy across the entire solar spectrum. Each solar cell that makes up the multi-junction stack is tailored to a specific part of the solar spectrum depending on the band gap of the material. Usually, the component with a higher band gap absorber serves as the top cell where it converts high energy photons. The lower band gap absorbers are tuned to cover the red and near infrared part of the solar spectrum. The overall open-circuit voltage in the stack is the sum of the open-circuit voltages of the individual solar cell since they are connected in series.

A tandem solar cell involves a stack of two solar cells. For a-Si:H based tandem, nc-Si:H and a-SiGe:H are most suited for the

bottom cell because of their band gaps. However, a-SiGe:H degrades on alloying with the associated poor optoelectronic properties. The use of nc-Si:H absorber layer for bottom cell with a-Si:H top cell in the so-called micromorph configuration (see Figure 1.4) has attracted so much interest since its introduction in 1994 by the IMT, Neuchâtel group [22]. This is because of the near-perfect coverage of the solar spectrum by the two solar cells and the stability of the bottom nc-Si:H. Since then, stabilized efficiencies of 12% have been reported [23-25]. Triple junction solar cells with the intrinsic layers comprising top amorphous silicon and two bottom nc-Si:H have been demonstrated to result in even higher stabilized conversion efficiency of 12.4% [26].

1.3 Material composition and characteristics of nc-Si:H

Nanocrystalline silicon is a mixed-phase material that is composed of columnar crystallites, amorphous fraction and voids (see Figure 1.5). The wide range of microstructures depends both on the deposition conditions [27] and on the substrate material [28]. Nanocrystalline silicon has an optical feature similar to c-Si. It has a lower absorption coefficient at the short wavelength spectral region (>1.7 eV) when compared to amorphous silicon. However, it absorbs energy from photons in the range 1.1 to 1.7 eV where a-Si:H shows a reduced response. This enhanced light absorption is partly attributed to the naturally textured surface of the nanocrystalline film surface [29] and mainly from a combined effect of its constituents namely the crystalline grains, the grain boundaries and the amorphous matrix.

The microstructure varies with the growth process which begins with or without the amorphous incubation layer depending on the deposition conditions and the substrate material. The growth evolves into the nanocrystalline phase consisting of crystals of varying sizes. The grain sizes depend on the level of hydrogen dilution during deposition. Grain sizes increase directly as the hydrogen dilution increases. Increasing hydrogen dilution beyond the amorphous-to-nanocrystalline transition results in large grain sizes with the associated voids and grain boundaries [30]. Nc-Si:H is structurally heterogeneous and contains amorphous component material having no long-range order. The randomly-oriented crystallites are embedded in columns where they exist together as conglomerates. Just as in a-Si:H, dangling bonds are present in nc-Si:H and substantially affect the performance of nc-Si:H solar cells in constituting carrier

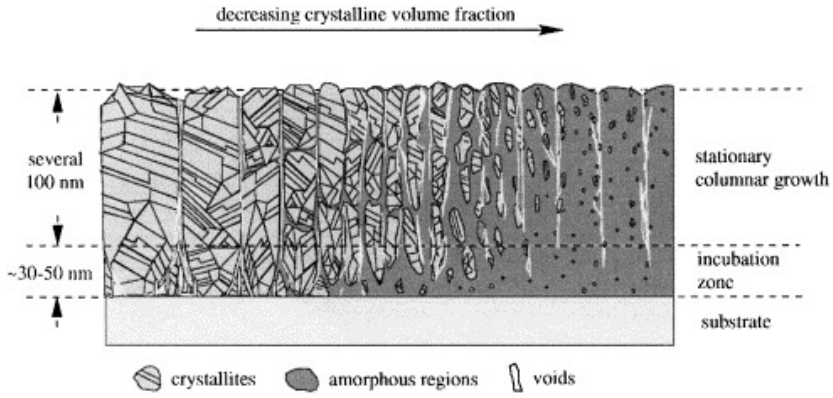

Figure 1.5: Structure of nanocrystalline silicon thin film showing the crystallites and voids embedded in amorphous matrix [23].

recombination points. Defects in nc-Si:H are located at the grain boundaries, in between the crystallites, in the amorphous matrix or at the surface [31-33]. Grain boundaries affect solar cell performance by impeding the flow of majority carriers, resulting in increase in series resistance. In addition, they provide shunt paths in the cell hence reducing the open-circuit voltage and the fill factor of the solar cell [29].

For application in solar cells, the crystalline mass fraction, f of nanocrystalline silicon is an essential material property, which also affects the optical as well as the electrical properties of the film. It expresses the percentage component of the film that is crystalline (see more details in section 2.3.6). The material quality is optimized at high crystalline mass fraction (above 50%) depending on the deposition conditions [23]. High crystalline mass fractions, however, are not absolutely a plus for nc-Si:H solar cell performance. With increased crystallinity also comes increased grain boundaries density and voids; all of which constitute defects and deteriorate solar cell performance. The onset of growth of nc-Si:H is critical. It nucleates on the underlying background depending on the substrate material and the deposition conditions. The need for high crystalline mass fraction in nc-Si:H is mostly important at this onset of growth as shall be shown in this thesis.

The electrical properties of intrinsic nc-Si:H layer are determined by the different constituents of the material. The different

transport properties of nc-Si:H constituents and the inhomogeneity of the microstructure account for the resultant complex electrical properties of the film. Generally, a high μτ-product (in which μ is the free-charge carrier mobility and τ the carrier lifetime) is a basic requirement for efficient carrier collection. Transport path of carriers in nc-Si:H can be co-planar or transverse depending on its structure. The transport is co-planar if the carriers move parallel to the substrate surface (i.e. perpendicular to the columnar grain boundaries) and transverse if carriers move perpendicular to the substrate surface (like in a solar cell) [29]. At the interfaces and grain boundaries the drift process is predominant while diffusion is the predominant mechanism within the grains [34].

1.4 Material properties of thin film nc-Si:H in relation to depth, composition and substrate material.

The material properties of nc-Si:H are very sensitive to the composition, i.e. the crystalline and amorphous mass fractions, and the void fraction. In turn, these fractions are determined by the deposition conditions and device grade (i.e. material with good opto-electronic property for device application) material is often obtained within a sensitive process window. The growth of nc-Si:H therefore requires a constant optimization and re-optimization of the deposition conditions. At a crystalline mass fraction in excess of 50%, many research groups have made high performance solar cells [29, 35, 36]. At the same time, at low crystalline mass fractions of about 30%, nanocrystalline solar cells with 9.8% efficiency [37] have also been made. These variations, which depend on the different deposition conditions, suggest that the optimal solar cell performance depend more on the employed deposition conditions. It is known [23, 36] that the best nanocrystalline solar cells are made around the so-called amorphous-to-nanocrystalline transition. Amorphous-to-nanocrystalline transition is a transition phase in the growth of nc-Si:H at which the growth evolves from amorphous phase into the crystalline phase [38]. Adapting deposition conditions to attaining this transition is therefore the basis for film growth optimization. The transition regime is a sensitive process window that is largely dependent on the hydrogen dilution and other deposition conditions. Nc-Si:H solar cells with absorber layers deposited at this transition have high open-circuit voltage values.

Often the crystalline mass fraction in nc-Si:H is determined from Raman measurement. The peaks in the Raman spectrum are deconvoluted into contributions from the amorphous and crystalline phases of the material. In most cases the determined crystalline mass fraction in nanocrystalline silicon solar cells only reflects the top 500-600 nm of the cell. This, however, only shows the crystallinity value when the film growth is in the crystalline regime as shall be shown in this work. Hence, the crystallinity profile and as such the full structural profile of the film is not known from the onset of growth. Growth of nanocrystalline silicon conventionally begins with the amorphous incubation layer. From here growth progresses to the full nanocrystalline regime where the crystallinity value saturates [39]. Collins et al [40, 41] has shown that the initial amorphous incubation layer arises due to the time lapse required to attain equilibrium between deposition and etching at the substrate interface. This insitu real time spectroscopic ellipsometry (RTSE) approach however, only relates the structural evolution in terms of surface roughness based on a number of theoretical assumptions. Because of the depth limitation of the laser used for Raman measurement this initial growth phases preceding the full crystalline regime are not investigated especially for film thickness higher than 1 micrometer. Even for high laser excitation wavelength of 647 nm as used by Mai et al [42], the whole crystallinity development profile is not captured.

Apart from using crystalline mass fraction as the most critical parameter by which nc-Si:H films are characterized, other properties such as the preferred (dominant) crystal orientation can relate to the material features and add further insight into the complex material nature of nc-Si:H. Various techniques have been used in order to investigate the preferred crystal orientation in nc-Si:H. X-ray diffraction (XRD) [43] for instance has been widely applied in investigating the crystal structure of nc-Si:H. Transmission electron microscopy (TEM) [28, 44] has been applied also to probe the material structure of nc-Si:H. Although well-established, TEM is destructive, time-consuming, and expensive. Similarly XRD is not a fast measurement and the obtained diffraction pattern can be easily affected by impurities. Analysis using a computer program to determine grain orientation from traces of crystallographic planes of any known indices has been used [45]. This approach is, however, limited in that it is time-consuming, tedious and often applied only to specific crystal plane. Raman spectroscopy on the other hand is a fast, non-destructive technique that has wide application in estimating the

degree of stress and disorder in thin-films [44, 46] and the crystalline mass fraction in nc-Si:H [47]. The use of Raman for predicting crystal orientation has been proposed and it is based on Raman intensity dependence on the directions of the polarization vectors of the incident light relative to the crystallographic axes [48, 49]. This, however, has not been demonstrated in nc-Si:H.

Nanocrystalline silicon is usually deposited directly on glass, especially for material characterization. In either substrate or superstrate configuration, nc-Si:H solar cell active films are deposited on glass with either a transparent conductive oxide or another silicon layer. For infrared spectroscopy measurement, films are deposited directly on crystalline silicon wafers. The effect of these different underlying substrates on the growth profile of nc-Si:H is still an open question. Collins et al [40, 41] and Fujiwara et al [50] have used RTSE to show the dependence of film surface roughness development on film thickness. Using phase diagrams they showed the transition from amorphous to the microcrystalline phase for different hydrogen dilution. Though they showed the various evolution phases in the growth of nc-Si, there was no direct comparison to the crystallinity development as determined from Raman measurement. By the use of highly crystalline nc-Si:H seed layers, crystal nucleation on different substrates and film uniformity has been shown to be enhanced [51, 52]. However, it is still not clear how the crystallinity development profile in nc-Si:H is affected by the underlying substrate.

1.5 Motivation and outline of this thesis

Hydrogenated thin film nanocrystalline silicon is an attractive material for solar cell application. It is currently being used as bottom cell in a-Si:H/nc-Si:H tandem cells to develop a stable and efficient device. Nc-Si:H is a complex mixed-phase material. Its material properties are known to vary depending on the deposition conditions. Because of these, the understanding of its growth mechanism and the material properties has been diversely interpreted and has remained a research issue. The work reported in this thesis therefore is aimed at understanding better the growth mechanism and characteristics of nc-Si:H and how they affect nc-Si:H solar cell performance.

Nanocrystalline silicon can be deposited using radio frequency plasma enhanced chemical vapor deposition (rf PECVD). The main advantage of this deposition technique is its ease of adaptation for

industrial purposes, having been well developed over the years. For the growth of nc-Si:H in conventional rf PECVD, often the silane precursor gas is highly diluted with hydrogen. Apart from the hydrogen dilution, virtually all the other deposition parameters such as deposition power, deposition pressure and electrode distance affect the growth of nc-Si:H and its material properties. This has resulted in a sensitive process window for the growth of device grade film especially for rf PECVD nc-Si:H films grown under high pressure-high power condition.

The first step towards optimization of nc-Si:H is to relate the effect of the deposition parameters on the material properties and then obtain the process window. As a first step in this work, we optimized the deposition conditions for the growth of nc-Si:H. We then present a correlation between deposition parameters, film properties and device characteristics. The main material property that determines the device nature of nc-Si:H is its crystalline mass fraction. In this work, we have used this parameter for comparing nc-Si:H films.

Thin film nc-Si:H is a mixed-phase heterogeneous material. Its complex composition has made its microstructure investigation also complex. Because its growth evolves through various phases and stages, material characteristics are also depth-dependent. However, most structural characterization tools do not take this into account and instead assume nc-Si:H to be wholly or largely crystalline without relating to its depth-dependence. We therefore propose a simple approach using depth-profile Raman spectroscopy to investigate ex-situ the complex phase changes in nc-Si:H growth. By means of depth-profile Raman measurement, we demonstrate that the growth phases can be determined and the crystallinity development profile established.

The growth of nc-Si:H under conventional rf-PECVD begins with the amorphous silicon incubation layer. This layer limits the performance of nc-Si:H solar cell. The solar cell performance drops as a result of charge carrier extraction problem due to the interface with the incubation layer leading to low spectral response in the blue region. A seeding technique is applied in this work to suppress the amorphous incubation layer and in turn control the initial growth phase of nc-Si:H. The effect of this on the nc-Si:H crystallinity development profile and on solar cell performance is presented.

Nc-Si:H is usually grown directly on transparent glass substrate for optical and electrical characterization. For a nc-Si:H solar cell in superstrate configuration the substrate is glass with textured

TCO. These materials grown on different substrates show different material properties and this makes comparison of material properties of these films difficult. Again, till date not much investigation has been done on the effect of different substrates on the crystallinity development profile of nc-Si:H. This is presented in this work and it is shown that substrate effect on crystallinity development in nc-Si:H can reduced by seeding.

Preferred orientation of crystals can be used to characterize growth processes in nc-Si:H. Since each grain has its features and orientation, preferred orientation indicates the dominant orientation in the film. It gives an understanding of the growth process since different deposition parameters stimulate the growth of different crystal orientation in varying degrees. Determining preferred orientation in nc-Si:H is therefore important and is mainly done by x-ray diffraction spectroscopy (XRD). In this thesis, a new possible approach using Polarized Raman Spectroscopy (PRS) to determine preferred orientation of crystals in nc-Si:H is reported.

The outline of this thesis is as follows. In chapter 2 we discuss the deposition facilities used for the growth of our films and the techniques used for their characterization. In chapter 3 the material properties of nc-Si:H films as affected by the following rf PECVD parameters: deposition power, deposition pressure, substrate temperature, and silane concentration are investigated. The aim is to obtain the optimal process window and to verify the sensitivity of nc-Si:H material properties and the a-Si:H/nc-Si:H transition on rf PECVD parameters. Chapter 4 discusses the effect of amorphous silicon incubation layer on the growth of thin film nanocrystalline and how this can be reduced by seeding. Seeding technique is implemented in nanocrystalline silicon solar cells in both substrate and superstrate configuration. The following chapter (chapter 5) shows how different substrates affect the crystallinity development in nanocrystalline silicon. It is further presented that with the use of a seed layer the substrate effect can be neutralized. The use of Raman technique for determining preferred crystal orientation in thin film nanocrystalline silicon is discussed in chapter 6. The general conclusions and recommendations for future work is summarized in chapter 7.

1.6 Contribution of this work to the research field

The main aim of the work reported here is to investigate the effect of rf PECVD deposition parameters on the material properties of nc-Si:H and its device performance. Particular attention was paid to investigating the growth evolution of nc-Si:H. This was carried out using depth profile Raman measurement. This measurement gives the development in crystalline mass fraction in growth direction and was related to different growth phases in the material. This way we are able to observe the different growth phases of nc-Si:H on different underlying substrates. By using seeding technique, the crystallinity profile is modified and the effect of the underlying substrate is reduced. We show that this can improve material quality and in turn enhanced solar cell performance. In addition to using Raman spectroscopy to evaluate the crystalline mass fraction, we propose a method that uses Raman spectroscopy to deduce the preferred orientation of crystals in nc-Si:H. The results are summarized below:

- We have extended the knowledge of relationship between nc-Si:H material properties and the deposition conditions. In doing this, we have shown that
  - Transient depletion of SiH_4 during rf PECVD growth of nc-Si:H decreases the blue spectral response of nc-Si:H. This effect is reduced by proper timing of the gas inlet into the reactor chamber (see section 3.4.3).
  - Materials deposited at the amorphous-to-nanocrystalline transition under different deposition settings can have similar crystalline mass fraction but different electrical properties.
  - Use of Raman to predict preferred orientation of crystals in nc-Si:H (see chapter 6).

- We have demonstrated that the growth evolution profile of nc-Si:H can be favorably modified not only by manipulating the sensitive process window, but also by seeding. By using seed layers, our results show:
  - Nc-Si:H growth without the amorphous incubation layer (see sections 4.3).
  - A modification of the nc-Si:H growth profile such that crystallinity development is rapid and starts from the onset

of growth. This results in increased nc-Si:H solar cell performance (see chapter 4).

- Reduction of substrate effect on crystallinity development in nc-Si:H (see chapter 5).
- Raman depth profiling clearly shows the different phase changes during the growth of nc-Si:H on different substrates and how they can be manipulated by seeding (see section 4.3.3 and section 5.3.1).

2 Chapter 2

Experimental procedure and details

2.1 Thin film nc-Si:H deposition by radio frequency plasma enhanced chemical vapor deposition (rf PECVD)

Several methods used for thin film silicon growth can be physical vapor deposition, chemical vapor deposition, electrochemical deposition, or a combination of techniques. The most commonly used approach for both thin film amorphous and nanocrystalline silicon growth is the chemical vapor deposition (CVD). By this method, nc-Si:H or the a-Si:H layer is obtained from a reaction involving the dissociation of the silicon-bearing compound and the subsequent diffusion of the species to the substrate. This gas and substrate-surface reactions are controlled by deposition parameters such as the gas composition, flows and pressure, power density and frequency, and substrate temperature [9, 53, 54]. Physical vapor deposition involves the condensation of a vaporized form of the material onto a substrate surface. Various forms of this method include sputtering, pulsed laser deposition, etc. This chapter will be limited to radio frequency (13.56 MHz) plasma enhanced chemical vapor deposition (rf PECVD) as this is the technique used for the growth of nc-Si:H materials and devices reported in this thesis. The techniques used for the deposition of ZnO:Al TCOs and the metal contacts are also discussed.

The radio-frequency plasma enhanced CVD (rf PECVD) is used both for industrial and laboratory scale solar cell production [5, 55, 56]. The inherent advantages in this process include its adaptation for making device-grade material, large area deposition [57] and low temperature synthesis of materials. A typical rf PECVD set-up as shown in Figure 2.1 has two parallel electrodes; the anode, which is grounded and on which the substrate is placed, and the cathode by which the rf power is fed to the plasma [58]. The rf signal provides the energy by which the decomposition of the silicon-bearing gas (e.g. SiH_4) is effected and in this way generate the plasma. The radicals that are considered the most active species for nc-Si:H and a-Si:H layer

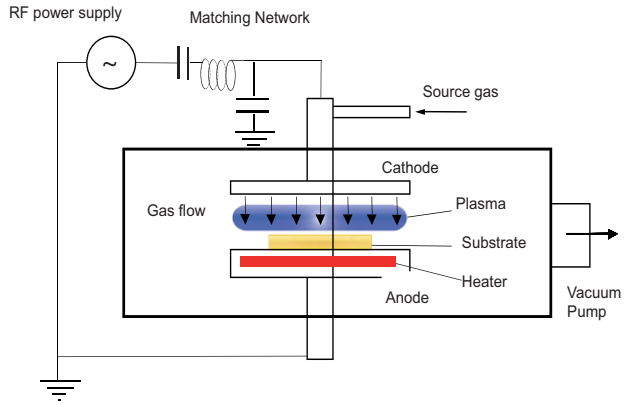

Figure 2.1: A typical rf PECVD set-up for nanocrystalline silicon deposition

growth, diffuse to the growing film surface and are involved in surface reactions. Low lifetime radicals, higher silane radicals (Si_2H_5, Si_3H_8, etc), and reactive radicals (SiH_2, SiH) are not good for the growth of device-grade material [29] and these are generated under increased deposition power. Even though the deposition rate is increased with increasing deposition power, the powder formation which leads to poor quality films is associated with this regime. SiH_3 (considered most relevant for good quality film) has the least reaction rate among the Si-H radicals and as a result lower electron temperature is preferred to enhance the formation of SiH_3 radicals and at the same time suppress the growth of SiH_2 to which material degradation has been associated [59].

The general approach for the growth of nc-Si:H layers involves using a silane-hydrogen gas mixture as a source gas under regulated substrate temperature, chamber pressure, rf power, deposition time and electrode distance. The doped layers (p- and n-) are obtained by introducing a suitable flow of boron-yielding gas (e.g. B_2H_6) and phosphorous-yielding gas (e.g. PH_3) respectively. The material and opto-electrical properties of the films and the resulting solar cells derive from these deposition parameters.

The materials reported in this thesis (except the doped layers) have been deposited at high pressure and using high power density as in the so-called high pressure depletion regime (HPD) [60, 61]. The high power density generates a high density of growth species, leading to a high growth rate. However, this would also lead to ion

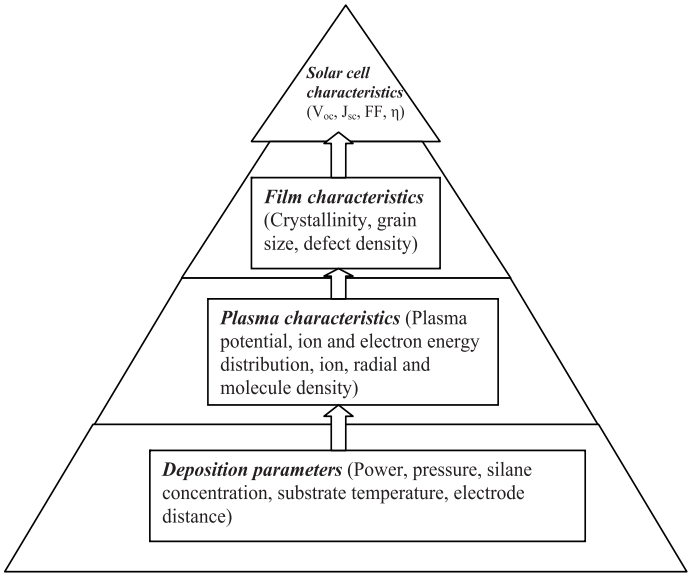

Figure 2.2: Correlation between deposition parameters and the solar cell characteristics.

bombardment with relatively high energy resulting to a high defect density. A high pressure is therefore used to suppress the ion energy. Increase in deposition pressure reduces the atomic hydrogen density in the plasma due to the so-called annihilation reaction in which hydrogen atom reacts with silane to form silyl radical and a molecule of hydrogen ($H + SiH_4 \rightarrow SiH_3 + H_2$) [29]. Here, higher pressures ($\geq$ 13.3 mbar) and silane depletion conditions both in connection with rf plasma are used for growth of nc-Si:H films. These configurations have yielded nanocrystalline solar cells of efficiency close to 9% at a deposition rate of 1.0 nm/s [36, 62]. Under low pressure conditions (~1.3 mbar), increasing discharge power deteriorates both film crystallinity and solar cell performance. These have been attributed to the high-energy bombardment of ionic species as a result of higher electron temperature [63, 60]. Under the high power regime as used in HPD, silane is efficiently decomposed, thus hydrogen annihilation reaction is suppressed [64]. Associated problems in this regime however include powder (polysilane) formation, high gas consumption especially hydrogen and high plasma excitation powers needed for large area growth [5, 36].

The main properties of nc-Si:H that determine its device nature include the crystallinity, grain size, and the defect density. In turn these properties determine the solar-cell performance as shown in figure 2.2. The process parameters are key to the growth of nc-Si:H films and their manipulation for example in going from a high to a low pressure can shift the growth transition from amorphous into the crystalline regime. A brief summary of the key rf PECVD parameters investigated in this work is as follows:

- *Silane concentration*, S_c: This is the ratio of the flow rate of silane to the sum of the flow rate of silane and hydrogen expressed as:

$$S_c(\%) = \frac{SiH_4}{SiH_4 + H_2} \cdot 100\% \qquad (2.1)$$

  Earlier reports [23, 53, 54] have shown that S_c is one of the most critical parameters that are tuned in order to grow thin film nc-Si:H. Usually, at low silane concentration, film growth is in the crystalline regime. Progressive increase in S_c decreases film crystallinity until it goes through the amorphous-to-nanocrystaline transition into the amorphous phase. Amorphous-to-nanocrystalline transition is known to have a high sensitivity to changes in S_c and has been of research interest because high grade nc-Si:H are deposited at this regime [36].

- *Deposition power*: The plasma excitation power affects the dissociation rate of silane. At high power the dissociation rate increases leading to high growth rate. Increase in deposition power while keeping other deposition conditions fixed leads to increase in the crystalline mass fraction of the deposited nc-Si:H film. The disadvantage of employing high power for nc-Si:H growth is the high ion bombardment of the growing film, which deteriorates film quality.

- *Deposition pressure*: The deposition pressure determines the collision probability of the colliding gas molecules [65]. At high pressure the ion energy is reduced hence the ion bombardment effect on the growing film surface is also reduced. High pressure leads to high growth rate. Except otherwise stated, for all the films

reported here, the deposition pressure was 2.5 mbar for the p-layers and between 7 and 12 mbar for the i-layers.

- *Substrate temperature*: The heating of the substrate influences the possible diffusion of the growth species at the growing surface and/or the relaxation of the silicon network in the bulk of the film. From the view point of reducing heating cost and the possibility to use flexible substrates, depositions are done at moderate temperatures ($\leq 200\ ^{o}C$).

2.1.1 The AMOR Deposition set-up

The radio frequency plasma enhanced chemical vapor deposition (rf PECVD) set-up, AMOR (the in-house name given to the rf-PECVD set-up at the Photovoltaic Materials and Devices group of the Delft University of Technology) was used for the deposition of all nc-Si:H materials and devices reported in this thesis. It consists of a cluster of four deposition chambers ($MPZ_{1\text{-}4}$) attached to a central transport chamber fitted with a robotic arm for the transport of samples in and out of the chambers as shown in figure 2.3. Each deposition chamber is designated for specific material growth and has capacitively-coupled parallel electrodes to which an rf generator source is connected. The rf generator generates an alternating current that sets up an electric field between the two electrodes; the electric field in turn accelerates and energizes the electrons for plasma generation by impact dissociation of silane. In order to keep the chambers in vacuum a turbo molecular pump backed up by a fore-line pump is connected. The flow of gases into the process chambers are controlled by the mass flow controllers (MFCs). An MFC is fitted with a throttling valve which adjusts its position so as to attain set flow values in the mass flow control unit.

The deposition chambers generally share similar features in terms of their configuration. Therefore, we shall present below only the details of the configuration of MPZ_4 where all the intrinsic nanocrystalline silicon films are deposited. The reactor volume V_r, has a capacity of 8 litres as it measures 20 cm × 20 cm × 20 cm. However, the heater well, the electrodes and rails reduce this volume to approximately 7 litres. The electrodes measure 12 cm × 12 cm and are separated by a distance of 8 mm, making a plasma zone of volume:

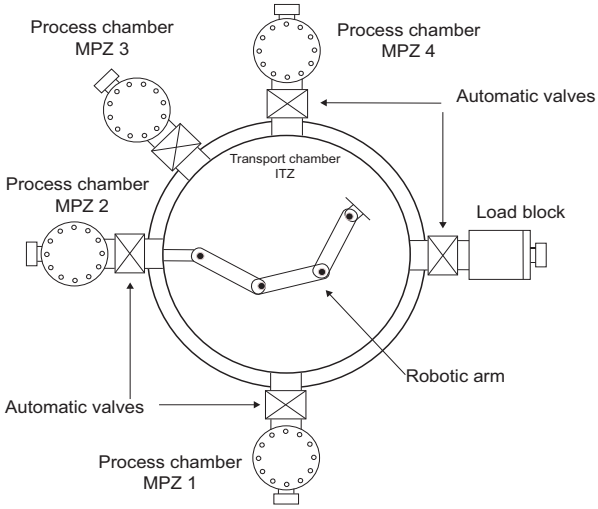

Figure 2.3: Schematic view of AMOR deposition set-up

12 cm × 12 cm × 0.8 cm = 115.2 cm^3. Even though this electrode distance is adjustable, this distance was fixed for all the experiments reported in this thesis except otherwise stated. The lower electrode has a shower head with holes at a pitch of 10 mm and a diameter of 0.5 mm. Gas flows through these holes into the processing zone. Due to the piping, chamber geometry, and the pumping arrangement the response time of the mass flow controllers was estimated to be about 60 s. By means of a butterfly valve in the pump line the pressure in the reactor was regulated. An electric heater with temperature set at 305 ^{o}C maintained the substrate temperature at 180 ^{o}C. For all depositions in this chamber, the hydrogen flow remained fixed at 150 sccm while the silane flow varied between 1.8 and 2.5 sccm.

2.2 Deposition of TCOs and metal contacts

The front contact of the solar cells used in this research are in-house sputtered ZnO:Al except otherwise stated. Sputtering involves the forceful ejection of a substance from a target unto a substrate after bombarding the target with the ions from a plasma. The deposition of ZnO:Al for our research was done using radio frequency magnetron sputtering. This is a multi-target system manufactured by Kurt J. Lesker. The system is composed mainly of a vacuum deposition chamber with a loadlock. The chamber has torus positions for four

targets. The source target for our deposition is a 7-inch ZnO ceramic target with 2% Al_2O_3 . The rf power source creates the plasma from Ar gas flow and the ions are directed to the target so as to release free atoms from the target to the Corning glass (E2000) substrate. As-deposited ZnO:Al has low roughness, hence the deposited ZnO:Al are wet-etched in 0.5% HCl in order to increase its roughness for improved light scattering in solar cells.

The Al and Ag metal contacts used either on single nc-Si:H layers (for electrical characterization) or as back contacts in nc-Si:H solar cell are evaporated. The Ag back contact is deposited using PROVAC (Pro 500 S) evaporator. This is a thermal evaporation process in which Ag pellets contained in a boat are heated up by passing current through it. The Ag pellets upon heating evaporate to the substrate. Al contact is also deposited in the same set-up by a similar approach except that in the case of Al, the Al target is bombarded with electrons released from a charged tungsten filament and accelerated towards the target by a magnetic field. The high energy from the electron beam heat up the Al target and thus causing the evaporation of Al atoms unto the substrate. Both depositions are carried out in vacuum.

2.3 Thin film nc-Si:H material characterizations

2.3.1 Reflection-Transmission (RT) measurement

The reflection-transmission measurement is an important technique for the evaluation of optical properties of thin films grown on a transparent substrate. For this purpose, a mini-RT set-up consisting of a 50 W halogen lamp, a SPEX 1680B monochromator and filters has been used. The specular part of the reflected light (R) and that of the transmitted light (T) are measured both on the same spot by two separate photodiodes on illuminating the samples perpendicular to the film surface. The absorptance, (A) is determined from the relation: $A = 1 - T - R$. The measurement data are further processed using opta 3.0 for the extraction of the optical-related properties of the film such as the film thickness, the refractive index and the extinction coefficient, and the absorption coefficient. From the absorption coefficient, the optical band gap is determined. More details of the physical concepts implemented in opta 3.0 are described in Klazes et al [66].

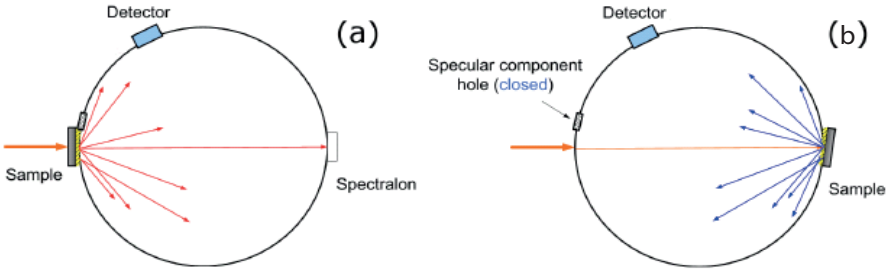

Figure 2.4: Total integrating sphere configuration for (a) total transmittance and (b) total reflectance measurements.

The band gap refers to the energy gap between the top of the valence band and the base of the conduction band. In a-Si:H, the concept of mobility gap is used due to the presence of localized tail states within the conduction and valence bands. The optical parameters are related as shown in equation 2.2. Here, α, hv, n, and E_g are the absorption coefficient, photon energy, refractive index, and the optical band gap respectively. p and q are parameters that determine the shape of the band edges. Tauc band gap [67] is obtained from equation (2.2) on assumption of parabolic band edges ($p = q = ½$). For $p = q = 1$, linear band edges are assumed and this gives the Klazes band gap. Compared to c-Si, nc-Si:H has higher absorption coefficient at high photon energy. This has been attributed to the higher absorption of the a-Si:H fraction that forms part of nc-Si:H [68].

$$(\alpha n h v)^{\frac{1}{p+q+1}} = (hv - E_g) \qquad (2.2)$$

One major limitation of the mini-RT is its inability to measure the diffused components of the transmitted and reflected lights and its limited spectral range to between 375 and 1060 nm. The diffused components of R and T are especially important for films deposited on a rough substrate, e.g. texture-etched zinc oxide. The mini-RT has been used mainly to extract the optical-related properties of thin film silicon. However, for films deposited on textured substrates in which the haze parameters are required the Perkin-Elmer Lambda 950 UV-VIS spectrometer was used. Its main component is the total integrating sphere (TIS) which makes it possible to measure total transmitted and reflected light. It has a deuterium arc lamp and a

tungsten-halogen lamp which enables it to measure in the wavelength range between 175 and 3300 nm. In figure 2.4 the system configuration is shown for total transmittance and reflectance measurements.

2.3.2 X-ray diffraction (XRD)

In order to investigate the structural features of nc-Si:H, x-ray diffraction analyses were carried out. This gives information about the crystal structure such as the crystal sizes and orientation, bi-axial lattice stress and micro-strain. The XRD measurements presented in this thesis were carried out at the New Technologies Research Centre, University of West Bohemia, 306 14 Plzen, Czech Republic using an automatic powder diffractometer X'pert Pro with a thin film attachment (parallel beam, asymmetric geometry, fixed incident angle ω, 2θ-scan) and a proportional detector. Copper Kα (Cu-Kα) characteristic radiation ($\lambda = 0.154$ nm) was used.

The XRD patterns were recorded using an asymmetric geometry because the penetration depth of Cu-Kα into nc-Si:H is much more than the thickness of the films. This way the volume of material that is probed is kept constant. The angle of incidence was fixed to 0.5 deg and the detector moved with a constant step of 0.05 deg from 10 to 65 deg on the 2ϑ scale. The counting time was 20 seconds per step and the irradiated area of the sample was 15 mm × 15 mm. Due to the asymmetric geometry of the experiment with a fixed incident x-ray beam, the lattice planes where a Bragg condition is fulfilled are not parallel to the sample surface, but they are inclined to the sample surface about $\theta - \omega$ degrees.

The ceramic alumina from NIST (National Institute of Standards and Technology) was used as instrumental standard. The position, height, integrated intensity and full width at half maximum (FWHM) are the main four parameters that characterize the diffraction lines. The broadening of a diffraction line is a result of a micro-structural change that can relate to the size of the crystallites and the micro-strains. The initial processing of the XRD patterns that includes background determination and subtraction was done using the X'pert HighScore plus software. A procedure utilizing the integral breadth of a diffraction line for determining the average size of the ordered domains and micro-strains was used. This procedure is based on a

Voigt function applied to the breadths of the diffraction line as proposed by Langford [69, 70]. Eq. (2.3) defines the integral breadth, β, and includes two parameters namely the height, I_0 , and the integrated intensity, I_{int} , of the diffraction line.

$$\beta = \frac{I_{\text{int}}}{I_0} \tag{2.3}$$

This procedure can only be used for symmetric line profiles.

The instrumental resolution of the equipment was taken into account in order to obtain a physical component of the broadening of the diffraction line. The reference measurement of the alumina powder from National Institute for Standard and Technology (NIST) was used for this correction. The physical component of the integral breadth of the diffraction line was then de-convoluted into a Cauchy part β_C^f , and a Gaussian part β_G^f , which represent the size of the diffracting domains and the micro-strains, respectively. The average size of the ordered domains and micro-strains were determined using equations 2.4 and 2.5, respectively [71, 72]:

$$\langle D \rangle = \frac{\lambda}{\beta_C^f \cos(\theta)}, \tag{2.4}$$

where $\langle D \rangle$ is the average domain size in the direction perpendicular to the diffracting lattice planes, λ is the x-ray wavelength and θ is the Bragg's angle.

$$\langle \varepsilon \rangle = \frac{\beta_G^f}{4\tan(\theta)}, \tag{2.5}$$

Here, $\langle \varepsilon \rangle$ is the average micro-strain in the diffracting volume which are residual short-range deformations and can be evaluated from the broadening of the diffraction line.

.

2.3.3 Transmission Electron Microscopy (TEM)

High resolution transmission electron microscopy (HRTEM) is a well-established technique for investigating the structure of materials. In thin film nc-Si;H, HRTEM can reveal the different phase materials that make up the film. In HRTEM individual grains that make up the film can be isolated and their sizes and orientations estimated. The HRTEM measurements were carried out at the Kavli Institute of Nanoscience of the Delft University of Technology. A FEI Tecnai F20ST/STEM transmission electron microscope was used for imaging. Cross sections of the samples were prepared by gluing a protective glass on the deposited film and cutting a cross section of thickness ~0.5 mm. Mechanical grinding and polishing of the cross section to ~10 μm and a subsequent thinning down to electron transparency with a Gatan Ar ion mill PIPS model 691 followed. Bright and dark field images were taken as well as lattice images (HREM images) without any objective aperture. Fast Fourier Transforms (FFTs) of the HREM images was carried out. Since bright and dark field contrast of the same grain changes a lot in the growth direction because of defects and bending of the TEM foil, only the grain diameter parallel to the substrate interface was determined.

2.3.4 Atomic Force Microscopy (AFM)

Atomic force microscopy (AFM) is a high resolution surface scanning microscopy used to investigate the morphology of surfaces. The system consists of a cantilever to which a point probe or scanning tip is attached as schematically shown in figure 2.5. When the tip is brought near the sample surface the force between the tip and sample surface creates a deflection of the cantilever. Hence in line with Hooke's law the force is dependent on the stiffness of the cantilever and on the distance between the probe and the sample surface. The deflection is measured using a laser spot reflected from the top surface of the cantilever into an array of photodiodes. For all the scans reported here, the NT-MDT NTEGRA AFM is used in a semi-contact mode. In this mode the tip of the cantilever does not make a continuous contact with the sample surface but rather makes contact intermittently with the surface.

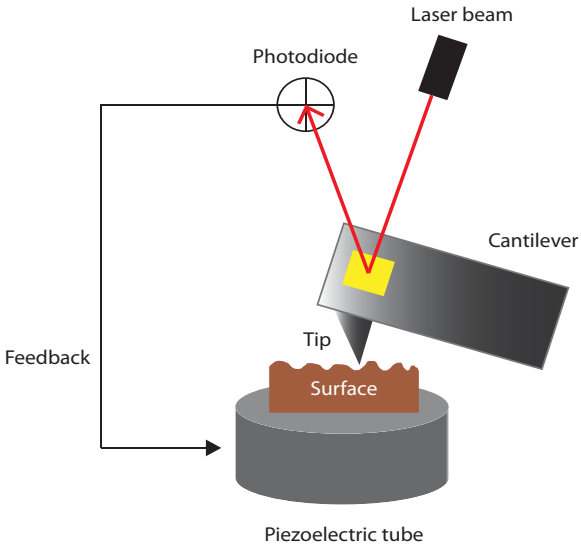

Figure 2.5: A typical AFM operational schematics showing the different components.

The cantilever is driven to oscillate at a frequency close to its resonance frequency by a small piezoelectric element with amplitude of oscillation between 100 to 200 nm. The piezoelectric feedback system controls the vertical displacement of the sample thereby ensuring that a constant force is maintained on the tip. The vertical movement of the tip follows the sample surface morphology and together with the x- and y- coordinates produces a 3D image of the probed surface. From the generated 3D images, the surface properties are obtained. Using the NT-MDT NOVA software the 3D scan images are processed to obtain the root mean square roughness, σ_{rms} from the relation:

$$\sigma_{rms} = \sqrt{\frac{1}{N}\sum_{i=1}^{N}(z_i - \tilde{z})^2} \qquad (2.6)$$

Here, N is the number of data points. z and ź represent the i^{th} position and the average surface level respectively.

2.3.5 Dark conductivity and activation energy measurement

For determining the electrical properties of our nc-Si:H samples under no illumination, the dark conductivity and the activation energy measurements are taken. Single layers of nc-Si:H films were measured using a home-built set-up consisting mainly of a temptronics stage, the probes and 617 Keithley voltage sources. The samples are deposited on Corning (E2000) glass and had two coplanar 300 nm thick aluminium electrodes of length 20 mm each separated by a gap of 5 mm. Before each measurement, the samples are annealed in air with the contacts in oven for 30 minutes at a temperature of 130 ^{o}C. Usually, a voltage in the range -100 to 100V is applied resulting in a current generation, I which relates to the dark conductivity, σ_d as:

$$\sigma_d = \frac{dI}{tlV} \qquad (2.7)$$

where d is the gap between the two electrodes, t is the thickness of the film and l the length of the electrodes. V is the applied voltage.

To determine the activation energy, E_a a temperature-dependent dark current-voltage measurement is performed. The activation energy gives indication of the level of conductivity in nc-Si:H. It is a measure of the energy gap between the Fermi level and the bottom of the conduction band (for n-type materials) or the top of the valence band (for p-type materials) and is expressed in the Arrhenius equation as [11] :

$$\sigma_d(T) = \sigma_0 \exp^{(\frac{-E_a}{KT})} \qquad (2.8)$$

Here, k is the Boltzmann constant, T the absolute temperature and σ_0 is the dark conductivity prefactor. Note that this simplified approach to determining the activation energy of nc-Si:H does not truly reflect the transport properties of nc-Si:H. This is because the effects of the many grain boundaries and the large number density of small crystallites with a distribution of crystallite sizes are not accounted for [73].

2.3.6 Raman spectroscopy

Theoretical background and system description

The Raman effect was first discovered by Chandreshra V. Raman in 1928 [74]. Raman spectroscopy is a fundamental method by which the structure and composition of materials are probed. It is based on the fact that light scattered in-elastically on interaction with a molecule reveals the characteristic nature of the molecule. For elastically scattered light the incident photons have the same energy (frequency) as the scattered photons and this is the case for most of the scattering observed. A small fraction of the scattered photons will have an energy that is different from the energy of the incident photon. This energy change induced by the Raman effect in materials is represented graphically in a plot of the Raman signal intensity as a function of the Raman shift. The Raman shift is the energy change expressed in wave numbers (inverse of wavelength) and relates directly to the vibrational frequency of the material.

In the Raman spectrum, the Raman shift is plotted on the horizontal axis and relates the frequency shift between the incident laser light and the scattered light as [76]:

$$\Delta\nu(\mathrm{cm}^{-1}) = \nu_L - \nu_R = \frac{10^7}{\lambda_L(\mathrm{nm})} - \frac{10^7}{\lambda_R(\mathrm{nm})} \qquad (2.9)$$

where v_R and v_L stand for the absolute wave number of the scattered light and that of the laser respectively. v_L has a fixed value depending on the laser; v_L = 19450 cm^{-1} for 514 nm line of Ar green laser and 15800 cm^{-1} for the 633 nm line of a HeNe red laser.

In thin film silicon, Raman spectroscopy has been used both for qualitative and quantitative micro-structural analysis. It is one of the easiest methods by which the crystallinity content of amorphous and nanocrystalline materials are determined. Also, qualitatively, it can give an indication of the different phase materials ranging from the amorphous, amorphous-to-nanocrystalline transition and the full crystalline phase materials [76].

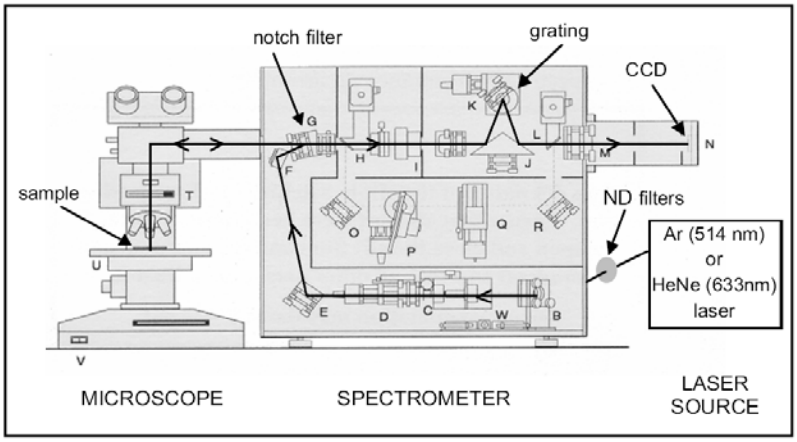

Figure 2.6: Schematics of the basic operation and components of Renishaw [75] Raman microscopy showing the different components that make up the system. The indicated directions show the path of the monochromatic light from the laser until it is incident on the sample in stage and the return path of the scattered light from the sample through the microscope into the spectrometer.

Typically, a nc-Si:H film has a Raman spectrum with a narrow peak at around 520 cm^{-1} as in c-Si. This transverse optical mode peak shows an asymmetric broadening of its width and a tail towards lower wave numbers.

The Raman spectra of the films were measured using a Raman microscope (Renishaw InVia, grating 1800 lines/mm) in a 180^{o} back scattering geometry. It is fitted with a 25-mW Ar laser at a wavelength of 514 nm focused on a spot of about 1 μm. The schematic of the set-up is shown in figure 2.6. The laser produces the monochromatic incident light; the intensity of which is regulated by Neutral Density (ND) filters to allow a certain percentage of the entire beam. This beam is directed and focused on the sample with the aid of the spectrometer mirrors and microscope. The incident laser beam is scattered by the sample and the scattered beam is re-directed back into the spectrometer via the objective lenses of the microscopes.

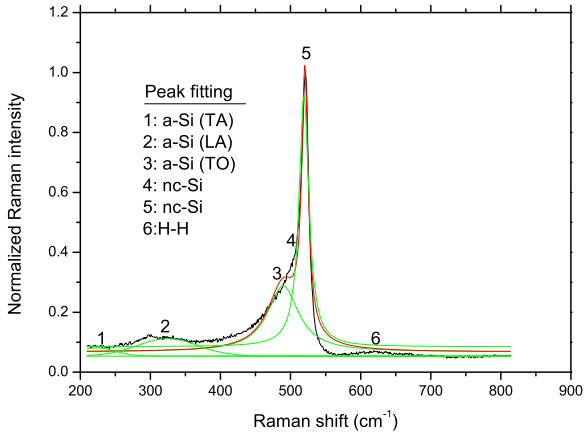

Figure 2.7: Typical Raman spectrum of thin film nanocrystalline silicon showing the fitted peaks for the extraction of the crystalline mass fraction.

By the use of notch filter the Rayleigh or the elastic scattered light is filtered out. The remaining Raman scattered light on getting to the grating is diffracted into a spectrum and collected by the sensitive charge coupled device (CCD) array. The CCD converts this to electrical signals and transmits same to the computer for further processing. The measurements were carried out in confocal mode with a 100 x objective lens. The numerical aperture (NA) and the focused laser beam area of this objective is 0.9 and 1 micrometer respectively.

Obtaining crystalline mass fraction from Raman measurement

The crystalline volume fraction, f is a quantity that specifies how much of nc-Si:H components are in the crystalline phase. This parameter was extracted from the Raman measurement by using a peak-fitting approach to the model of Smit et al [47]. First, the complete amorphous contribution in the nc-Si:H is fitted to three Gaussians in the range from 220 to 480 cm^{-1}. Theses Gaussians cover TA peak at 220 cm^{-1}, LA peak at 330 cm^{-1} and TO peak at 480 cm^{-1} as shown in figure 2.7. This range covered in the fitting of the amorphous contribution is to ensure that only the amorphous contribution is considered without any crystalline contribution [18]. This amorphous contribution is subtracted afterwards from the Raman spectrum. The

crystalline contribution which has only TO peaks at 510 and 520 cm^{-1} is fitted with two Lorentzian distributions. The hydride mode at around 650 cm^{-1} is also fitted to a Gaussian. After subtracting the fitted amorphous part of the film from the spectrum, the cross-sectional area of the crystalline part is divided by the sum of the integrated areas of the crystalline and amorphous parts expressed as in equation 2.10 to obtain *f*:

$$f(\%) = 100\left[\frac{I_{520} + I_{510}}{I_{520} + I_{510} + I_{480}}\right] \qquad (2.10)$$

Two major peaks in the Raman spectrum of nc-Si:H are related to its transverse optical (TO) mode. One sharp peak at Raman shift of 520 cm^{-1} associated with crystalline phase and another broad peak at 480 cm^{-1} associated with amorphous phase. As commonly used [77] both the amorphous and the crystalline peaks are fitted to Gaussian distributions. In some instances [78, 79] a combination of both Gaussian and Lorentzian distributions are used. In this work, the crystalline peaks (the 520 cm^{-1} peak and the tail at around 510 cm^{-1}) are assigned to Lorentzian distributions and not Gaussians because we obtained relatively lower error in *f*. The error in *f* is calculated from standard statistical method [80] as a combination error since the formula for calculating *f* consists of 3 variables. It compares the values of *f* obtained from the fitted and actual Raman spectra. Using only Gaussian distributions for all the peaks leads to up to 15% error and for a combination of Lorentzian and Gaussian distributions, less than 5% error is obtained. Note that we have not used the same amorphous silicon spectrum for all the samples as is the case in [47] but fits the amorphous spectrum of each sample.

Depth-profile Raman measurement was carried out on nc-Si:H layers and on solar cells in order to obtain the crystallinity development (evolution) profile. For this purpose, we used the reactive ion etching (RIE) system (Alcatel CL GIR 300) in our group to etch through the depths of the nc-Si:H materials and solar cells. The RIE plasma is generated from a gas mixture composed of 70 sccm of CF_4, 10 sccm of SF_6 and 10 sccm of O_2 under vaccum condition using an rf power of 60 W at a pressure of 0.05 mbar. The reactive species in the plasma diffuse to the sample surface and penetrate through as they interact with the sample. Volatile by-products are produced from this reaction and these are pumped out from the chamber. The sample

is masked at one end with an Al bar while leaving open the other end to be etched. The masked area is not etched hence creates a step with respect to the etched area. Since the entire exposed area is etched, the craters formed have fairly uniform lateral profile across the exposed area. The etch rate varied with depth as the material composition changed. The RIE experiment was done at a set substrate temperature of 50 ^{o}C. This value could not be changed for our experiment because of the system limitation. One difficulty with this is the fact that there could be a possibility of an unintentional thermal-induced crystallization of the samples. To address this, we limited the exposure time of the samples to the plasma to few tens of seconds. Test measurements confirmed that our samples showed no induced crystallization during the RIE experiments following this measure.

Depending on pre-determined etch rate the depths were determined using the Dektak step profiler (Veeco Dektak 150 with 12.5 μm stylus) after each etching step. Etched depth varied from 20 nm to 80 nm with a resolution of ~20 nm. At each depth, Raman measurements were performed and the crystalline mass fraction extracted.

Polarized Raman Spectroscopy (PRS)

Polarized Raman spectroscopy (PRS) for investigating crystal orientation is based on the fact that the intensity of Raman scattered light depends on the polarization of the incident laser light relative to the crystal axes of the material being irradiated [81]. At fixed sample position the change in the intensity of the scattered light is guided by the symmetry selection rules of the sample and gives information concerning the orientation of the crystals within the samples [81-83]. Polarization measurement is induced either by manually changing the position of the intercepting plane of the sample simply by rotation or by the use of a Raman system incorporated angular rotator to change the polarization angle of the incident laser as in our case. The rotator is turned through various angles and this rotation also turns the polarization plane of the incident light.

The possibility of determining the dominant crystal orientation in nc-Si:H is based on the analysis of the internal molecular vibrations obtained from polarized Raman measurement. These molecular vibrations are expressed in the Raman intensities which depend on the polarization direction of the incident laser light and on the

crystallographic grain orientations. It is this Raman intensity dependence on polarization of the incident laser light that is used to determine preferred orientations of crystals [84, 85]. For the work reported here the polarized Raman spectra of standard test silicon wafers of known orientations are used as reference and the spectrum of our nc-Si:H films are compared to a profile comprising a superposition of the three known orientations obtained from the test reference wafers. The comparison is based on the fit parameters obtained from the least square fitting routine developed for the purpose. Results from this approach are compared to results obtained from XRD measurements.

2.4 Solar cells characterization

2.4.1 Current-voltage characterization

The electrical performance of a solar cell is determined from the current-voltage (I-V) correlation obtained on illuminating the cell with a solar simulator calibrated at AM1.5 solar spectrum. From the I-V curve, the short-circuit current density J_{sc}, the open-circuit voltage, V_{oc} and the fill factor, FF are obtained as illustrated in Figure 2.8. The solar cell collection efficiency, η which is a measure of the fraction of the solar energy incident on the cell that is converted into electrical energy is determined from the cell external parameters as:

$$\eta = \frac{J_{sc} V_{oc} FF}{P_{in}} \qquad (2.11)$$

where P_{in} is the input power of 1000W/m^2 of AM1.5 spectrum.

The open-circuit voltage is the voltage at which no current flows through the external circuit; that is at $I = 0$. The short-circuit current density on the other hand is the current density at which no voltage is applied ($V = 0$). The fill factor is the ratio of the maximum power that can be obtained from the cell to the product of J_{sc} and V_{oc}. It is a measure of the 'squareness' of the I-V curve and describes the degree to which the voltage at the maximum power point (V_{mpp}) matches V_{oc} and current density at the maximum power point (J_{mpp})

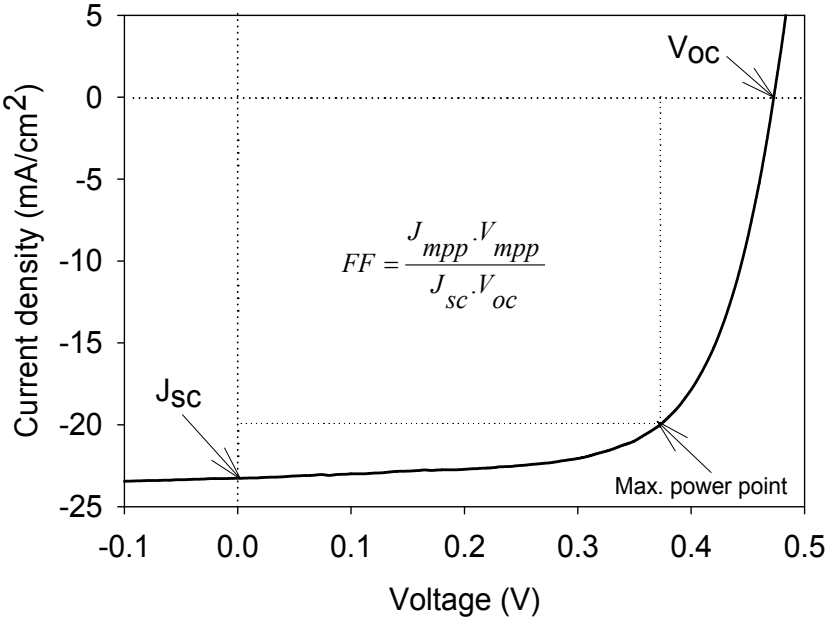

Figure 2.8: I-V Characteristics of a solar cell with the J_{sc} and V_{oc} indicated.

matches J_{sc}. Assuming that a solar cell behaves like an ideal diode, the fill factor relates to the open-circuit voltage by the expression [86]:

$$FF = \frac{\nu_{oc} - \ln(\nu_{oc} + 0.72)}{\nu_{oc}} \qquad (2.12)$$

$$\nu_{oc} = \frac{V_{oc}}{kT/q} \qquad (2.13)$$

Equation (2.13) is the normalized voltage. The dark saturation current density is obtained from the expression:

$$J(V) = -J_{ph} + J_0[\exp(\frac{e(V - JR_s)}{nkT}) - 1] + \frac{V - JR_s}{R_p} \qquad (2.14)$$

J_{ph} is the photogenerated current density, J_0 is the dark saturation current density, R_s is the series resistance, R_p the parallel resistance

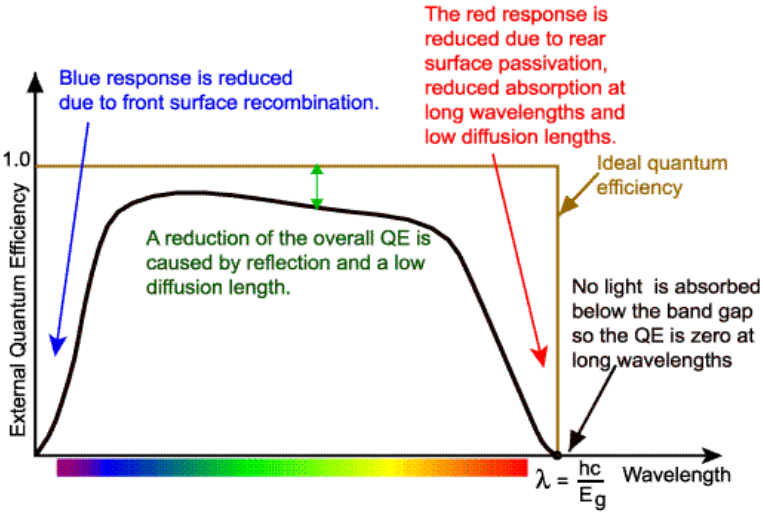

Figure 2.9: Typical external quantum efficiency of silicon solar cell showing the different spectral responses and the mechanisms responsible for losses in spectral responses. Taken from Ref [87].

and n, k, T are respectively the diode ideality factor, Boltzmann constant and the temperature (in Kelvin). R_s and R_p are parasitic resistances in solar cells and they mainly affect the fill factor and hence the efficiency of the solar cell. R_s arises as a result of contact resistance between the silicon layer and the metal contact. R_p on the other hand is associated with defects in the solar cell. These defects create alternate current path for the current generated in the solar cell leading to losses in the generated power.

2.4.2 Quantum efficiency measurement

The quantum efficiency of a solar cell describes how the solar cell responds to monochromatic light and hence is an indicator of how well a solar cell converts light with a specific wavelength to electricity. The quantum efficiency of a solar cell can be described either as external quantum efficiency (EQE) or internal quantum efficiency (IQE). Internal quantum efficiency compares the number of photons on the solar cell to the number of electron-hole pairs generated. IQE is unity if all incident photons generate each an electron-hole pair. On the other hand, EQE relates the photo-generated carriers to the

collection efficiency through the external contacts of the solar cell. A 100% EQE means that all photo-generated electron-hole pairs are collected, i.e they contribute to the current obtained from the device. For photons whose energy is smaller than the band gap the quantum efficiency is zero. A typical EQE plot is shown in figure 2.9.

The EQE measurement set-up used consists of an Oriel Apex illuminator coupled to an Oriel Cornerstone 1/8m monochromator and an Amtek 7225 lock-in amplifier. The solar cell is illuminated using chopped monochromatic light and the photo-generated current measured. Measurements at reverse bias are used to check for recombination losses in solar cell. At reverse bias an extra field is imposed on the device to ensure that all generated carriers are collected. Comparing the EQE at no bias and that at reverse bias shows how much of the carriers are lost to recombination. Except otherwise stated, all the QE measurements presented in this work were done at a voltage bias of 0V.

3 Chapter 3

Sensitivity of thin film nanocrystalline silicon (nc-Si:H) properties to rf PECVD parameters

3.1 Introduction

Hydrogenated nanocrystalline silicon (nc-Si:H) is an interesting solar cell material which was used for the first time in the 90s [17, 88]. One of its main features is its stability against light-induced degradation. Nc-Si:H is applied in the so-called micromorph tandem as bottom cell. In the tandem structure the band gap of nc-Si:H and that of a-Si:H result in an almost-perfect match for effective utilization of the solar spectrum. Initial efficiencies up to 12% have been reported for such double-junction devices [22, 89]. Thin film nanocrystalline silicon is known to evolve into a complex mixed-phase material; the make-up of which depends on the deposition conditions. For rf PECVD films, the general properties of the films are affected by the deposition conditions.

Key challenges in the current effort towards optimizing and utilizing nc-Si:H include the sensitivity of its properties to defects and to the deposition conditions [90]. In conventional rf PECVD, device-quality nc-Si:H is made around the amorphous-to-nanocrystalline transition. This transition regime is usually found within a sensitive process window that is influenced by a number of the deposition parameters [91]. For a variation in any of the deposition and process parameters the transition tends to shift, hence making the process difficult to control. For instance, at a constant rf power and deposition pressure, varying the silane concentration affects the transition with the amorphous fraction increasing with increasing silane flow. For depositions at high gas flows as usually is the case for rf PECVD nc-Si:H, the challenge of flow control and process stability is critical. Deposition parameters such as gas flow ratio, deposition power and deposition pressure have been reported to affect the crystallinity, and

the optical and electrical properties of nc-Si:H [92-95]. However, not much attention has been paid to how these deposition parameters affect the amorphous-to-nanocrystalline transition and the material properties of the film grown around it. Amorphous-to-nanocrystalline transition is important in nc-Si:H growth because devices with highest performance are believed to be made at this transition [36, 96].

In this chapter, we report on the effect of rf PECVD parameters on the material properties of p-type and intrinsic nc-Si:H and on the performance of nc-Si:H solar cells. The i-layer investigation is extended to how the i-layer deposition parameters affect the amorphous-to-nanocrystalline transition. We investigate the effect of transient silane depletion during rf PECVD growth on the performance of nc-Si:H solar cells. A modification in the start-off of the growth process [97] is implemented to reduce this effect. We use the blue response as an indication of the p-i interface quality in solar cell [98, 99].

The outline of this chapter is as follows: In section 3.2, the experimental procedure is discussed. Section 3.3 and 3.4 show results of p- and i-layers development respectively. Section 3.5 presents the results of the sensitivity studies of rf PECVD deposition parameters to the amorphous-to-nanocrystalline transition.

3.2 Experimental details

A series of nc-Si:H p-layers were deposited using rf PECVD to investigate the effect of doping, deposition power, p-layer thickness and front TCO roughness on its material properties and on solar cell performance. The properties investigated include the optical transmittance and electrical conductivity, and the p-i interface property (blue response) of nc-Si:H solar cell. For all the p-layers, the silane (SiH_4) flow was fixed at 1.3 sccm and diborane (B_2H_6, 2% in hydrogen) flow varied between 0.2 and 0.5 sccm, giving a flow ratio in the range 0.1–0.25%. The deposition pressure was maintained at 2.5 mbar while the deposition power was varied from 30 to 80 W.

For the intrinsic layer investigation, the following deposition parameters were investigated: silane concentration, deposition power, deposition pressure, and substrate temperature. These parameters were varied such that a wide range of material compositions were obtained. To investigate how rf PECVD deposition parameters affect the amorphous-to-nanocrystalline transition, we consider nc-Si:H films of

50-55% crystalline mass fraction, *f*, as the transition films [93]. We compare the properties of these films obtained by a systematic variation of different deposition parameters. To obtain materials with *f* within this range, we carefully varied a combination of pressure, power, and silane concentration while keeping all the other deposition conditions constant. The deposition pressure varied between 7 to 11 mbar while the deposition power was maintained in between 60 and 100 W. The silane concentration, S_c, defined as $[SiH_4]/([SiH_4 + [H_2])$ (with $[SiH_4]$ and $[H_2]$ the silane and hydrogen flow, respectively) used to obtain transition material depended on the pressure-power combination and varied between 1.2 and 2.4%. Here the hydrogen was fixed at 150 sccm while the silane flow varied between 1.8 and 3.7 sccm. The crystalline mass fraction was chosen as bases for comparison of the transition materials, because nc-Si:H material properties are very sensitive to this fraction [100].

In conventional rf PECVD, switching on the plasma after simultaneous introduction of SiH_4 and H_2 into the process chamber results in the variation of SiH_4 concentration in the plasma due to its initial depletion and later back diffusion from the reactor chamber; an effect that is associated with inhomogeneous nc-Si:H film growth [97]. The transient depletion experiment therefore involves circumventing the effect of SiH_4 back diffusion by employing a delay between the SiH_4 introduction and plasma ignition and/or by profiling the SiH_4 supply into the process chamber. In this work, a delay time between 10 and 80 s was used with the deposition pressure and the SiH_4 flow fixed at 9 mbar and 2.0 sccm, respectively. In complete nc-Si:H solar cells, the effect of different flow and pressure regime on the solar cell performance were investigated. Typical structure of the nc-Si:H device is as shown in figure 3.1.

To characterize the films, electrical measurements were taken. For this, 300-nm thick Al bars were deposited on the layers and annealed in an oven for 30 min at 130 ^oC in order to secure Ohmic contact. The activation energy of the dark conductivity of the films was obtained from a temperature-dependent measurement of the dark conductivity. The crystalline mass fraction was extracted from the Raman spectroscopy measurements by using peak-fitting approach to the model of Smit et al. [47]. The solar cells were characterized by carrying out current-voltage measurements under AM1.5 Oriel illumination and external quantum-efficiency (EQE) measurements.

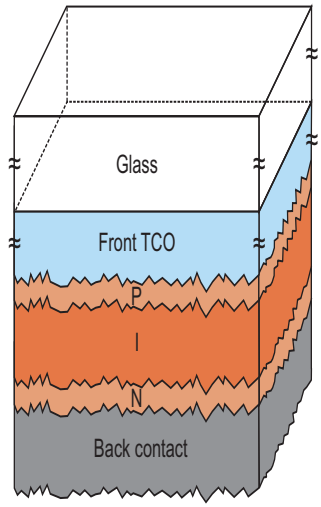

Figure 3.1: Structure of the p-i-n thin film nanocrystalline silicon solar cell as deposited in our rf PECVD set-up. The back contact was a stack of 100 nm thick Ag and a 200 nm Al.

The solar cells had the following structure (see figure 3.1): 25-nm thick p-type nc-Si:H layer, 1100-nm thick intrinsic nc-Si:H layer, 20-nm n-type a-Si:H layer. ZnO:Al-coated Corning glass (E2000) served as the substrate. The ZnO:Al front TCO was sputtered in our lab and thereafter a chemical wet-etching for 40 s in 0.5% HCl was applied in order to roughen the surface for light scattering. Ag/Al layer was used as the back contact. The solar cells were not annealed before the measurements.

3.3 P-layer development

3.3.1 Effect of deposition parameters on p-layer properties.

The p-layer properties of interest includes its transmittance, which is required to be high and its electrical conductivity. The conductivity is expected to be high so that a large built-in potential can be assured [19]. Similarly, high crystallinity is required to promote the nucleation of the nanocrystalline silicon i-layer deposited on it [101].

Figure 3.2 shows the transmittance as a function of wavelength of p-layers of different thicknesses deposited on 40 s etched glass/ZnO substrate. The results indicate that the p-layer thickness affects its transmittance largely at the long wavelength region (> 500 nm), where the transmittance decreases with increase in thickness. In the blue region of the spectrum (< 500 nm) the transmittance varies only slightly with thickness. From the table (inset) in Fig. 3.2 it is clear that crystallinity increases with thickness in line with earlier reports [101, 102]. Decreased long wavelength transmittance can be only partially related to increased absorption in thicker p-layers and is mainly due to amplified reflectance of the air/glass/ZnO:Al/p-layer/air optical system with certain p-layer thicknesses (as indicated by optical simulations- not shown).

In Fig.3.3 the transmittance of p-layer as a function of TCO wet-etching time is presented. The different etching times of TCO in HCl solution result in different TCO roughness as specified in Table 3.1. From the graph we observe that the front TCO roughness does not affect the transmittance of the p-layer significantly. The interference fringes observed for the 0 and 10 s etched TCOs are due to their lower roughness and hence less diffused scattering. Table 3.1 gives the details of the TCO parameters and the crystallinity of the p-layers deposited on them. We see that even with a large change (from 9 to 76 nm) in the root mean square roughness, σ_{rms} of the TCO, the p-layer crystalline mass fraction varies only slightly. Hence a further indication that the p-layer crystallinity plays a more dominant role in its transmittance than the roughness of the underlying substrate.

Fig.3.4 shows the transmittance of p-layer for different doping levels. The transmittance of p-layer clearly decreases with increasing diborane flow. At 500 nm of the wavelength axis the transmittance is reduced by almost 50% on increasing the diborane flow from 0.2 to 0.5 sccm. This drop in transmittance with increase in diborane flow can be attributed to the increase in the amorphous mass fraction as boron is known to suppress crystal nucleation [103]. The inset table in Fig.3.4 presents this variation of p-layer crystalline fraction, activation energy, and dark conductivity with diborane flow. This is in agreement with an earlier report in which an inverse relation between the p-layer doping and conductivity was established [104]. Even though the crystallinity drops with increasing diborane the conductivity increases due to increased carrier concentration.

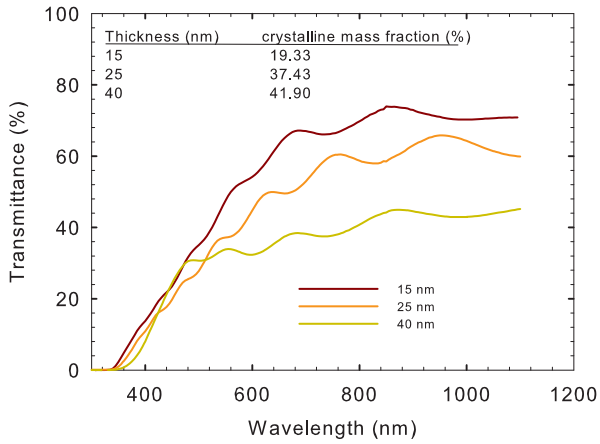

Figure 3.2: Transmittance of p-layers of different thicknesses, deposited on textured glass/TCO substrate.

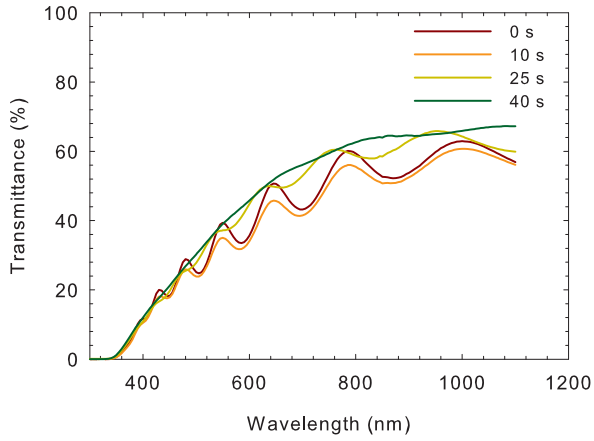

Figure 3.3: Transmittance of 25 nm thick p-layer deposited on different TCO roughness. The legends show the different wet-etching times of the ZnO:Al TCO.

Table 3.1. TCO parameters and the crystalline mass fraction, *f* of 25-nm thick deposited p-layers.

ZnO:Al			p-layer
Thickness (nm)	Etching time (s)	RMS roughness (nm)	f (%)
770	0	9.29	36.82
755	10	14.79	35.61
741	25	68.75	41.39
691	40	76.18	39.94

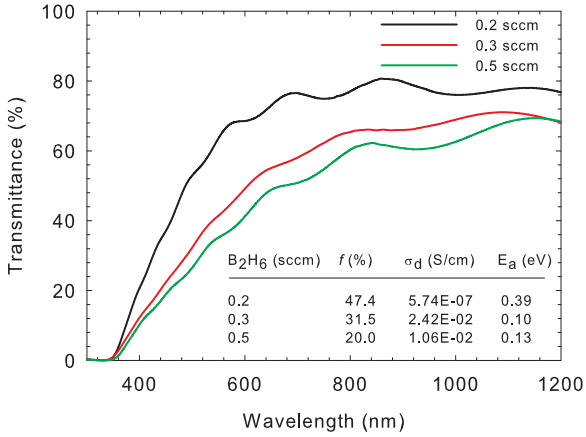

Figure 3.4: Transmittance of 20-25 nm thick p-layers as a function of the diborane flow.

3.3.2 Effect of p-layer deposition power and diborane flow on nc-Si:H solar cell performance.

In Fig. 3.5, external quantum efficiency curves are shown of three nc-Si:H solar cells with 25-nm thick p-layers deposited on 40 s etched glass/ZnO:Al substrate using 0.2, 0.3 and 0.5 sccm of diborane. Increasing the diborane flow reduces the blue response of the solar cells, which we ascribe to the larger amorphous fraction in the p-layer. An increase in diborane flow not only reduces the p-layer crystalline fraction but can also lead to the diffusion of boron atoms into the absorber layer, resulting in unintentional doping of the absorber layer and an attendant defective p-i interface [105, 106]. Reducing the diborane flow from 0.5 to 0.2 sccm results in an increase of the short-circuit current density from 16.3 to 20.0 mA/cm^2. (see inset of Fig. 3.5). The slight drop in open-circuit voltage with decrease in diborane flow can be due to a decrease of the built-in voltage (V_{bi}) as this relates to V_{oc} [107]. The activation energy becomes larger (as can be seen in the inset table in Fig. 3.4) with decrease in diborane flow and results in lower built-in voltage.

The result of the power variation during p-layer deposition on the external quantum efficiency of nc-Si:H solar cell is presented in Fig. 3.6. This series was carried out to optimize the gains of the diborane flow and p-layer thickness further. The results show that the blue response of nc-Si:H solar cells increases with increase in deposition power. Also in this case we link this increase of blue response to the increase in the crystallinity of the p-layer (see also inset table in Fig. 3.6). A highly crystalline p-layer enhances nucleation in i-layer and leads to a more uniform, more transparent and less defective p-i interface [99].

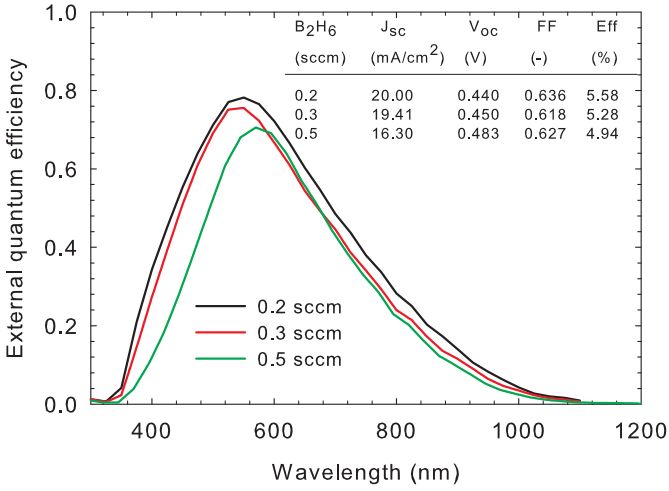

Figure 3.5: External quantum efficiency of nc-Si:H solar cells deposited at varying p-layer doping level.

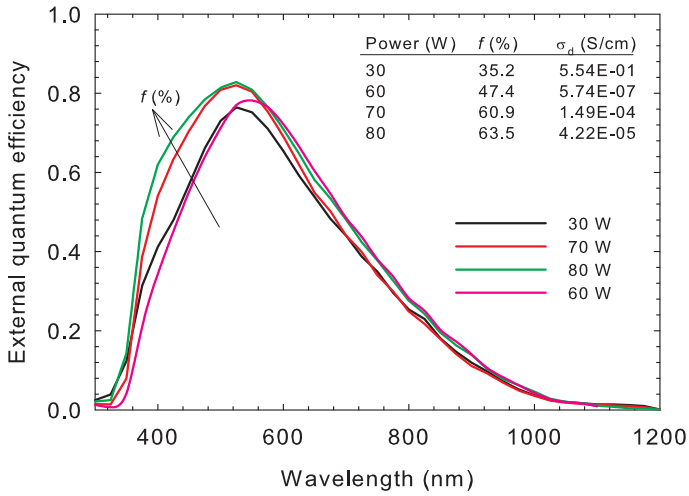

Figure 3.6: External quantum efficiency of nc-Si:H solar cells deposited for various p-layer deposition powers.

3.4 I-layer development

3.4.1 Effect of deposition parameters on i-layer material properties

Our analysis of the effects of i-layer deposition parameters are based on the following material properties: growth rate, crystalline mass fraction, dark conductivity, and activation energy. The deposition parameters were varied such that films spanning from amorphous materials through the transition materials to the full nanocrystalline phase materials are obtained. However, the ranges covered in the deposition pressure were limited by the system configuration. The experiments were done with the following as reference deposition parameters: pressure (9 mbar), power (80 W), substrate temperature (180 ^{o}C), silane concentration (1.32%) and electrode distance (8 mm).

In figure 3.7 the effect of substrate temperature on the material properties of nc-Si:H is presented. Here, the crystalline mass fraction only slightly decreases with increase in temperature in the range 100 to 300 ^{o}C. Low effect of substrate temperature on the crystallinity of nc-Si:H has also been previously observed [108]. Surprisingly, at low deposition temperatures (100 and 150 ^{o}C) low dark conductivity and high activation energy values are obtained, typical of a-Si:H. This low conductivity values at high crystalline mass fraction is however strange and not fully understood, hence will need further investigation. The profile of both the activation energy and the dark conductivity suggest a shift in growth transition from one regime to another in the temperature range of 150 to 180 ^{o}C. Within this shift, the crystalline mass fraction changes from around 48% at 150 ^{o}C to around 62% at 180 ^{o}C. We speculate that this electrical effect can be due to a restructuring of the grain arrangement in the film at high temperature. Such re-structuring probably re-aligns the crystals such that their surface area of contact is increased hence increasing charge carrier transport path within the material.

In figure 3.8, the activation energy, dark conductivity, crystalline mass fraction, and growth rate are plotted as a function of the deposition power. Increasing the deposition power leads to increase in both the growth rate and crystalline mass fraction. As the power increases, the SiH_4 dissociation rate increases, leading to increased growth rate. This SiH_4 dissociation also releases atomic hydrogen, which is essential for crystal formation [109, 54], and hence

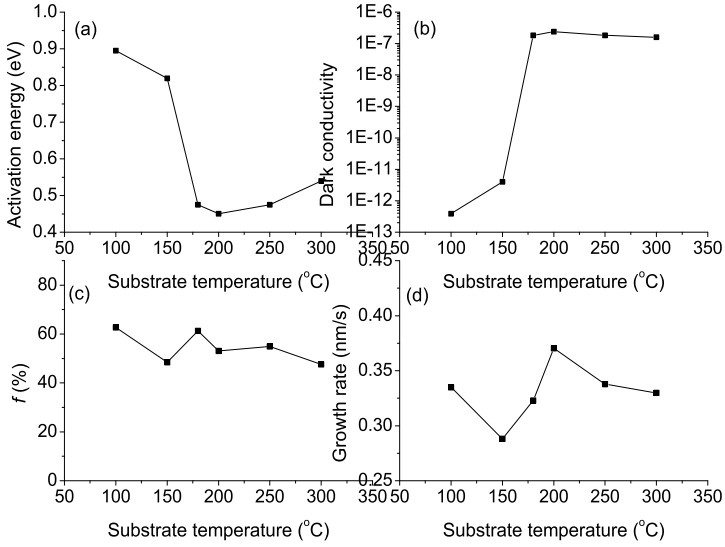

Figure 3.7: Effect of substrate temperature on the (a) activation energy (b) dark conductivity (c) crystalline mass fraction and (d) growth rate of intrinsic thin film nc-Si:H.

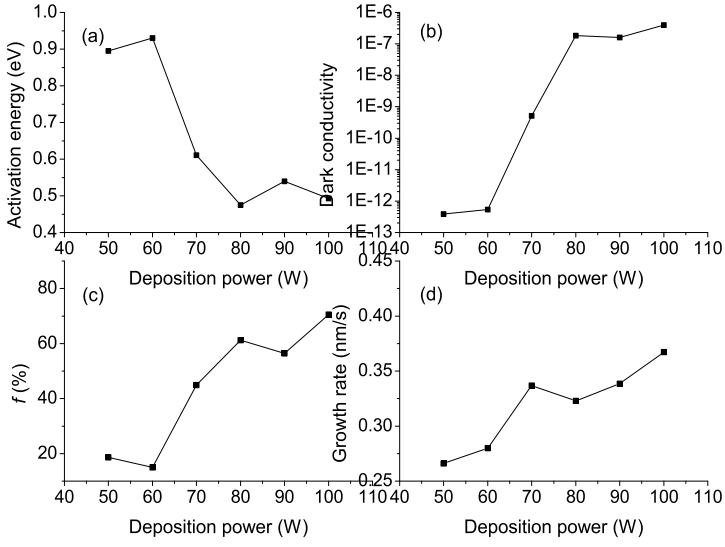

Figure 3.8: Effect of deposition power on the (a) activation energy (b) dark conductivity (c) crystalline mass fraction and (d) growth rate of intrinsic thin film nc-Si:H.

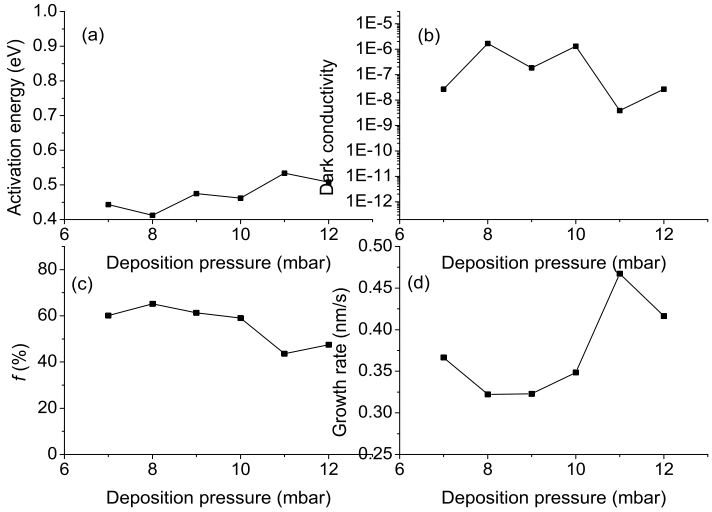

Figure 3.9: Effect of deposition pressure on the (a) activation energy (b) dark conductivity (c) crystalline mass fraction and (d) growth rate of intrinsic thin film nc-Si:H.

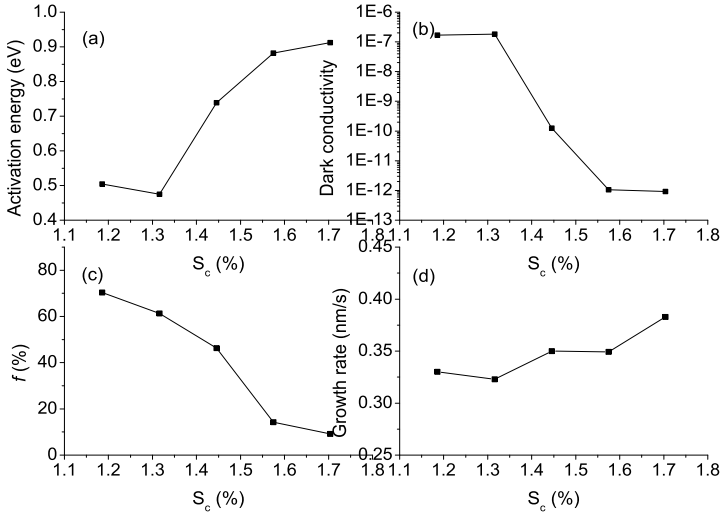

Figure 3.10: Effect of silane concentration on the (a) activation energy (b) dark conductivity (c) crystalline mass fraction and (d) growth rate of intrinsic thin film nc-Si:H.

increases *f*. The growth precursors of nc-Si:H films are generally believed to be SiH_3 radicals, which are formed by the hydrogen abstraction reaction between SiH_4 and H in the plasma [109]. With increase in deposition power the activation energy drops as the material becomes more crystalline. Notice that by varying the deposition power between 50 to 100 W a phase transition takes place from the low (about 19%) to high (above 70%) *f*.

The effect of the deposition pressure on the material properties of nc-Si:H is presented in figure 3.9. The growth rate decreases from about 0.37 nm/s at a pressure of 7 mbar to 0.32 nm/s at 9 mbar before increasing again to peak at 11 mbar. The crystalline mass fraction decreases gradually from around 60% at 7 mbar to 44% at 11 mbar. The activation energy changes by 18% in moving from 7 to 11 mbar. With deposition pressure increasing, the atomic hydrogen concentration in the reactor decreases [42, 110] thus the ratio of atomic hydrogen flux to the SiH_3 radical flux also decreases. As a result, *f* decreases with increase in deposition pressure. It is noteworthy to observe that through the changes in deposition pressure from 7 to 11 mbar, nc-Si:H materials mainly remained crystalline in composition. The values of activation energy and the dark conductivity further corroborate this. Therefore, the deposition pressure affects nc-Si:H composition and growth regime less significantly in comparison to deposition power.

Figure 3.10 shows the effect of S_c on nc-Si:H material properties. Increasing S_c implies increasing the amount of silane relative to that of hydrogen in the flow ratio. This reduces the ratio of H atoms to the SiH_3 radical and in turn favors amorphization, hence *f* drops as shown. The values of *f* indicate that within the S_c values covered, various phase materials ranging from amorphous to highly crystalline phase materials are obtained. The growth rate increases from 0.33 nm/s for the highly crystalline film (*f* around 70%) to about 0.38 nm/s for the amorphous (*f* around 10%). The increase in activation energy from 0.5 eV (for device grade nc-Si:H) to above 0.9 eV (for a-Si:H) with increase in S_c are in agreement with the changing film composition from the highly crystalline to amorphous material.

3.4.2 Sensitivity of amorphous-to-nanocrystalline transition to i-layer deposition parameters

Understanding how the different deposition parameters affect the amorphous-to-nanocrystalline transition will help during deposition in tracking the process window. For this purpose, we investigate transition films grown from different deposition power, pressure and S_c combinations.

From table 3.2, we observe that crystallinity of the transition films are all within the desired values of between 50-55%. However, the input silane concentration varies significantly depending on the power-pressure combination. Increase in deposition pressure favors amorphous growth while increase in power favors the crystalline formation [60]; the basis for the so-called high power high pressure depletion regime. Film growth at high pressure will require high power in order to sustain the growth within or beyond the a-Si:H/nc-Si:H transition.

At a fixed power, lowering the silane concentration will require increasing the deposition pressure and vice versa in order to maintain nc-Si:H growth of layers with $50\% < f < 55\%$. One significance of this therefore is that nc-Si:H growth at low pressure-low power combination can be exploited so as to avoid the powder formation that is known to characterize high power-high pressure nc-Si:H growth [57]. One downside of the low pressure-low power deposition regime is the low growth rate.

Material properties of the transition films presented in table 3.2 indicate that they share similar values of f. However, the other material properties show substantial variation depending on the combined effect of the deposition parameters. For example, at 60 W, increasing deposition pressure from 7 to 11 mbar results in a 19% increase in activation energy and a corresponding 83% and 17% decrease in the dark conductivity and growth rate respectively. Similarly, at 100 W, the activation energy shows a 13% variation while the dark conductivity and the growth rate vary by 95 and 26% respectively. Overall for all the transition films in table 3.2, the activation energy varies by 19% while the dark conductivity and the growth rate change by 95 and 46% respectively. This suggests that even though the transition films have similar material composition, their conductivities vary and is strongly affected by the deposition parameters.

Due to the significant change in the amount of silane concentration required to sustain the growth of transition nc-Si:H, we plot in figure 3.11 the effect of S_c variation on the growth rate and on the electrical properties of the transition films. In this figure, we observe expectedly an increase in growth rate as S_c increases. Such increase in S_c provides for more SiH_3 radicals from the dissociation of SiH_4 hence increasing growth rate [100]. The dark conductivity and the activation energy show significant variation as a function of S_c. As in figure 3.11b, the dark conductivity increases as S_c increases until at a S_c value of around 1.7%. On further increase in S_c beyond this flow ratio, the dark conductivity decreases. A reverse trend is observed for the activation energy. The reason for this trend in the electrical properties of the transition films is not clear yet. However, we speculate that the different deposition settings under which the transition films are made affect their transport properties differently though they have similar *f* values.

Table 3.2: Material properties of transition nc-Si:H films deposited under various power, pressure and gas flow combination. D_p, E_a, σ_d and G_r are the deposition pressure, activation energy, dark conductivity and growth rate, respectively.

Power (W)	D_p (mbar)	S_c (%)	*f* (%)	E_a (eV)	σ_d (S/cm)	G_r (nm/s)
60	7	1.690	51	0.520	5.36×10^{-8}	0.459
	9	1.445	51	0.610	1.38×10^{-8}	0.456
	11	1.269	51	0.642	9.15×10^{-9}	0.382
80	7	2.029	52	0.578	1.28×10^{-8}	0.506
	9	1.575	55	0.621	4.84×10^{-9}	0.394
	11	1.547	53	0.602	2.08×10^{-8}	0.482
100	7	2.340	52	0.596	2.55×10^{-9}	0.702
	9	1.830	53	0.521	4.97×10^{-8}	0.553
	11	1.640	55	0.542	4.16×10^{-8}	0.519

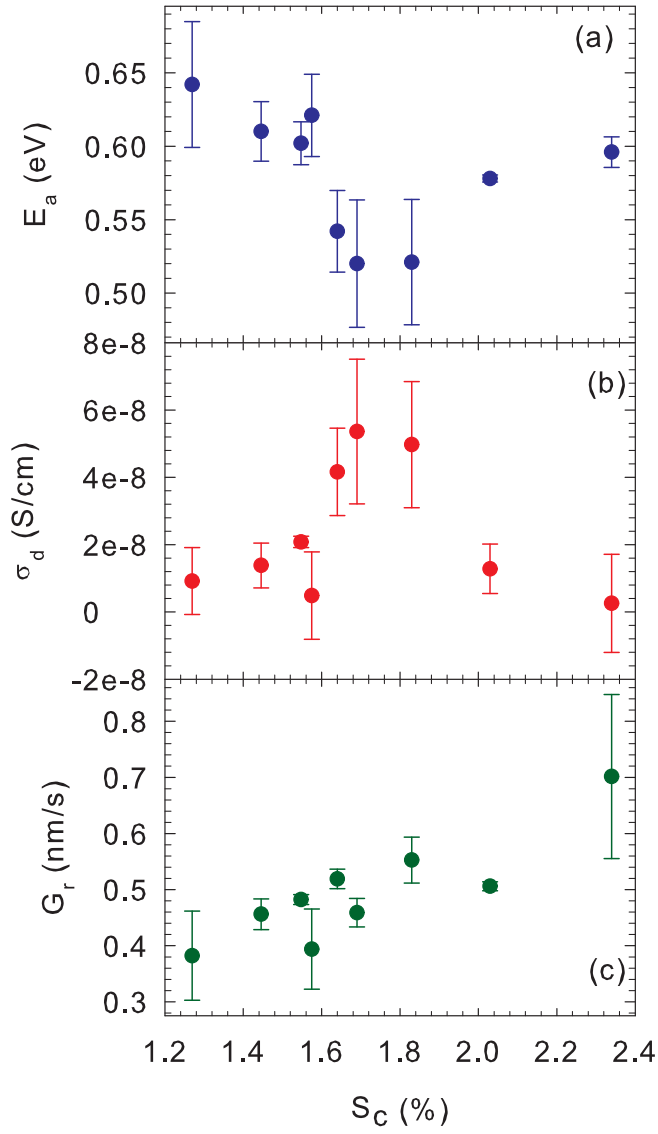

Figure 3.11: The effect of changes in S_c on the (a) activation energy (b) dark conductivity and (c) growth rate of nc-Si:H films deposited at the amorphous-to-nanocrystalline transition using different deposition settings.

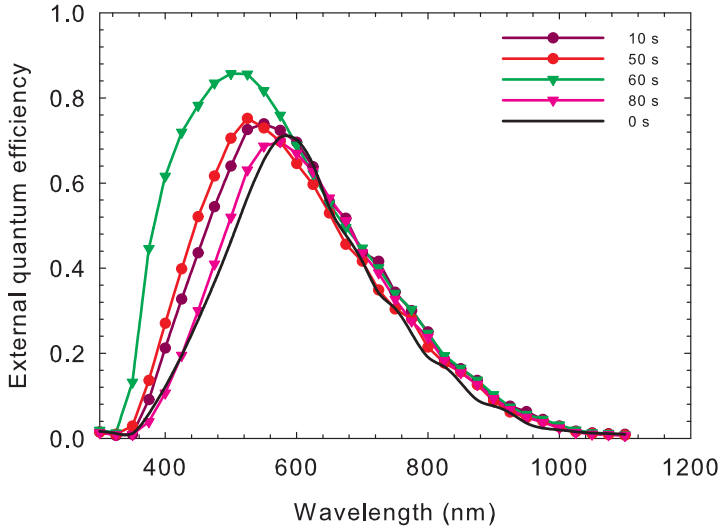

Figure 3.12: External quantum efficiency of nc-Si:H solar cells for different delay time between the time of silane introduction into the plasma zone and the ignition of the plasma.

3.4.3 Effect of transient depletion of SiH_4 on the growth of nc-Si:H

Earlier investigation by van den Donker et al [111] shows that the initial transient depletion of silane in the plasma zone and a subsequent back diffusion results in film growth that is non-uniform and largely amorphous from onset. As a result we use the blue response of nc-Si:H as an indicator of p-i interface quality affected by the amorphous incubation layer induced by transient depletion of silane [99, 111]. First, we fill the process chamber with hydrogen gas. After its stabilization, we bring in the silane gas and after some time delay to allow for the back diffusion of silane from the reactor volume into the process zone, the plasma is ignited. We monitored different delay time and how they affect solar cell performance.

Table 3.3: Nc-Si:H solar cells deposited at different delay time between the time of introduction of SiH_4 into the deposition system and the ignition of the plasma. Note that the solar cells are not optimized in terms of all the deposition parameters hence the low performance.

Delay time (s)	FF	V_{oc} (V)	J_{sc} (mA/cm^2)	η (%)
0	0.601	0.461	15.6	4.33
10	0.619	0.448	17.3	4.79
50	0.591	0.438	17.7	4.58
60	0.570	0.429	20.9	5.10
80	0.628	0.446	16.0	4.49

In Fig. 3.12, external quantum efficiency plots of transient depletion experiments are shown for varying delay times before plasma ignition after SiH_4 introduction into the process chamber. The plots indicate a significant increase in blue response of the solar cell for certain delay time. The blue response increases as the delay time is increased until after 60 s. At 60 s delay, the external quantum efficiency at 400 nm was 60%. On further delay after 60 s the blue response dropped. A possible explanation is that at 60 s delay, the plasma is ignited almost at the same time the SiH_4 is diffusing back into the plasma zone. This leads to a more homogenous nucleation process from onset of growth and reduced amorphous incubation layer [111]. The effect of this is a significant increase in the blue spectral response as shown. At delays longer than 60 s, there is a mismatch in the timing of the silane back diffusion and the ignition of the plasma. As such the SiH_4 concentration gradient is again established between the plasma zone and the reactor volume as in the case of no delay time.

The gains of the transient depletion experiment directly shows in the gain in J_{sc} of the solar cell (see table 3.3) and can be attributed to the relative suppression of the amorphous incubation layer and a more uniform depletion of SiH_4 in the plasma zone [41]. In this way homogeneous material growth is obtained, which aids charge carrier transport through the p-i interface [37]. The initial depletion of SiH_4, which affects the onset growth of the film, mainly influences the p-i interface as there is no observable change in the long wavelength region for all delay times employed.

3.4.4 Effect of i-layer deposition parameters on nc-Si:H solar cell

Based on the results of the above investigation of rf PECVD parameters, three series of nc-Si:H solar cells were deposited. The series include one S_c series for each of 8, 9 and 10 mbar pressure. We limited S_c to values that will yield nc-Si:H ($f \geq 50\%$). For the substrate temperature and deposition power, 180 ^{o}C and 80 W respectively, were used for i-layer deposition following from the sensitivity study results. These values are judged to have resulted in material with crystalline mass fraction intermediate between amorphous and nanocrystalline silicon.

Figure 3.13 shows the external parameters of nc-Si:H solar cells deposited under varying pressure-S_c conditions. We observe that the V_{oc} varies with S_c depending on the pressure regime. At 8 mbar the V_{oc} drops as S_c increases while at 9 mbar the trend is almost reversed. The V_{oc} for the 10 mbar series indicates no significant dependence on S_c. A similar trend is also observed for the FF (see fig.3.13 (b)). The J_{sc} follows an inverse trend to the V_{oc} for 8 and 9 mbar. At 10 mbar the J_{sc} decreases in going to higher S_c. Increasing S_c at higher pressure (9 and 10 mbar) leads to lowering of J_{sc}. This can be linked to the fact that at high pressure, amorphous growth is favored because of the decrease in the atomic hydrogen flux in the plasma [42]. Overall, the efficiencies of the solar cells (fig. 3.13(d)) also fluctuate for the different growth regimes and seem to be mainly affected by J_{sc} given their similar trend. This fluctuations will require further investigation to rule out or otherwise the effect of run-to-run fluctuations during deposition.

In order to investigate further the effect of both deposition pressure and S_c on the solar cell performance, the EQE of the cells is measured. In figure 3.14, the external quantum efficiency of all nc-Si;H solar cells deposited at 8, 9, and 10 mbar is presented for different values of S_c. Here, we observe a strong dependence of the EQE on pressure-S_c combination. At low S_c (1.25%), increasing pressure from 8 to 9 mbar results in significant increase in the EQE especially around the short wavelength region before dropping significantly again at 10 mbar. At S_c of 1.32%, a similar but less-pronounced effect of pressure is observed on the EQE. At these low S_c flow values the process window for the growth of nc-Si:H narrows hence making process control and stability difficult. The fluctuations

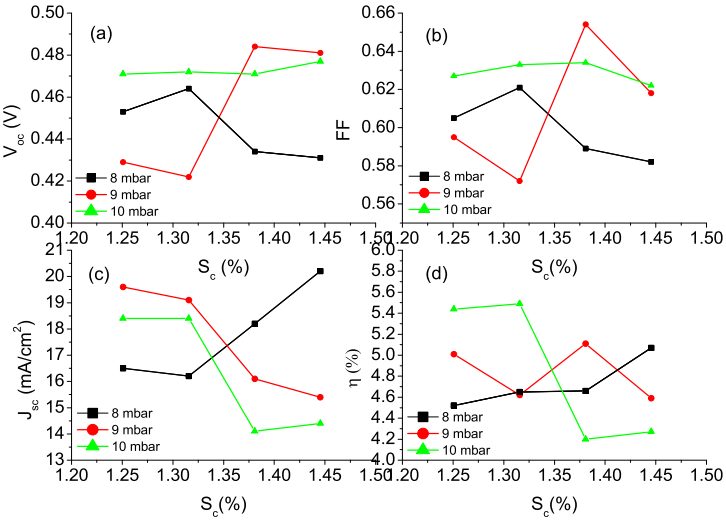

Figure 3.13: Effect of silane concentration on the (a) open circuit voltage (b) fill factor (c) short circuit current density and (d) efficiency of p-i-n thin film nc-Si:H solar cells.

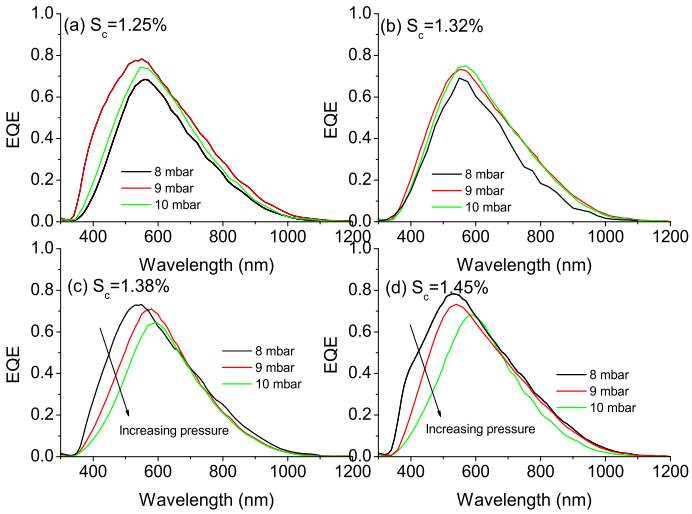

Figure 3.14: Effect of varying deposition pressure at silane concentration values of (a) 1.25% (b) 1.32% (c) 1.38% and (d) 1.45% on the external quantum efficiency (EQE) of p-i-n thin film nc-Si:H solar cells.

in EQE for the different pressure can be related to the fluctuations in the nc-Si:H growth regime at these low flows. At higher silane flow (S_c = 1.38 and 1.45%), the effect of deposition pressure is more pronounced and is mainly observed within the blue spectral response of the solar cells. At these high silane flow regime, the blue spectral response significantly decreases as the deposition pressure increases. Increase in pressure leads to a drop in the blue spectral response because of the associated amorphous growth which dominates onset of growth and leads to an amorphous-rich p-i interface. This defective interface interface results in the low blue response [98].

3.5 Conclusions

The rf PECVD growth of nc-Si:H p- and i-layers have been carried out. The effect of selected deposition parameters of p- and i-layers on the properties of nc-Si:H materials and solar cells were investigated. The p-layer investigation shows that the p-layer transmittance is strongly affected by the doping level and the deposition power. These two parameters are reflected in the crystalline mass fraction of the layer. Increased doping increases the conductivity on one hand and decreases the crystallinity on the other hand. The p-layer properties are thickness-dependent and are not affected by the root mean square roughness of the TCO substrate. Suitable deposition parameters for the growth of p-type nc-Si:H lies in a trade-off between film thickness, transmittance and conductivity.

For the i-layer, the material properties are found to be strongly dependent on deposition conditions. These material properties include the crystalline mass fraction, the growth rate, activation energy and the dark conductivity and have been shown to be affected by such parameters as deposition power, deposition pressure, substrate temperature, and silane concentration. Each of the various deposition parameters affects the material properties at varying degrees. It has been demonstrated that using any of the above deposition parameters as a deposition variable, it is possible to grow device grade nc-Si:H. Device grade films are made within a sensitive process window. For materials deposited at the amorphous-to-nanocrystalline transition by different deposition settings, though they have similar crystalline mass fraction, their electrical properties show a substantial variation. Conventional rf PECVD growth of nc-Si;H by simultaneous introduction of precursor gases and immediate plasma ignition leads to

a transient depletion of the silane content. Time-delay between the gas inlet into the reaction chamber and the ignition of the plasma allows for the back diffusion of silane. We have demonstrated that depending on the delay time the spectral response of nc-Si:H solar cell can be increased. The gain in current outweighs the loss in V_{oc} resulting generally in increase in the solar cell efficiency.

In solar cells, we found that the effect of the i-layer deposition power and pressure are mainly manifested at the short wavelength spectral response of nc-Si:H solar cell. Increase in pressure favors amorphization and is compensated by an increase in deposition power and/or a decrease in silane concentration.

4 Chapter 4

Crystallinity development profile in thin film nc-Si:H

4.1 Introduction

In conventional radio-frequency plasma enhanced chemical vapor deposition (rf PECVD), the growth of hydrogenated thin film nanocrystalline silicon (nc-Si:H) begins with an amorphous silicon incubation layer (ASIL), then continues through the amorphous-to-nanocrystalline transition into the crystalline regime. Crystal growth nucleates on the underlying amorphous tissue and the crystal size and orientation depend on deposition parameters. The effect of this incubation layer on the performance of nc-Si:H solar cells has been widely reported [50, 112, 113]. In a p-i-n solar cell, for instance, absorption losses in the ASIL layer of the p-layer results in a reduced short-wavelength response of the solar cell [98]. Reducing the thickness of the ASIL layer during growth and obtaining high crystalline device quality nc-Si:H material has been a major research challenge till date.

Various approaches have been implemented to control the ASIL layer and thereby increase the crystalline mass fraction, *f*, in the nc-Si:H layer. Van den Donker et al. [97] demonstrated that by means of controlling the transient depletion of silane during rf PECVD the ASIL layer can be reduced. This they did by allowing for a delay between the time of introduction of silane into the process chamber and the starting of the plasma. Agbo et al. [98] implemented this technique in nc-Si:H p-i-n solar cell and observed an increase in the blue response of the solar cell. A major challenge of this technique is the very narrow process window required for this process. Another approach often employed is to grow a very thick nc-Si:H layer such that the incubation layer effect at the p-i interface is reduced [114]. For example, up to 50 nm thick nc-Si:H p-layer and 2000 nm absorber layer are deposited. Such a thick p-layer will reduced the light

transmitted through it. Again, increased film thickness requires more deposition time and material cost.

In recent years, depositing a seed layer is one of the mostly used options to suppress the ASIL layer and enhance crystallization in the growth direction during the deposition of both doped and intrinsic nanocrystalline silicon layers [51, 114-116]. It involves the deposition of very thin layers of mainly intrinsic nc-Si:H usually under very high hydrogen dilution. The seed layer serves as the nucleation layer upon which the active layers of the solar cells are deposited. By seeding the p-layer deposition, nc-Si:H growth evolves with a more uniform *f* and . better charge carrier extraction is ensured [116].

The relationship between solar-cell performance and the crystallinity development profile in the intrinsic nc-Si:H layer in growth direction has not been demonstrated so far. This profile will give an indication of the phase changes that occur as nc-Si:H is formed since the structure of nc-Si:H generally evolves as a function of thickness due to the kinetics of crystalline nucleation and grain growth [117].

In this chapter, we report results of the effect of seeding on the *f* development profile of nc-Si:H and on the performance of p-i-n and n-i-p nc-Si:H solar cells. For this we investigate the crystalline mass fraction in growth direction and show that by seeding, the *f* profile in the active layers of the two solar-cell configurations is modified. Using a Raman setup and Dektak step profiler, we present a crystallinity depth profile of the solar cells. From TEM image analyses and XRD measurements, we probe the structural properties of the bulk of the solar cells. The effect of seeding on crystal size and orientation and micro-strain in nc-Si:H are investigated.

4.2 Experimental details

For this study, we used the rf PECVD set-up in our laboratory. First, the seed layers, which in our case are highly crystalline intrinsic nc-Si:H layers, were optimized. The optimization focused on the thickness and *f* and their effect on material properties of nc-Si:H p- and i- layers. Details of the optimization results are reported elsewhere [102]. The optimized seed layers were implemented in p-i-n and n-i-p nc-Si:H solar cells. In the p-i-n series, first a reference solar cell (herein after called sample A) was deposited without applying any seeding. Next, a p-i-n solar cell (sample B) of similar structure was

deposited except that a 40-nm thick intrinsic seed layer was deposited after the p-layer. In another solar cell (sample C), a seed layer was introduced before the growth of both the p- and i-layers. Sample A had the following structure: Corning (E2000) glass/800 nm ZnO:Al/20 nm nc-Si:H p/~1100 nm nc-Si:H i/20 nm a-Si:H n-layer/100 nm Ag/200 nm Al. For the n-i-p solar cells, a reference unseeded (sample D) and a seeded (sample E) were deposited using the same deposition conditions as the p-i-n cells except for the sequence of deposition. For sample E the 40-nm thick intrinsic seed layer was deposited on top of the a-Si:H n-layer to precede the growth of the i-layer. The n-i-p cells had 250-nm thick flat ZnO:Al layer as back contact with a 300-nm thick Ag layer deposited on Corning glass (E2000). The structure of the unseeded p-i-n and n-i-p solar cells are shown in figure 4.1. For all experiments, the thickness of the i-layer in the solar cells was about 1000-1200 nm.

The solar cells are characterized by carrying out external quantum-efficiency measurements and current-voltage measurements under AM1.5 illumination. The crystallinity development profile in the solar cells is determined by a combination of reactive ion etching (RIE) and Raman spectroscopy. The crystallinity development profile here refers to the depth profile of *f* measured in growth direction. For this purpose, we used the RIE system (Alcatel CL GIR 300) in our group to etch through the depths of the solar cells beginning from the top n-layer for p-i-n (and top p-layer for n-i-p) solar cells down to the front (back) TCO layer. RIE is carried out at 50 ^{o}C. Depending on the pre-determined etch rate, the depths are determined using the Dektak step profiler (Veeco Dektak 150 with 12.5 μm stylus). Each RIE process step etched 20 nm to 80 nm of the test material with a resolution of ~20 nm. Raman measurements were performed at various depths in the solar cells after each etching step. Note that the exact penetration depth of the Raman laser varies as the crystalline mass fraction changes with depth.

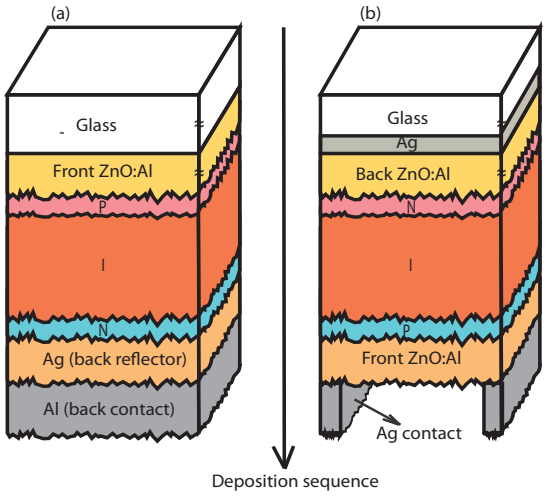

Figure 4.1: The schematic structure (not to scale) of the reference unseeded (a) p-i-n and (b) n-i-p nanocrystalline silicon solar cells.

The Raman spectra are measured using a Raman microscope (Renishaw, Ramascope system 2000, grating 1800 lines/mm) in a back scattering geometry with a 2-mW Ar laser at a wavelength of 514.5 nm focused on a spot of about 1µm in diameter. The penetration depth of the 514.5 nm laser in nc-Si:H is estimated to be around 300 nm [77]. This however is dependent on nc-Si:H composition. The crystalline mass fraction was extracted from the Raman spectroscopy measurement by implementing peak-fitting approach following the procedure of Smit et al. [47].

Transmission electron microscopy (TEM) measurements are carried out on samples A to E using the FEI Tecnai F20ST/STEM transmission electron microscope for imaging. The samples are prepared as earlier described in chapter 2. Fast Fourier Transforms (FFTs) of the HREM images are carried out. Since bright and dark field contrast of the same grain changes a lot in the growth direction because of defects and bending of the TEM foil, only the grain diameter parallel to the substrate interface was determined. Dark field images are not shown since they did not reveal any additional information with respect to the bright-field images. Further structural characterization of the solar cells for crystallite size and their crystallographic orientation and micro-strains are investigated by x-ray diffraction (XRD) analysis.

4.3 Results and discussion

4.3.1 Seeding effects on p-type and intrinsic nc-Si:H

In figure 4.2(a), the Raman spectra of 25 nm thick p-layers deposited on seed layers grown using varying silane concentration, S_c are compared with the reference case with no seed layer. We observe that for the p-layers with no seeding applied (none) and the p-layer with a seed layer that has a large amorphous fraction (S_c = 0.25%), the Raman spectra show a strong contribution of the 480 cm^{-1} peak; an indication of a significant amorphous fraction in the material from the onset of growth. For low values of S_c (0.05% and 0.15%), the Raman spectrum shows a more pronounced crystalline peak at 520 cm^{-1}, indicating that the amorphous fraction in the film is well reduced.

The Raman spectra of the intrinsic layers of different S_c are shown in figure 4.2(b). The thickness of the i-layers ranged from 402 to 483 nm. The thicknesses of the i-layers were limited to this range so as to be able to probe the entire film. Higher values for f are observed in i-layers (though with high S_c) than in p-layers because these i-layers are thicker and the crystalline mass fraction increases with film thickness. Without a seed layer, the Raman spectrum clearly shows a broad peak at 480 cm^{-1}. Upon seeding, f increases and this relates directly to other material properties of the film: the dark conductivity increases and the activation energy decreases [102].

4.3.2 Effects of seed layers on the performance of p-i-n and n-i-p nc-Si:H solar cells

In figure 4.3(a), the external quantum efficiencies (EQE) of p-i-n solar cells A, B and C are presented. The figure shows that implementing seed layers in the growth of nc-Si:H p- and i layers of nc-Si:H p-i-n solar cell leads to a large increase in short-circuit current density of the solar cell. In sample B the increase in J_{sc} is observed to arise mainly from the increase in the blue/green region spectral response. Seeding of i-layer facilitates crystal nucleation hence resulting in a more crystalline and transparent material [116].

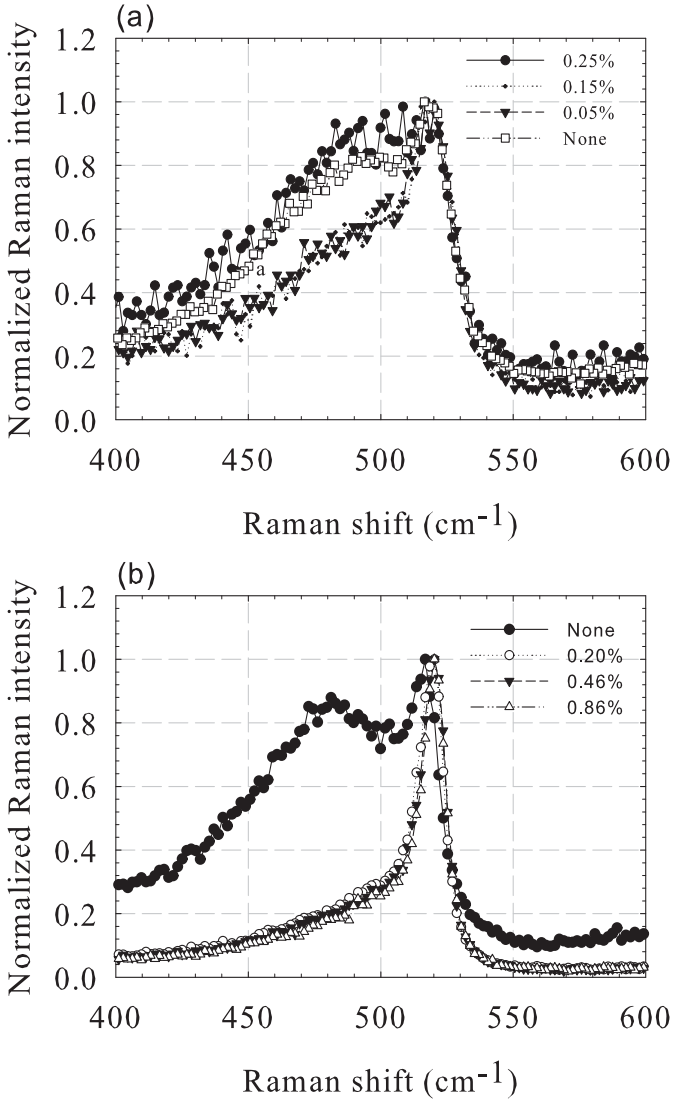

Figure 4.2: Raman spectra of (a) 25 nm thick p-layers and (b) 402-483 nm thick intrinsic nc-Si:H layers deposited on seed layers grown at varying S_c. The measurements were taken from the glass side to show the crystallinity structure of the layers from the onset of growth. The legends indicate the silane concentration of the seed layers.

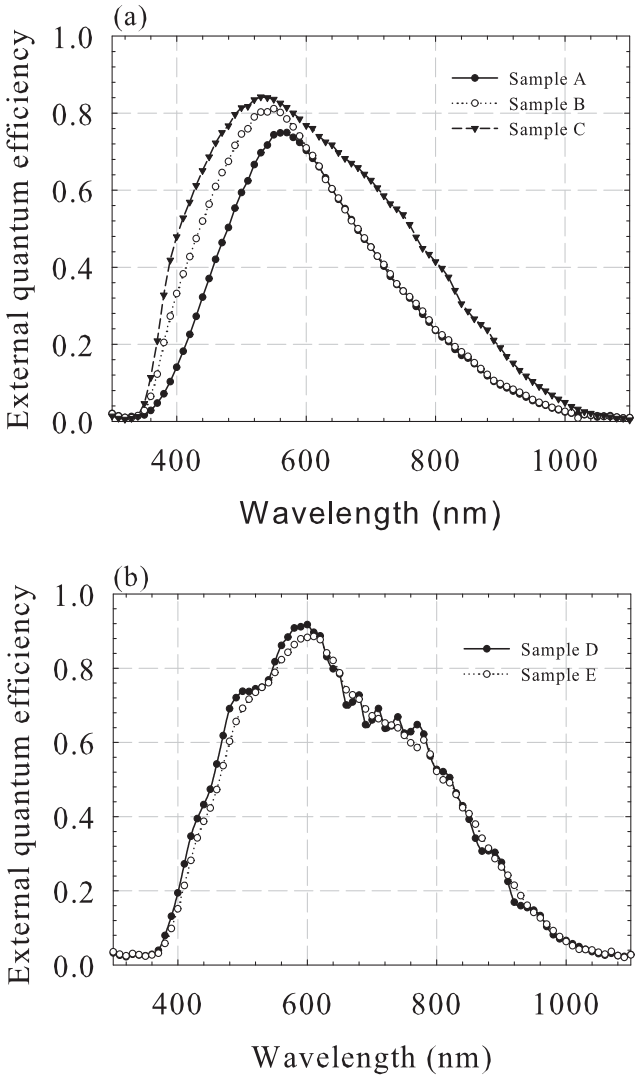

Figure 4.3: External quantum efficiencies of unseeded and seeded (a) p-i-n and (b) n-i-p nc-Si:H solar cells. Note that the solar cells are not fully optimized and the p-i-n cells had no back reflectors.

A more crystalline and transparent nc-Si:H material implies less absorption and hence lower solar cell spectral response within the visible region of the solar spectrum. The EQE, however, increases due to better charge carrier collection from a more favorable electric field distribution in the cell. With seeding of both the p- and i-layers, as in sample C the solar cell's overall performance even increases further due to extended spectral response of the solar cell up to the 1100 nm in the infrared region. From the J_{sc} values obtained from EQE curves as shown in figure 4.4 the J_{sc} increases by 10% for sample B and by 37% for sample C. On the other hand, the V_{oc} and the fill factor drop by 11% and 2.9%, respectively.

Figure 4.3(b) shows a comparison between the external quantum efficiencies of unseeded (sample D) and seeded (sample E) n-i-p solar cells. Unlike the p-i-n cells, the external quantum efficiencies show a slight decrease in the blue on seeding (sample E) and no significant effect in the red region of the spectrum with respect to the reference unseeded cell (sample D). Overall, the J_{sc} decreases by 2%. The V_{oc} increases slightly by 5% and the fill factor drops by 7.9% upon seeding. The seed layer used here affects the i-n interface, which is less critical to charge carrier generation and collection than the p-i interface. Even though the value of f is increased from onset of growth in this region, little contribution is made to the overall performance of the solar cell.

In conclusion, the use of seed layers leads to a gain in J_{sc} and a drop in V_{oc} in p-i-n cells, whereas the opposite is observed in n-i-p cells. The different effects observed in p-i-n and n-i-p solar cells can be linked to the different positions of the seed layers in the solar cells and the different underlying substrates to the seed layer growth. Due to the deposition sequence in n-i-p cells, the seed layer is deposited on top of the a-Si:H n-layer. To grow nc-Si:H on an amorphous silicon under-layer will result in a defective transition layer at or near the interface [116]. This will lead to poor device performance and explains why the n-i-p solar cell performance degrades upon seeding. The drop in the V_{oc} can be linked to the increased porosity of the bulk material with increase in f [118].

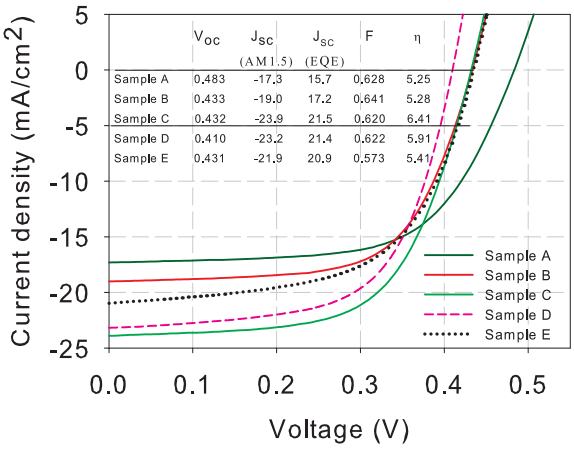

Figure 4.4: The I-V characteristics of the unseeded (sample A: p-i-n and sample D: n-i-p) and seeded (sample B and C: p-i-n and sample E: n-i-p) nc-Si:H solar cells. The external parameters (inset table): V_{oc}, J_{sc}, and η have their units as V, mA/cm^2 and % respectively. The parameter, J_{sc} (EQE) is obtained by multiplying the EQE and the photon flux from AM1.5 spectrum and then integrating over the wavelength range. The value of η is based on J_{sc} (AM1.5) obtained from solar simulator.

4.3.3 Crystallinity development profiles of nc-Si:H solar cells

The comparison presented here is between sample C in which both the p- and i- layers are seeded and sample A with no seeding at all. The crystalline mass fraction as a function of depth in the experimental solar cells is shown in figure 4.5. In figure 4.5 (a), we observe that the crystallinity profile of the seeded p-i-n solar cell (sample C) taken through the cross section of the solar cell is more uniform and follows from rapid nucleation. A gradual build up of the crystallinity in growth direction is observed without seeding as in sample A. In seeded solar cells, crystallinity evolution is more rapid in the region close to the seed layers. In all samples, the crystallinity increases in growth direction and saturates after attaining steady-state condition [117] at a film thickness of about 500 nm. At this thickness the film growth is at the full crystalline phase and hence no further increase in *f* is observed beyond this point. Notice that *f* begins with a value above 40% in

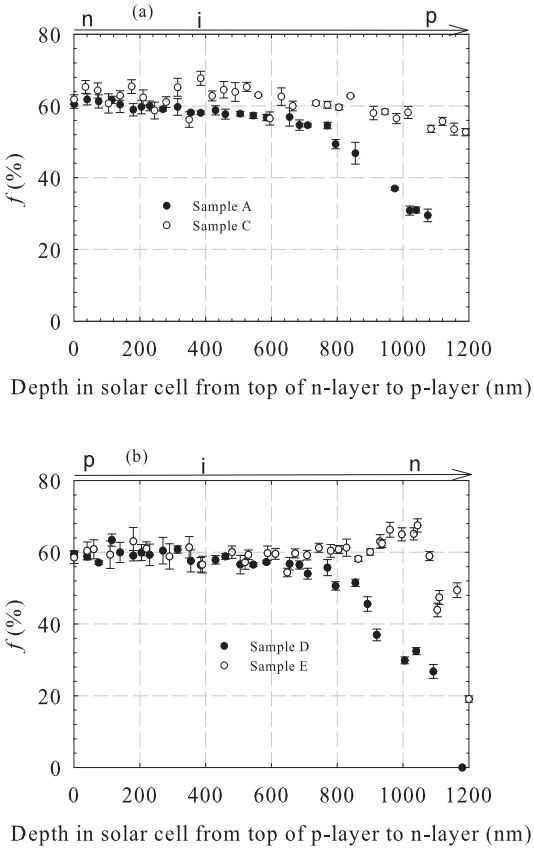

Figure 4.5: Depth profile of the crystalline mass fraction in (a) p-i-n and (b) n-i-p nc-Si:H solar cells. The arrows (not drawn to scale) are guides to the eye and indicate the starting and ending point of RIE experiment. The error bars are the standard deviation values of the crystalline mass fraction obtained for different Raman measurements taken at each given depth.

sample C, which is an indication that the ASIL is completely suppressed. The thickness of ASIL can be estimated by comparing the crystallinity depth profile of sample A and C at onset of growth as in Figure 4.5(a). This is estimated to be around 80 nm.

ASIL can vary in thickness depending on the underlying substrate and the deposition conditions [119]. The use of seed layer for the rf PECVD growth of nc-Si:H facilitates crystal nucleation and eliminates the adverse effect of ASIL. This shows the possibility to

grow nanocrystalline silicon directly from a crystalline growth phase without the growth evolving through the intermediate phases.

Crystallinity depth profiles for n-i-p nc-Si:H solar cells are presented in figure 4.5(b). Just as in the p-i-n cells, the crystallinity is enhanced with seed layers and is also observed to lead to rapid crystallinity build up or nucleation in growth direction and provides constant f of about 60% afterwards. The increase in crystallinity observed for both seeded p-i-n and n-i-p cells does not yield similar results in the performance of the solar cells. The difference can be attributed to the differences in the underlying substrates and the sequence of deposition between p-i-n and n-i-p solar cells.

4.3.4 Microstructure analysis of p-i-n and n-i-p nc-Si:H solar cells

4.3.4.1 Analysis by transmission electron microscopy (TEM)

Figure 4.6 shows the (i) TEM high resolution images (HREM), (ii) bright field (BF) images under focus, and (iii) the bright field images of the unseeded (sample A) and seeded (samples B and C) p-i-n solar cells. The high resolution images (HREM) of the samples are presented with insets showing the FFTs from a 15 nm × 60 nm area close to the ZnO:Al/nc-Si:H interface. The wide rings are caused by the amorphous Si in this area. The ring patterns consisting of individual spots indicate the presence of silicon crystallites within the amorphous phase. The crystal density is higher in samples B and C than in sample A, as estimated from inspection of a number of images as in figure 4.6 (A(i), B(i) and C(i)) and their FFTs.

From the BF images of all samples, isolated and elongated microcrystals parallel to the growth direction and typical for nanocrystalline growth are observed. The elongated crystallites are irregular in shape and have an estimated average diameter of about 30 nm and a length that extends throughout almost the entire thickness of the solar cell. The grain size was estimated from bright field images at large magnification. Columnar and cone-shaped crystals are also observed. In bright-field images with higher magnification and taken slightly under focus we observe elongated vertical features that correspond to voids, and cracks at grain boundaries that sometimes also extend throughout the entire thickness of the device. Narrow cracks (indicated by arrows in Figure 4.6(ii)) appear as white lines in

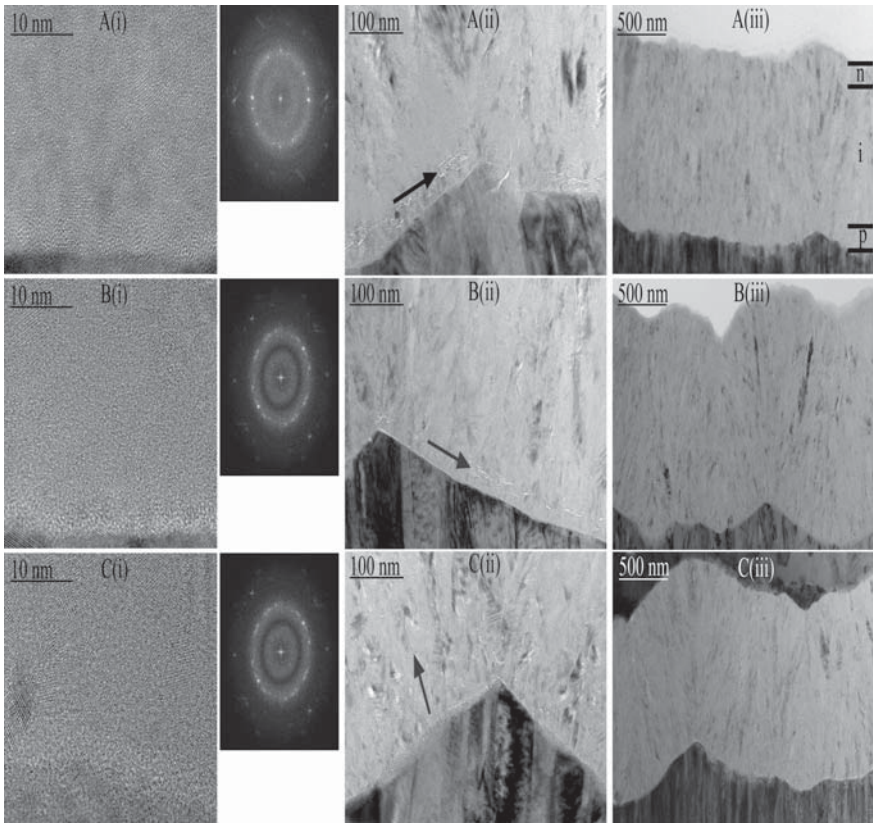

Figure 4.6: TEM images showing (i) TEM high resolution images (HREM), (ii) bright field (BF) images under focus, and (iii) the bright field images of unseeded (sample A) and seeded (samples B and C) p-i-n solar cells. (111), (220) and (113) lattice planes of Si are visible and are reflected as spots in the FFTs. The scale bars are indicated for each image.

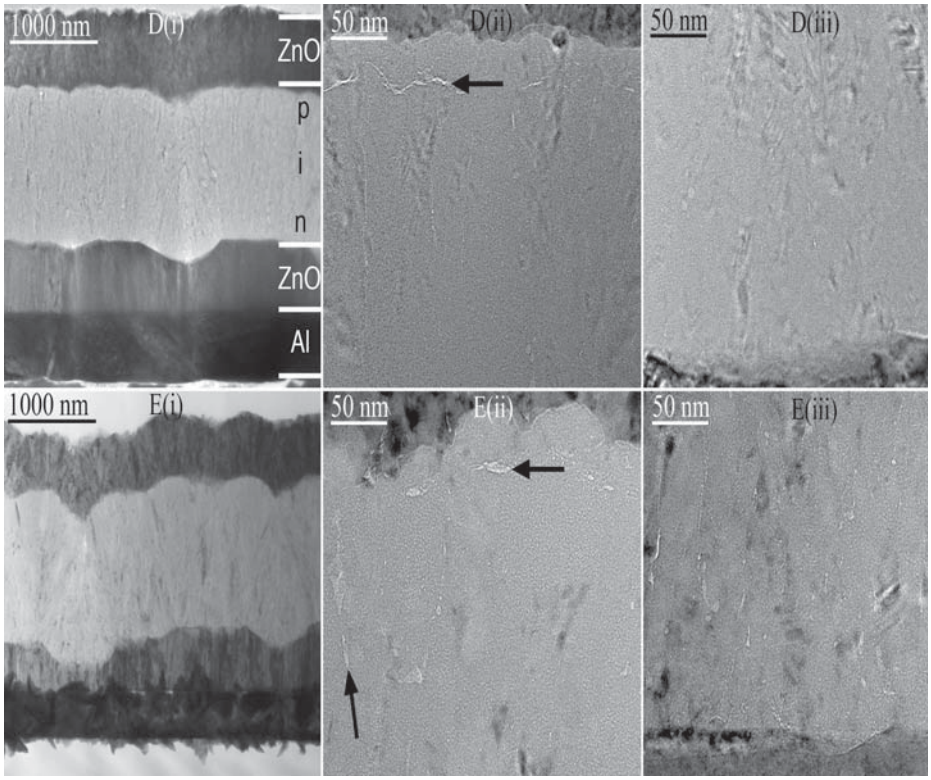

Figure 4.7: TEM images of the entire structure of the n-i-p nc-Si:H solar cells for unseeded Sample D (Di) and seeded sample E (Ei). Columns (ii) and (iii) show the images of the top of the intrinsic layer and directly above the front ZnO:Al layer, respectively for the two solar cells.

bright-field images that are slightly under-focused [92]. We have taken care to ensure that cracks are not introduced during TEM samplepreparation. However, possibility of cracks from sample preparation may not be entirely ruled out here.

From the BF images horizontal cracks are seen everywhere within the first 35 nm of the nc-Si:H layer in sample A. This observation is in line with an earlier report of Roschek [65] where these cracks are found in regions close to the substrate and are linked to internal stress in the film during the onset of growth. Similarly, in sample B, horizontal cracks are also observed but within ~ 15-25 nm from the substrate. No horizontal cracks are observed in sample C within 35 nm from the substrate. We attribute the reduction of cracks by seeding within the substrate-film interface to the reduced substrate inhomogenity effect on the nucleation process. Here the seed layer also serves as a buffer. Without a seed layer, the contact region between the denser ASIL and the less dense overlying nc-Si:H experiences sheer stress and the attendant strain effect is the horizontal cracks.

TEM images of the n-i-p cells are presented in figure 4.7. BF images of the complete solar cells are shown in figure 4.7 D(i) and E(i); BF images of the top and the bottom regions of the absorber layer are shown in D(ii) and E(ii) and D(iii) and E(iii), respectively. Elongated grains are observed within the bulk of the absorber layers, which are thinner than in the case of the p-i-n cells. A crack-rich layer with horizontal cracks was detected 20-30 nm from the front ZnO:Al in unseeded sample D. Also vertical cracks are evident. At the region close to the back contact such a layer was not observed as can be seen in figure 4.7 D(iii) and E(iii). Similar images of seeded sample E also reveal both vertical and horizontal cracks. This trend is opposite to what we observed for the p-i-n cells. Note that in the n-i-p configuration the cracks appear in that part of the layer that is deposited at the end of the i-layer growth, whereas in the p-i-n the cracks appear in the region that is grown first. The difference between sample D and E from the HREM images lies in E having a larger crystallinity than sample D.

With seeding, f increases in both p-i-n and n-i-p solar cells. For p-i-n cells the increase in f is observed without cracks especially at regions close to the p-i interface. On the other hand, for n-i-p cells, cracks are observed near the interface. These cracks inhibit charge carrier transport hence a reduction of the performance of these n-i-p

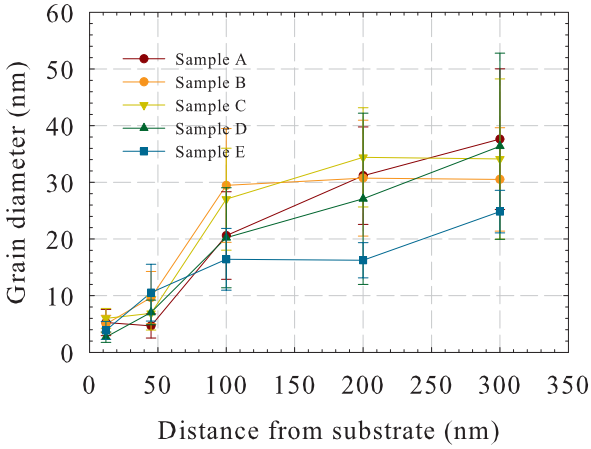

Figure 4.8: Average grain sizes of nc-Si:H crystals calculated from the different positions in the bulk of both the p-i-n and n-i-p cells. The error margins are standard deviations from the average values and lie between 10 and 30% of the plotted values.

solar cells. Similar effects have been reported for solar cells with seed layers grown on an amorphous under-layer [116].

Grain size analyses of both p-i-n and n-i-p solar cells are presented in figure 4.8. The average diameter of the grains was determined from high magnification bright field images, at five different distances from the substrate within the first 300 nm of the silicon layer. Number of grains measured for each position varied from 20 to 65 and the plotted data in figure 4.8 are the average values of the grain diameter determined from the number of grains counted for each position. The error bars represent the spread of the measured values in the diameter distribution. The grain size (diameter) distribution of crystals in all samples show a general increase in growth direction as has also been observed by Hwang et al. [120]. An average grain size of 30 nm is obtained. Seeding does not affect crystal size but affects the crystalline mass fraction in nc-Si:H for p-i-n cells. On the other hand, n-i-p cells show a decrease in the crystal size with seeding and this difference in crystal sizes gets bigger in growth direction. Figure 4.8 also indicates that n-i-p cells have smaller crystal sizes than the p-i-n cells.

4.3.4.2 Seed layer effect on the X-ray diffraction pattern of p-i-n and n-i-p nc-Si:H solar cells

For the XRD analysis, we use a procedure utilizing an integral width of a diffraction line [69, 71]. The x-ray diffraction patterns of the test p-i-n and n-i-p solar cells are presented in figure 4.9(a) and 4.9(b) respectively. The pattern as shown in figure 4.9(a) is typical of highly crystalline nc-Si:H material with the strong visible lines representing the (111), (220) and (311) planes. The solar cells seem to show preferential crystal orientation in the [111] direction irrespective of seeding. The intensity of the (111) silicon crystal plane increases when seeding is used for the i-layer. For the more crystalline sample C having both p- and i-layers seeded the line increases even further; an indication that crystal orientation is affected by seeding. The (220) and the (311) planes vary only slightly with seeding. The broadening of the first broad scattering line at the 2θ position of about 27.5^{o} with seeding can be linked to the ordered region of tetragonal silicon hydride [121]. For the n-i-p cells, a contrary effect is observed. The (111) silicon plane intensity drops slightly with seeding and the scattering line at 27.5^{o} 2θ position shows no variation as presented in figure 4.9(b). In both solar cell configurations, dominant peak intensity is mainly affected on seeding while the identity of the dominant peak (Si (111)) stays the same.

Details of the microstructure analysis of the XRD results are presented in Table 4.1. The crystalline mass fraction of the p-i-n solar cells stays the same even with seeding. On the other hand the f of sample E increases by 16% in comparison with the unseeded sample D. These f values differ from values obtained by Raman and this may be attributed to differences in the probing technique and the probing depth between Raman and XRD. The two techniques probe different depths and regions of the samples. The probing depth of XRD depends on wavelength (energy) of x-ray radiation used, and on the absorption of the material. This depth can extend up to 35 μm in silicon for CuK-alpha x-ray radiation. Raman spectroscopy using a green laser on the other hand has a much lower probing depth, which is limited also to a smaller volume than the XRD. This can explain the differences in f values obtained from the two techniques.

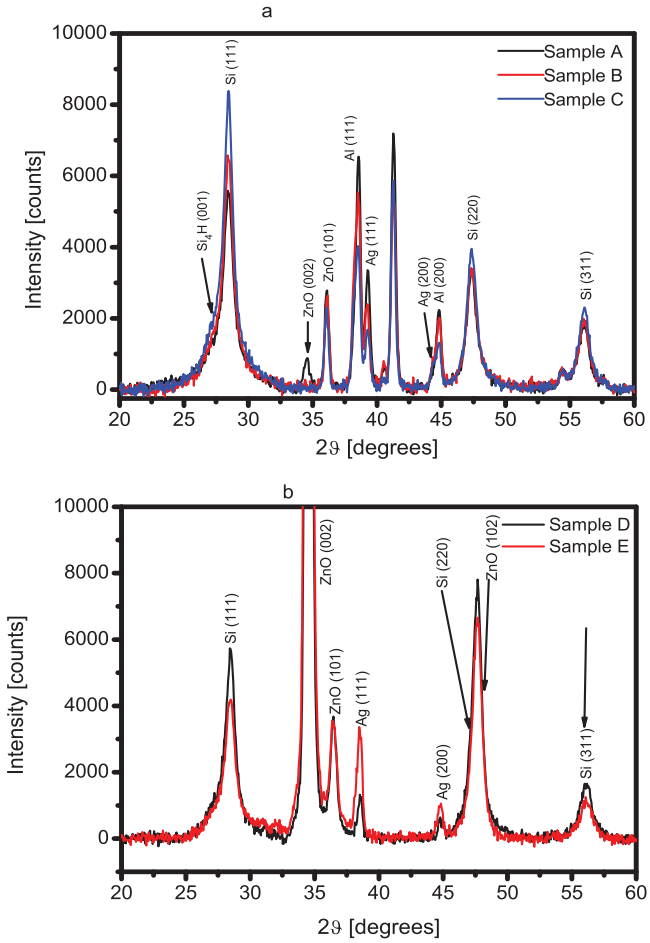

Figure 4.9: XRD patterns of the unseeded and seeded (a) p-i-n and (b) n-i-p nc-Si:H solar cells. The integrated intensity of the line is proportional to the amount of material (atoms, lattice planes) having the same distances from each other where diffraction of x-rays takes place. The Si_4H line is from the tetragonal silicon hydride and the metal lines (Al, Ag) and that of ZnO are from the solar cell contacts. The origin of the peak at around 41 degrees in figure (a) is still not understood.

Table 4.1: Orientation of lattice planes (hkl) and micro-phase parameters in thin film nc-Si:H solar cells. The intensity here refers to the integrated intensity of the line, which is the area below the diffraction line profile. Standard values represent the relative integrated intensity values of the lines for completely randomly oriented crystallites (lattice planes) in space. The standard values were calculated from the theory of diffraction using APX 63 Struc software.

	Relative intensity $I_{(220)}/I_{(111)}$ (%)	Standard values $I_{(220)}/I_{(111)}$ (%)	μc phase volume content (%)	Crystal size, D (nm)	micro-strain, Å X 10^{-3}
Sample A	61	68	45	20	9.3
Sample B	60	68	44	30	10
Sample C	51	68	44	19	7.8
Sample D	50	68	62	13	5.9
Sample E	51	68	72	15	9.0

Average grain sizes of 20, 30 and 19 nm are obtained for samples A, B and C, respectively, and these sizes are in agreement with the grain sizes obtained from TEM. The grain size as well as the micro-strain in the materials show no dependence upon seeding. An increase in grain size results in an increase in the micro-strain for both solar cell configurations. N-i-p cells show much smaller grain sizes in line with the TEM results and a stronger dependence of the micro-strain on seeding is observed as it increases by ~ 52% upon seeding. The general increase in the micro-strain with grain size can be due to the increased structural stress in the films arising from increase in interaction of grains as the grain sizes get bigger [122].

4.4 Conclusions

The use of seed layers to enhance crystal nucleation and crystallinity in nc-Si:H material has been investigated. For conventional rf PECVD growth of nanocrystalline silicon film under high hydrogen dilution,

we show that nucleation starts on the underlying amorphous incubation layer and crystallinity increases gradually in growth direction. With the aid of seed layers this process is modified. In this case, crystallization is rapid and starts almost from onset of growth. In both p-i-n and n-i-p cells we observe that the crystalline mass fraction saturates at the full crystalline regime. The use of seed layers for the rf PECVD growth of thin film nanocrystalline silicon facilitates crystal nucleation and suppresses the amorphous silicon incubation layer. This way it is possible to grow nanocrystalline silicon of uniform crystalline mass fraction directly from a crystalline growth phase without the growth evolving through the intermediate phases.
Seed layers were implemented in p-i-n and n-i-p nc-Si:H solar cells. The use of seed layers leads to an increase in J_{sc} and a decrease in V_{oc} in p-i-n nc-Si:H cells and a decrease in J_{sc} and increase in V_{oc} in n-i-p cells. We obtained 37% increase in the J_{sc} with seeding in p-i-n solar cells relative to the reference case with no seeded layer.

In n-i-p cells, the efficiencies of the solar cells drop on seeding. The external quantum efficiency of n-i-p cells decreases with seeding, whereas a strong increase is observed for the p-i-n cells. TEM measurements have revealed that seed layers can reduce the crack density in p-i-n nc-Si:H. The crystal size increases in growth direction in both p-i-n and n-i-p solar cells and showed no dependence on seeding. However, in p-i-n cells slightly larger grain sizes were found than in n-i-p cells. XRD results indicate that the peak intensity of the dominant crystal orientation is affected by the use of seed layers while its identity (in this case, Si (111)) stays the same. In p-i-n solar cells, dominant [111] orientation is observed in all solar cells and an increase in the contribution to the spectrum of the (111) silicon plane is observed with seeding. For the n-i-p cells the dominance of the (111) silicon plane is also observed, however it shows a slight drop on seeding. Crystallite sizes calculated from XRD results corroborate the results from TEM and shows crystallites sizes in the range of 13-30 nm for all the cells investigated with the n-i-p cells having smaller crystallite sizes than the p-i-n cells.

5 Chapter 5.

Substrate effect on crystallinity development in thin film nc-Si:H

5.1 Introduction

Thin fim nanocrystalline silicon is usually deposited directly on glass substrate especially for material characterization. In either substrate or superstrate configuration, nc-Si:H solar cell active films are deposited on glass with either a transparent conductive oxide or another silicon layer. For infrared spectroscopy measurement films are deposited directly on crystalline silicon wafers. Finding a correlation between the different substrates and the crystallinity development profile of the deposited layer is still an open question. The nature of substrate and its morphology influence the growth of thin film nanocrystalline silicon as has been variously shown [40-42, 50-52]. This influence mainly affects the onset of growth and in turn the material properties of the deposited layer. In terms of the substrate morphology, Python [123] has shown that relatively flat substrate results in dense nc-Si:H film whereas sharp textured substrate results in incorporation of voids and cracks within the film. These voids are empty spaces or volumes that exist in a growing layer which he opines arises as result of limited coverage ability of silicon growth in the trough of the crater on the surface of the substrate.

In this chapter, the work in chapter 4 is extended. Substrate effect on the crystallinity development profile of nc-Si:H is investigated. Phase changes at different depths in nc-Si:H are linked to changes in crystallinity in growth direction. It is shown that the substrates affect the crystallinity development profile. Using nc-Si:H seed layers deposited first on the substrate to facilitate crystal nucleation, the growth profile of the overlying nc-Si:H layer is modified. We shall show that the substrate effect can also be favorably manipulated during film growth. By means of XRD measurement, the effects of the seed layers and the underlying substrate on the preferred orientation of the crystals in the films are also investigated.

5.2 Experimental details

Films reported here are intrinsic nc-Si:H grown using the rf PECVD set-up in our laboratory. In the first deposition series, we deposited in one run ~ 500 nm thick layers on three different substrates: Corning glass (E2000), Corning glass with 15-nm thick p-type nc-Si:H and Corning glass with 40 s etched ZnO:Al. For this deposition, the H_2 and SiH_4 flows were fixed at 150 and 2.2 sccm respectively. The deposition pressure and the substrate temperature were kept constant at 9 mbar and 180°C, respectively while the deposition power was maintained at 78 W. In another deposition run, seed layers were first deposited on the substrates using SiH_4 flow of 0.7 sccm for 5 minutes while keeping all the other parameters constant. Afterwards, nc-Si:H layers were grown using same conditions as in the first case. The films were characterized using X-ray diffraction and Raman spectroscopy following the same procedure described in chapter 2.

5.3 Results and discussion

5.3.1 Crystallinity development profile of nc-Si:H on different substrates

The crystallinity depth profile in growth direction of intrinsic nc-Si:H layers deposited on Corning glass, Corning glass with nc-p-layer and Corning glass with 40 s etched ZnO:Al is presented in figure 5.1 (a). Here the indicated phase materials are distinguished using the specified f ranges for ease of understanding of the structural and phase-change evolution in growth process. The crystalline mass fraction generally increases in growth direction in all the substrates. The changing crystallinity is an indication of a phase transition in growth direction beginning from the amorphous incubation layer through the amorphous-to-nanocrystalline transition. Through this transition structural changes evolve further into the full nanocrystalline regime where crystallinty saturates. From figure 5.1(a) it is seen that the layer grown on a nanocrystalline background gives

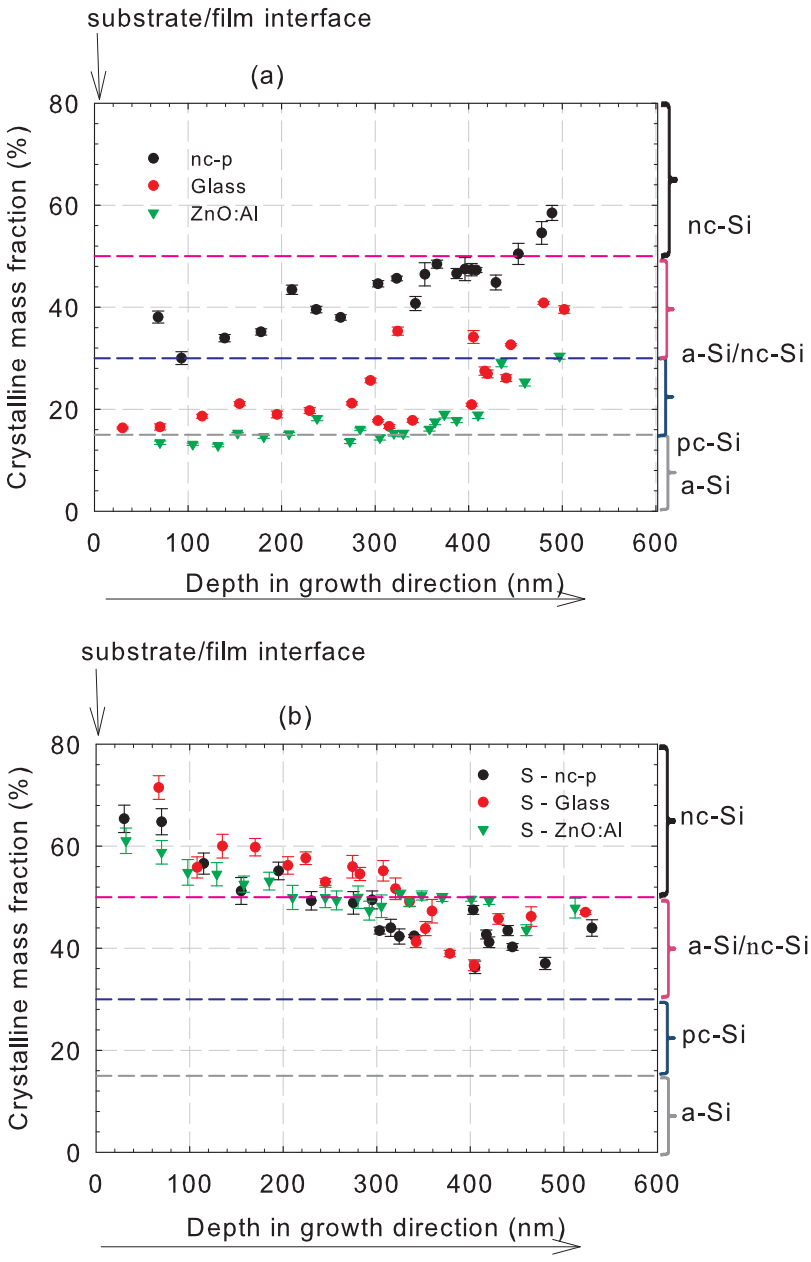

Figure 5.1: Crystallinity depth profile of rf PECVD thin film nanocrystalline silicon deposited directly on glass, glass with nc-Si:H p-layer and glass with etched ZnO:Al (a) without a seed layer and (b) with a seed layer. The legends represent the substrates.

higher crystallinity relative to the other substrates hence implying that there is a substrate-dependent effect in this case. The ZnO substrate shows the least crystalline mass fraction both at onset of growth and at the end of growth.

5.3.2 Seeding effect on crystallinity development profile of nc-Si:H on different substrates

In figure 5.1(b) the crystallinity depth profile of the test layers are shown with the layers deposited on the same substrates as in figure 5.1(a) under the same deposition conditions except that a 40-nm thick nc-Si:H seed layer was first deposited on the substrates before main test layers. Here, a modification in the growth profile is observed in all the substrates. The crystalline mass fraction, f, evolves rapidly (f~ 60%) from the onset of growth, which leads to an initial higher crystalline mass fraction. This trend is a reverse of what is usually obtained in conventional rf PECVD nanocrystalline layers without an underlying seed layer as in figure 5.1(a). This way it is possible to make nc-Si:H films with high crystallinity with the growth evolving directly from the nanocrystalline regime and bypassing all the other intermediate growth phases as shown. This further implies that high crystalline nc-Si:H can be obtained for even much thinner layers [114]. Notice that there is a limited dependence of the crystallinity development on the substrate in this case. This possibility of manipulating the growth process from the substrate can be a vital approach in controlling the growth mechanisms of nc-Si:H, which are quite sensitive to often-erratic plasma and deposition conditions. The similar crystallinity depth profile of all the substrate implies that seeding reduces the substrate effect on the growth mechanisms of nc-Si:H [115]. We speculate that this can be linked to the uniform silicon nuclei distribution on the substrate surface after seeding. For thicker layers, the crystalline mass fraction at the end of growth would be similar independent of seeding as also shown in figure 4.5.

5.3.3 Bi-facial Raman profile of seeded and non-seeded nc-Si:H layers deposited on different substrates

In order to investigate further how the substrates and seed layers affect the crystallinity evolution at the onset and at the end of film growth, a bi-facial Raman measurement was carried out. Bi-facial Raman measurement implies measuring the Raman profile of the films with the laser entering from the glass side in one instance and from the film side on the second instance [77, 124]. Results of this investigation are presented in figures 5.2 and 5.3 for the unseeded and the seeded cases respectively.

In figure 5.2(a) the glass-side Raman profile shows an initial growth that is dominated by the ASIL given the broad peaks around the 480 cm^{-1} typical of amorphous material in all the substrates used. Figure 5.2(b) gives the facial Raman profile with obvious crystalline peak at 520 cm^{-1} especially for the film deposited on nc-Si:H p-layer and on glass. A clear dependence on substrate especially at onset of growth is observed. The Raman profile of nc-Si:H layer deposited on glass/nc-Si:H substrate shows a stronger crystalline peak at around 520 cm^{-1} which can be linked to the already-crystalline growth background.

The bi-facial Raman profiles of the seeded layers are presented in figure 5.3. The back-side profile (figure 5.3(a)) shows that the nc-Si:H films evolved without the ASIL and this further corroborates the results in figure 5.1(b). The seed layer here not only facilitates nucleation by eliminating ASIL but also suppresses effects of underlying substrate hence the similar Raman spectrum obtained for the three substrates. The facial Raman profile represented in figure 5.3(b) indicates pronounced crystalline peaks in all the films with slight differences in their amorphous shoulder.

In downplaying the substrate effect, seed layers provide a background that promotes uniform silicon nuclei distribution on the substrate at onset of growth. This way, they serve as ‘cap’ to the substrates hence suppressing possible interferences to crystallinity development that may arise as a result of the nature of substrate.

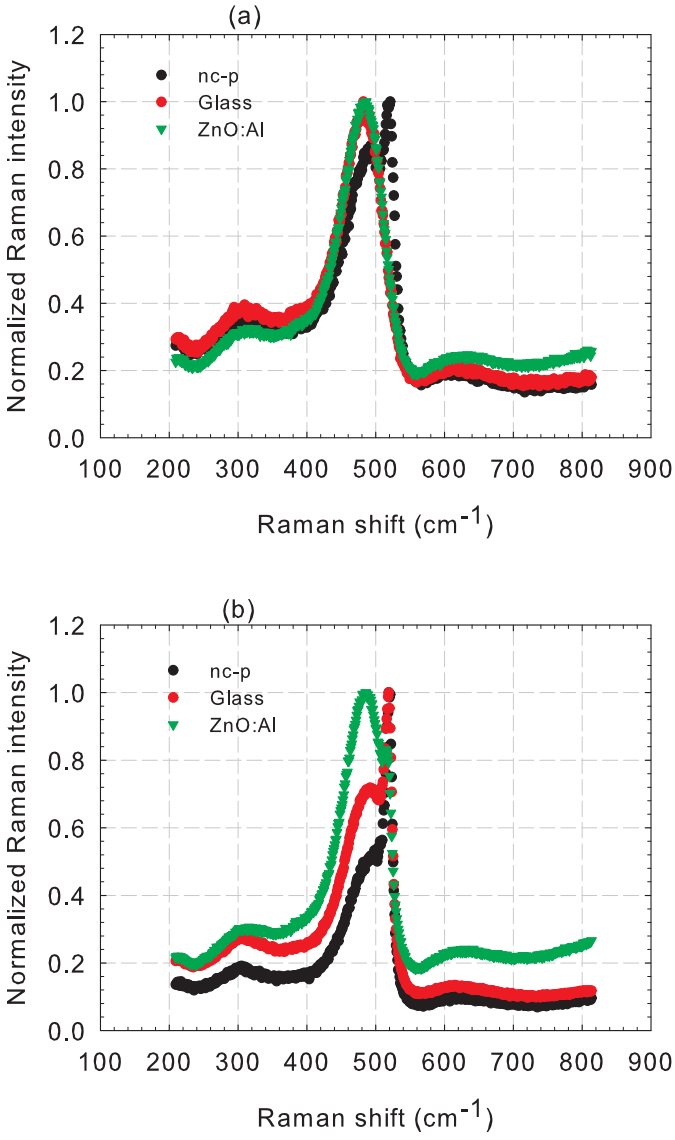

Figure 5.2: Bi-facial Raman spectra of unseeded nc-Si:H films on different substrates with measurements taken (a) from the glass side and (b) from the film side.

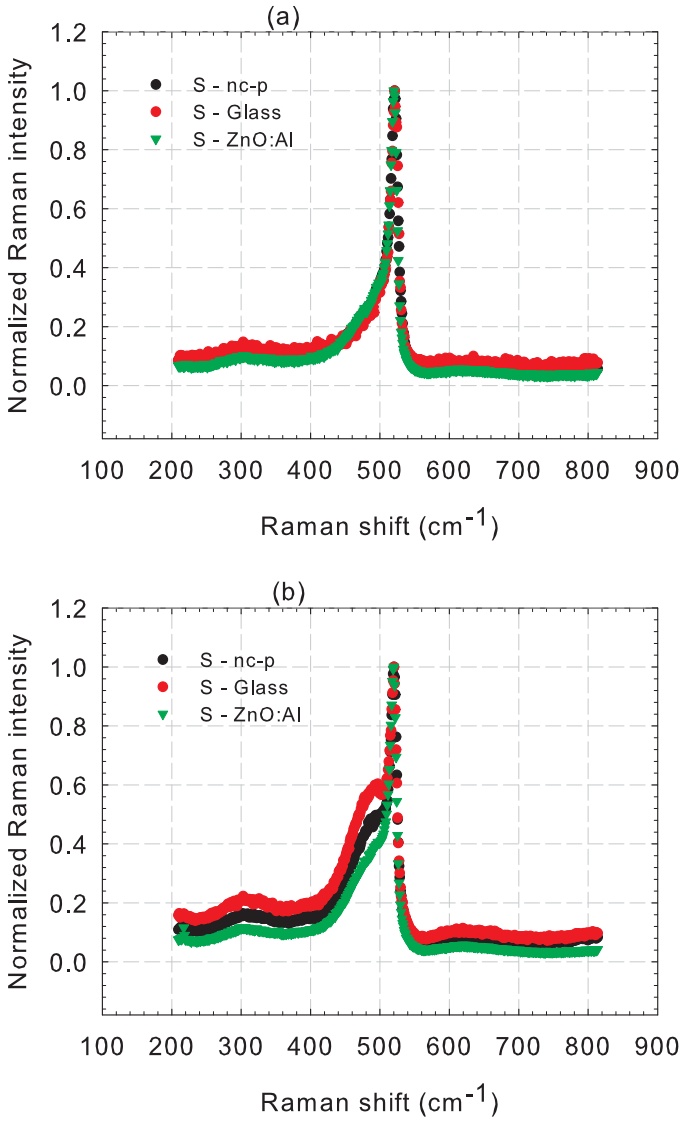

Figure 5.3: Bi-facial Raman spectra of seeded nc-Si:H films on different substrates with Raman measurement taken (a) from the glass side and (b) from the film side.

5.3.4 X-ray diffraction patterns of seeded nc-Si:H grown on different substrates

The x-ray diffraction pattern of both seeded and unseeded nc-Si:H layers deposited on the three substrates are shown in figure 5.4. The (111), (220), and (311) silicon lines typical of nc-Si:H [125] are observed in all layers with the (111) lines having the highest intensity counts. The integrated intensities of these lines can be related to the crystal orientation. Comparatively, we observe that the preferred crystal orientation of nc-Si:H grown on ZnO substrate is most affected by seeding. This we see in the intensity counts of its (111) and (220) lines relative to that of the other substrates in figure 5.4. For both layers deposited directly on glass and on glass with nc-Si:H p-layer (Figures 5.4(c) and 5.4(b), respectively) the preferred orientation of the crystals is not significantly affected by the use of seed layers. In the layer deposited on ZnO:Al (Figure 5.4(a)) the seed layer seems to induce a significant change in the orientation of the crystals as the intensity counts for Si(111) and Si(220) peaks also change significantly. Here, the (220) peak is more affected than the (111) peak with the (220) peak intensity increasing by over 300% as against 75% for the (111) peak.

The crystal sizes for the two sets of experiments determined from XRD have values in the range: 7-19 nm and the micro-strain between 3.6×10^{-3} and 12×10^{-3} with the biggest grain having the highest micro-strain. The micro-strain increases as the grain size increases due to increasing micro-stress with increases in grain size. We found no dependence of the crystal size and micro-strain on seeding for all the three substrates.

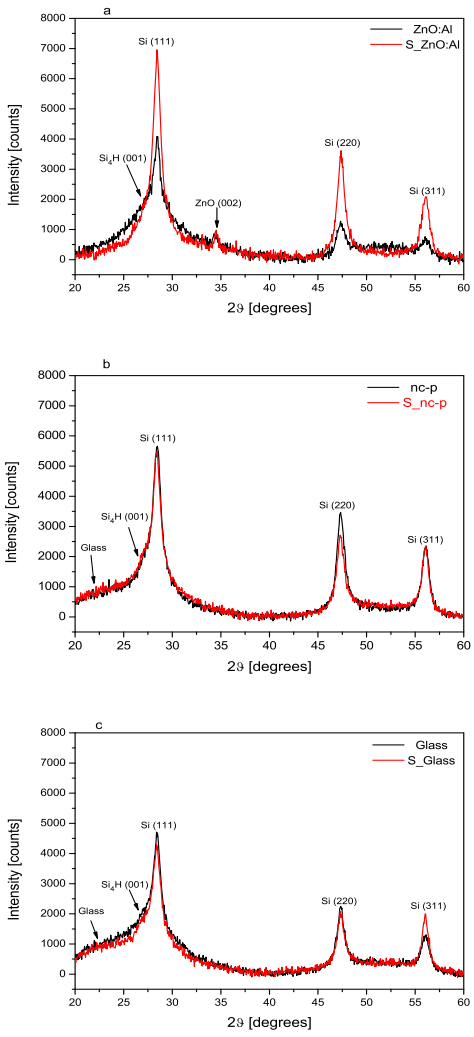

Figure 5.4: XRD pattern of nc-Si:H layers deposited on (a) ZnO:Al (b) nc-Si p-layer and (c) glass substrates with and without seed layers. The letter "S" as used in the legends represents the seeded layers.

5.4 Conclusions

Thin film nanocrystalline silicon is a mixed-phase and complex hydrogenated material comprising the amorphous tissue, crystals and voids. Its growth evolves through a number of intermediate phase changes. Phase changes in the growth of nc-Si:H represent different crystallinity levels in the material and as such the crystalline mass fraction can be an indicator of phase transitions. In the work reported here it has been demonstrated that ex-situ investigation of phase-change profiles in nc-Si:H is possible by means of depth-profile Raman measurement. The results show that when using rf PECVD the nc-Si:H growth begins with the amorphous incubation layer with gradual increase in crystallinity until saturation at the full nanocrystalline regime. Applying a seed layer reverses this order and makes it possible to grow nc-Si:H from onset of deposition without the intermediate phases. These effects were investigated for different underlying substrates and were found to still hold independent of the substrate. However, we observed that without seed layer the crystallinity development profile is substrate-dependent. Underlying substrate effect on crystallinity depth profile of nc-Si:H can be eliminated using seed layers. From XRD investigation the crystal structure is probed and we found no dependence of the crystal size and the micro-strain on the seed layer and on the nature of substrate. However, we observe a dependence of crystal orientation on seeding.

6 Chapter 6

Determination of preferred crystal orientation in thin film nc-Si:H using Raman spectroscopy

6.1 Introduction

The structural and material properties of nc-Si:H depend on its crystalline mass fraction and preferred orientation of its crystals [125, 126,]. Insight into nc-Si:H preferred crystal orientation is important as it gives an understanding of the growth process. Furthermore, physical properties such as conductivity are affected by the preferred crystal orientation and the general characteristics of nc-Si:H materials are dominated by the properties of the crystals with the preferred orientation [127].

Various techniques have been used to investigate the structure and composition of nc-Si:H and the preferred orientation of its crystals. X-ray diffraction (XRD) for instance has been widely applied in investigating the crystal structure of nc-Si:H. Transmission electron microscopy (TEM) [28, 44, 128, 129] has been applied also to probe the material structure of nc-Si:H. Although well-established, TEM is destructive, time-consuming, and expensive. Similarly XRD is not a fast measurement and the obtained diffraction pattern can easily be affected by impurities [130]. Analysis using computer programs for grain orientation determination from measured traces of crystallographic planes has been used [45]. This is however limited in that it is time-consuming, tedious and often applied only to a specific crystal plane.

Raman spectroscopy on the other hand is a fast, non-destructive technique that requires no sample preparation. Raman spectroscopy has a high spectral resolution with added features that allow for surface enhancement, polarization measurement and compatibility with aqueous samples [131]. It has wide application in estimating the degree of stress and disorder in thin-films [44, 46, 132] and the crystalline mass fraction, f in nc-Si:H [47]. This quantity gives

the fraction of silicon in the material that is in the crystalline phase. Qualitatively, it can give an indication of the different phase materials ranging from the amorphous, amorphous-to-nanocrystalline transition and the full crystalline phase materials as shown in figure 6.1. Typically, nc-Si:H film has a Raman spectrum with a peak at around 520 cm^{-1} depending on its crystalline mass fraction and an asymmetric broadening of its width and a tail towards lower wave numbers.

The use of Raman for predicting the crystal orientation has been proposed and is based on the intensity dependence of the Raman signal on the directions of the polarization vectors of the incident light relative to the crystallographic axes [48, 49]. Based on this characteristic polarization-dependent Raman intensity the crystal orientation in some materials has been determined [133, 134]. Lu et al. [79] investigated high temperature electron cyclotron resonance (ECR) PECVD samples with f over 72%. Its application in determining preferred orientation of crystals in complex mixed-phase radio frequency plasma enhanced chemical vapor deposition, rf PECVD nc-Si:H has not been reported to our knowledge. Hence, it is necessary to authenticate this approach in low temperature nc-Si:H films over a wider range of materials in terms of the crystal composition.

In this chapter, we demonstrate the possibility of determining preferred crystal orientation in nc-Si:H based on the analysis of polarized Raman spectroscopy (PRS) measurements. The intensity of the Raman peaks in the spectrum depends on the lattice vibration, which are in turn dependent on the polarization direction of the incident laser light and on the crystallographic grain orientations. It is this Raman intensity dependence on polarization of the incident laser light that is used to determine preferred orientations in crystals [84, 85]. The polarized Raman spectra of standard test silicon wafers of known orientations are used as references and the spectra of our nc-Si:H films are compared to a profile comprising a superposition of the three profiles obtained from the test reference wafers namely (111), (110) and (100) c-Si wafers. The comparison is based on the fit parameters obtained from a least-square fitting routine developed for the purpose. Results from this approach are compared to results obtained from XRD measurements.

In the first section of this chapter, a general introduction is given followed by a theoretical background to PRS measurements. In section 6.2 details of the deposition conditions of the experimental samples are laid out. The procedure followed for the Raman and x-ray diffraction measurements are presented. Section 6.3 contains a

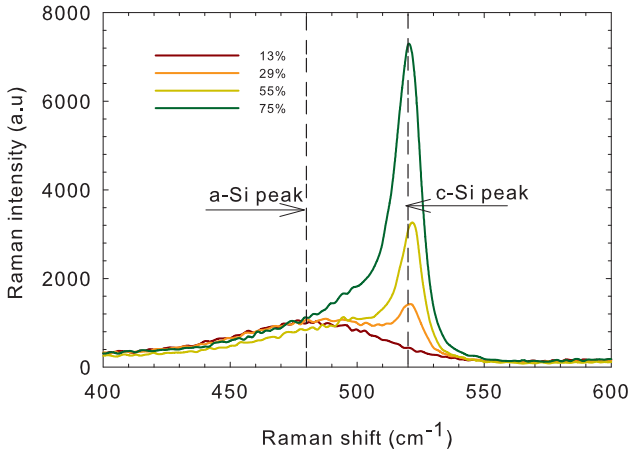

Figure 6.1: Raman profile of different phases of thin film silicon-based materials. The peak gets narrower as film crystalline mass fraction increases. Shifting peak position for different f (the legend) implies phase changes. The (TO) mode position in c-Si and a-Si:H are respectively 520 and 480 cm^{-1}.

description of the approach followed in order to calibrate and validate our measurement results. Measurements results are presented and discussed in section 6.4. The fitting procedure adopted is explained with the assumptions on which this is based. The fitting parameters obtained from the nc-Si:H samples are compared with that from standard wafers to give indication of the preferred crystal orientation.

6.2 Experimental details

The nc-Si:H films used in this experiment were deposited in the rf PECVD set up in our lab. Intrinsic nanocrystalline silicon layers were deposited on Corning glass (E2000) under varying silane concentration, S_c (S_c = $SiH_4/(SiH_4+H_2)$), while keeping the deposition pressure and substrate temperature at 9 mbar and 180 ^oC, respectively. The deposition power was also fixed at 542 mW/cm^2. The silane concentration varied between 1.2 to 1.7%. With these deposition conditions we obtained films with f in the range 10 to 76%. The crystalline mass fraction was extracted from the Raman spectrum by

using a peak-fitting approach to the model of Smit et al. [47]. The thicknesses of the layers were deduced from reflection and transmission measurements by fitting the interference fringes. For all experiments, the thicknesses of the nc-Si:H layers were between 500 and 700 nm. Two crystallized a-Si:H samples deposited by the expanding thermal plasma (ETP) technique were also investigated.

The Raman spectra of the films were measured using a Raman microscope (Renishaw InVia, grating 1800 lines/mm) in a 180^o back scattering geometry with a 25-mW Ar laser at a wavelength of 514 nm focused on a spot of about 1 μm.

For measurements under different polarization, a change in the polarization angle of the incident light is induced by a rotator incorporated in the system and placed in between the laser and spectrometer. The rotation angle was varied in steps of 2^o from 0 to 120^o. Due to a limitation in the turning mechanisms of the rotator, no measurements were recorded beyond 120^o. The incoming light was incident on the sample surface along the z axis at 0^o which corresponds to the direction perpendicular to the sample surface.

PRS was first carried out on single crystalline silicon wafers of [111], [110] and [100] orientations in order to establish the dependence of Raman intensities at the 520 cm^{-1} TO peak on rotation angle. We have chosen this phonon band because of its extreme sensitivity to local lattice characteristics [135]. Subsequently, measurements were carried out on all nc-Si:H samples for different polarization angle. For a reference randomly-oriented sample (RD), we measured crystalline silicon powder with particle size below 100 nm. For all PRS profiles, the effect of changing polarization angle on the Raman intensity was corrected.

For purposes of comparison, the preferred crystal orientation of nc-Si:H films was also determined by XRD analysis using an automatic powder diffractometer X'pert Pro with a thin film attachment (parallel beam, asymmetric geometry, fixed incident angle ω, 2θ-scan) and a proportional detector. Copper Kα characteristic radiation ($\lambda = 0.154$ nm) was used. The angle of incidence was fixed to 0.5^o and the detector moved with a constant step of 0.05^o from 15 to 65^o on the 2θ scale. The counting time was 20 seconds per step and the irradiated area of the sample was 15 mm × 15 mm.

6.3 Raman system calibration and validation test.

For each set of PRS measurements, we first carried out a system calibration and validation of the instrument response. The aim is to monitor and possibly correct for any system-induced effects in the measured Raman spectrum. To validate the Raman intensities, we followed the procedure as proposed by McCrery [131].

First we carried out reference measurements on a standard test sample, which in our case is a monocrystalline (110) silicon wafer to check for Raman intensity reproducibility and shift in peak intensity position. These effects can be corrected by an automated system calibration and sometimes with an auto-alignment of the laser. With the angular-dependent polarization measurement, a further calibration and correction was implemented. We checked the effect of the rotation of the rotator on the incident laser intensity by measuring the current generated on a photo-diode for each rotation step [85]. Using the linear dependence of the measured current on laser intensity [135] the Raman spectra were corrected for the laser intensity dependence on rotation angle. We have assumed that this correction takes care of all the rotation-induced effects that may arise from each of the relevant system components [131]. Becker et al. [85] have also shown that the grating effect on the Raman scattered light has no influence on the deduced crystal orientation from the Raman measurement. All Raman measurements were carried out at 5% of laser power, which is a pre-determined value at which we observed no laser-induced structural changes in our samples.

In order to further validate our method, we checked for the inherent rotational symmetries of the silicon crystals in the different Si wafers. We manually rotated the wafers about the *z*-axis through 360^{o} and carried out PRS measurements at angular intervals of 90^{o} until full rotation. Here we use the primary flat as the reference. After measurement, the wafer was turned through angle 90, 180 and 270^{o} for the subsequent measurements.

Figure 6.2 shows the Raman spectrum of (110) reference wafer used for the calibration of the system. These measurements were taken after carrying out an in-built system check and calibration, which examines the laser alignment and that of all the other components in the path of the laser propagation. We observed that the shift in the crystalline silicon peak position is around 1 cm^{-1}, which is within the acceptable deviation value reported in literature [47, 76]. The linearity of the Raman intensity with the laser power is also established in this

figure. Similar result (not shown) is observed for both (111) and (100) silicon wafers except for the differences in the Raman intensity count and associated broadening.

To check for the effect of PRS measurement-induced change on the structural property of measured nc-Si:H films, we compared the values of *f* obtained for each rotation angle investigated. A wide range of nc-Si:H samples with crystalline mass fraction ranging from 30 to about 70% were used and the results are presented in figure 6.3. Here we observe that for all investigated films, *f is* not affected by the PRS measurement as it shows no systematic dependence on the rotation angle. However, the figure also indicates an increasing scattering in the relation between *f* and rotation angle as the material changes from the highly crystalline to the amorphous regime. This can be tied to peak-fitting inaccuracies as the crystalline peak gets smaller with increasing amorphous fraction of the films. Non-dependence of *f* on rotation angle further indicates that there are no measurement-induced structural changes in the materials.

Figure 6.4 shows the PRS profile of the three test wafers taken to test for the rotational symmetry of the wafers. Here we observe that the amplitude of PRS profiles differs for the three different wafers. It decreases as the number of intercepting axes in the test c-Si wafers increases hence (100) profile has the highest amplitude for varying polarization angle and the (111) has the least. We observed that (100) maintains its four-fold symmetry since for the complete wafer rotation the PRS profile remains the same [136]. The peak intensity variation as a function of rotation angle shows a consistent maxima and minima points at around 45^o and 90^o respectively. The (110) and the (111) show two-fold rotational symmetry for each 180^o rotation.

The 3-fold rotation symmetry of the (111) wafer [137] can be observed from the similar Raman intensity value at 0 and 120^o rotation. While the (110) PRS profile indicates a shift in the maxima and minima points position for each rotation symmetry, the (111) maintains its maxima and minima positions for all rotations with much lower amplitude than both the (100) and the (110). This is a further indication that PRS profiles are unique depending on the crystallographic structure of the irradiated samples.

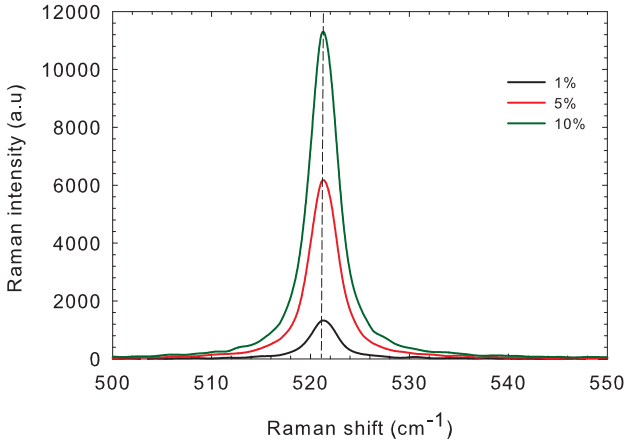

Figure 6.2: Raman intensity variation for 1%, 5% and 10% of the full laser intensity carried out on a (110) silicon wafer. The peak position deviates by about 1 cm^{-1} from the 520 cm^{-1} TO peak of crystalline silicon.

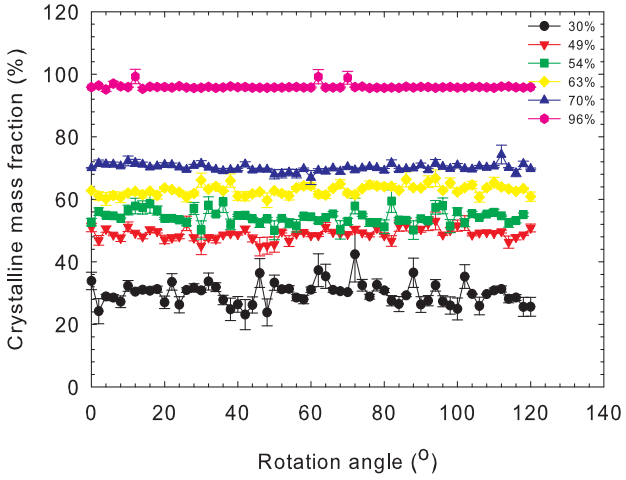

Figure 6.3: Crystalline mass fraction, *f* verses rotation angle for some selected experimental samples. The legend represents the crystalline mass fraction at 0 degree polarization.

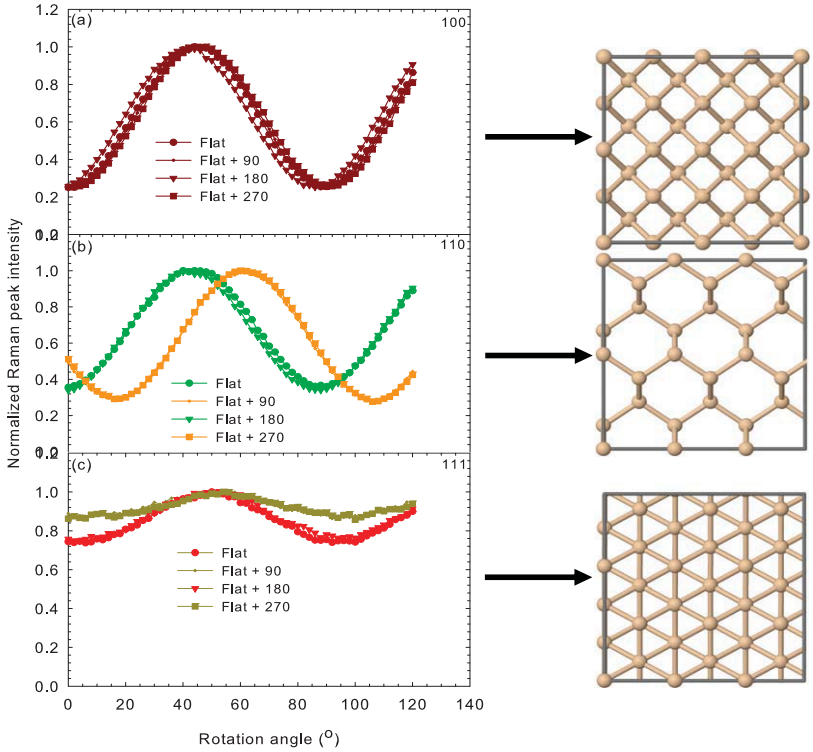

Figure 6.4: PRS profile of (a) (100) (b) (110) and (c) (111) c-Si test wafers. Flat as in the legend refers to the primary flat. The added values are the angles of rotation of the wafer with respect to the flat. "Flat + 90" means that the primary flat is rotated through 90 degrees. Similarly, "Flat + 180" and "Flat + 270" correspond to rotation of the primary flat through angles 180 and 270 degrees respectively.

6.4 Results and discussion

6.4.1 Data analyses

In analyzing the PRS measurement data, we use a relatively simple qualitative approach to determine preferred crystal orientation in nc-Si:H films. The analysis of the PRS measurement data involves least square fitting of the measured nc-Si:H profile to a unique profile obtained by superposition of (111), (110) and (100) data profiles obtained from the respective monocrystalline silicon wafers. The following assumptions were made:

1. Thin film nc-Si:H are composed of nano-crystals embedded in the amorphous matrix. The mass fractions of these crystals are expressed as a percentage of the entire material composition.
2. The structural properties of nc-Si:H are derived from the properties of its constituents. Hence we consider nc-Si:H to be a linear system. The constituents include crystal grains of varying orientations, grain boundaries, voids and the amorphous matrix. However, we consider only the crystal orientation, crystalline mass fraction and the amorphous matrix as Raman-active constituents.
3. The mixed-phase nature of nc-Si:H implies that its constituents retain their individual properties, thus they are independent and as such nc-Si:H can be treated as a linear system.
4. The most commonly detected crystal orientations in nc-Si:H are [111], [220] and [311], with the dominant orientation often being [111] or [220]. Based on this and also on the fact that we have reference crystalline silicon wafers only in [111], [110] and [100] orientations, our model is limited to detect only to these dominant orientations. In our approach, we take [110] to be equivalent to [220] except for the differences in their interplanar distances.
5. We assume that there is no contribution of the amorphous fraction to the preferred orientation in nc-Si:H.

If we consider mixed-phase nc-Si:H as a linear system, then we can apply the superposition principle as follows:

$$I_{nc}(\alpha) = a_{111} I_{111}(\alpha) + a_{110} I_{110}(\alpha) + a_{100} I_{100}(\alpha) \tag{6.2}$$

where I_{nc}, I_{111}, I_{110}, I_{100} are the normalized Raman intensity at 520 cm^{-1} TO peak as a function of rotation angle α, for the experimental nc-Si:H films and the (111), (110) and (100) test wafers respectively. a_{111}, a_{110} and a_{100} are best-fit parameters which are obtained on fitting I_{nc} to equation (6.2) by least square fitting algorithm. The best-fit parameters are obtained as unique parameters on a boundary condition

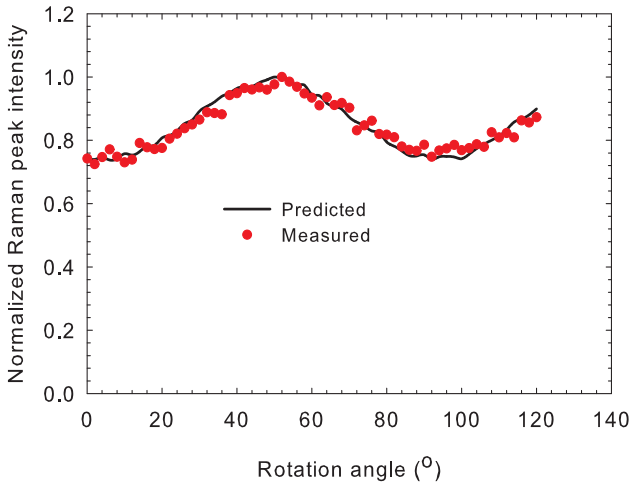

Figure 6.5: A comparison between experimental data obtained from the PRS measurement and a predicted data obtained from equation (6.2). The profile is that of a nc-Si:H sample with $f \sim$ 63%.

that their summation equals one and the least possible residual deviation from the experimental values is obtained. A very good agreement between the measured and the fitted profiles is obtained for most of the films. An example is presented in figure 6.5. In order to further verify our model, several *goodness-of-fit* tests are carried out. These are standard statistical model validity tests [138, 139] based on the residual, R, which is the difference between the observed and predicted value estimated from the regression equation. The least squares method chooses the parameter estimates such that the sum of the squared residuals is minimized.

Goodness-of-fit tests employed in this work include the sum of squares of the residual R^2, correlation coefficient CC, root mean square error $RMSE$, and the mean bias error, MBE. The detailed formulae of these tests as applied here are described in detail elsewhere [138]. For a good fit, R^2 and the error values of $RMSE$ and MBE approach zero. CC has values between 0 and 1 and gives indications of linearity of relationship between the dependent and the independent variables. A value of 1 implies a perfect fit and a strong relationship, while 0 means a bad fit and absence of any relation. Table 6.1 shows a summary of the test of validity indices and the fit parameters. This will be discussed in section 6.4.3.

Table 6.1: Details of the fit parameters obtained from the model of equation (6.2) and the *goodness-of-fit* test results for all the test samples. E1 and E2 are thin film silicon samples deposited by expanding thermal plasma (ETP) and R1 to R8 are nanocrystalline silicon samples deposited using rf PECVD.

Sample ID	f (%)	Fit parameters			Test of validity indices			
		a_{111}	a_{110}	a_{100}	R^2	*RMSE*	*CC*	*MBE*
[111]	-	1.0000	0.0000	0.0000	0.0000	0.0000	1.0000	0.0000
[110]	-	0.0000	1.0000	0.0000	0.0000	0.0000	1.0000	0.0000
[100]	-	0.0000	0.0000	1.0000	0.0000	0.0000	1.0000	0.0000
RD	96	1.0000	0.0000	0.0000	0.9062	0.1219	0.7318	0.1014
R1	30	0.6765	0.0000	0.3235	0.3716	0.0781	0.8741	0.0361
R2	49	0.9664	0.0000	0.0336	0.0512	0.0290	0.9570	0.0105
R3	54	0.9865	0.0135	0.0000	0.0268	0.0210	0.9719	0.0016
R4	60	0.8619	0.0000	0.1381	0.1858	0.0552	0.8877	0.0240
R5	63	1.0000	0.0000	0.0000	0.0594	0.0312	0.9748	0.0238
R6	67	0.8766	0.1234	0.0000	0.0557	0.0302	0.9544	0.0022
R7	70	0.9645	0.0000	0.0355	0.0202	0.0182	0.9805	0.0028
R8	73	1.0000	0.0000	0.0000	0.0448	0.0271	0.9755	0.0193
E1	92	0.8809	0.0993	0.0198	0.1657	0.0521	0.8691	0.0147
E2	95	0.9074	0.0926	0.0000	0.0722	0.0344	0.9374	0.0039

6.4.2 PRS spectra for (111), (110) and (100) reference silicon wafers.

The Raman intensity at 520 cm^{-1} as a function of rotation angle normalized to the maximum intensity is presented in figure 6.6 for the three silicon wafers and silicon powder (RD). Because our interest is in relating the Raman profile of the silicon wafers of known crystal orientation to the profile obtained in nc-Si:H films, we limited our comparison to measurements taken along the *z*-axis perpendicular to the primary flat because the primary flat has specific orientation relative to the wafer surface [140] and is present in all the test wafers. The variation in rotation angle results in a change in the polarization plane of incident light and hence affects the Raman scattering intensity [141]. We attribute this to the different degrees of scattering and energy distribution within the crystal lattice of the silicon wafers

depending on the crystal plane. The <111> plane has the largest number of silicon atoms per cm^2 (atomic lattice packing density) whereas <100> has the least number of atoms per cm^2 [142, 143]. If the bond density in the intercepting plane is high, this will result in a more even distribution of the Raman intensity with rotation angle, as more interactions between the plane and incident laser light are more likely. The least dependence of Raman intensity on rotation angle observed for the (111) wafer implies a more even distribution of the scattered light since it also has more bonds within the lattice than the (110) and the (100) lattices. Similarly, the (100) lattice has the least atomic bonds in its crystallographic structure and thus scatters the least of the incident light. RD shows no clear dependence on the laser polarization, which actually is due to its random structure as has also been earlier observed [79].

6.4.3 Predicting preferred crystal orientation in thin film nc-Si:H from Raman polarization spectra of reference test wafers

In figure 6.7 the PRS results of some of the experimental nc-Si:H films of different f are presented. A visual comparison of the plots of figure 6.7 shows that most of the nc-Si:H films have a profile similar to that of (111) Si wafer, which indicates that the films have mainly preferential [111] orientation. The fit parameters obtained for all the samples are shown in table 6.1 and are compared to the fit parameters of the test silicon powder, which we consider to have randomly-oriented crystals. Quantitatively, the orientation with the highest value of the fit parameter implies that such orientation is dominant in the film. From table 6.1 we observe that most of the test samples indicate the dominance of a [111] orientation with a_{111} values of about 90% or higher. For the film with f = 30% as in R1, a_{111} is still the highest fit parameter but drops to 0.677. These fit parameters are adjudged as correct by considering the test of validity indices. The near-zero values of R^2, RMSE and MBE indicate that the fitting error is minimal and high CC implies a strong correlation between the predicted and the experimental data. The fit parameters for RD suggest it has a dominance of [111] orientation. However, the *goodness-of-fit* test indicates that the fitting here falls below accepted values for a good fit.

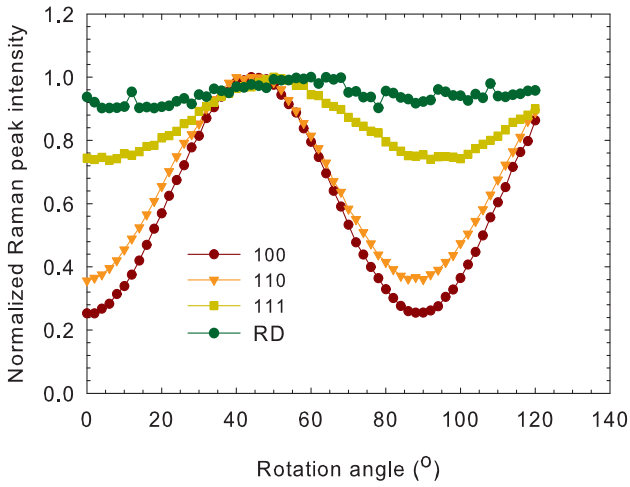

Figure 6.6: PRS profile of (111), (110) and (100) test monocrystalline silicon wafers and silicon powder (RD).

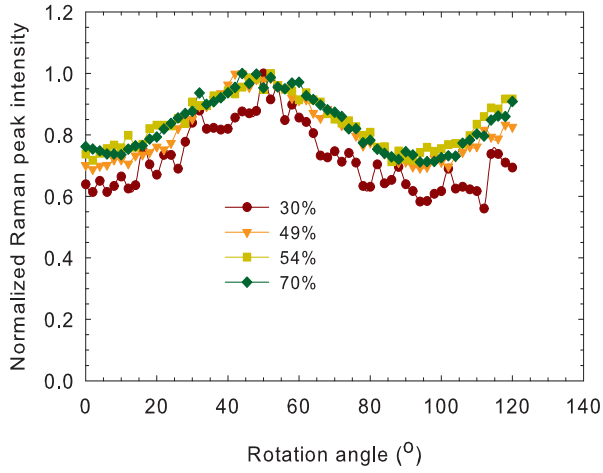

Figure 6.7: The PSR profile of selected nc-Si:H samples. The samples' crystalline mass fractions taken at 0 degree rotation are indicated in the legend.

This is corroborated by the over 90% value of R^2 and the lower *CC* value.

6.4.4 XRD analyses of test nc-Si:H films and comparison of results with Raman results

In figure 6.8, the result of the semi-quantitative XRD phase analysis carried out on all significant diffraction lines in 2ϑ-interval of 15-65 degrees of the test samples are presented. The figure 6.8(a) indicates that all films have a strong [111] orientation finger prints as the strongest peak and is observed at 2$\vartheta \sim 28^{o}$. The I(220)/I(111) intensity ratio is in the range: 0.53 - 0.81. This indicates that the nano-crystals have preferential orientation in the [111] direction; a feature in line with nc-Si:H deposited at the conditions described in section 6.2 [127]. The (111) intensity increases as *f* also increases in the films. The broadening of the (111) peak and its lower intensity for the material with $f = 30\%$ for instance is indicative of the amorphous fraction. Figure 6.8(b) shows the XRD pattern of the test random sample (silicon powder). In figure 6.8(b) we observe that the I(220)/I(111)) intensity ratio has a value of about 0.4 which indicates a much higher (111) intensities in the test random sample than in the nc-Si;H samples in figure 6.8(a). This suggests that the [111] oriented crystals mainly dominates the powder.

A comparison between *f* values obtained from Raman and that from XRD is presented in table 6.2. The *f* values from XRD were estimated by comparing integrated intensities of amorphous and crystalline components of the XRD patterns after separating the overlapped diffraction lines by curve fitting. Good agreement is observed for some samples, especially for the highly crystalline samples. The difference between *f* obtained from Raman and from XRD has also been earlier reported [144] and has been ascribed to the difference in the depth probed and in the sensitivity of the techniques. From the XRD results crystallite size (see table 6.2) was evaluated using (001) silicon hydride line and (111) silicon line as described in section 2.2.2. Crystal sizes in the range 4-17 nm were obtained and they seem to become larger as *f* increases.

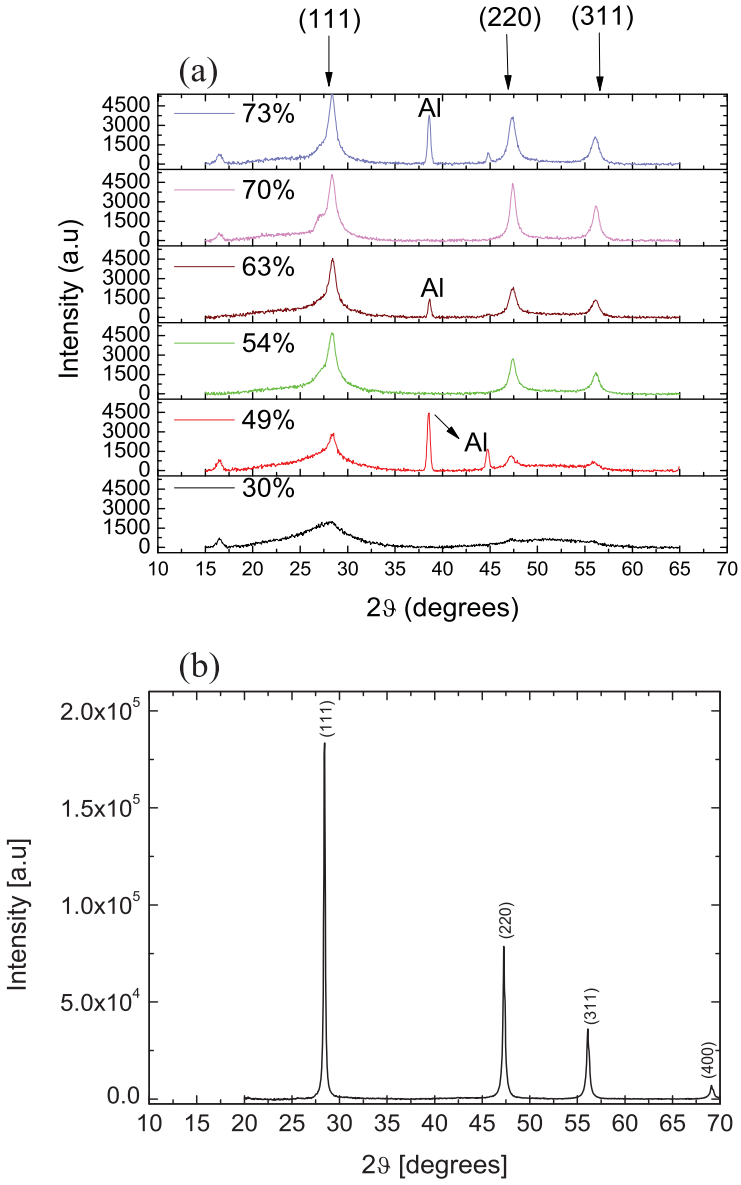

Figure 6.8: X-ray diffraction patterns of (a) nc-Si:H samples of different crystalline mass fraction, *f* (b) nanocrystalline silicon powder (RD). The legend in figure 6.8(a) represents the *f* value of each nc-Si:H sample.

Table 6.2: Comparison between the crystalline mass fractions obtained from Raman and that obtained from XRD.

f(%)		Crystal size (nm)
Raman	XRD	XRD
30	24	4.3
49	62	8.0
54	47	9.7
63	47	13.5
70	74	16.3
73	75	11.4

6.5 Conclusion

The use of Polarized Raman Spectroscopy for the investigation of preferred orientation of crystals in nc-Si:H has been demonstrated. This principle is based on the fact that a change in the polarization angle of the incident laser light on interaction with crystalline material of a given crystallographic structure generates a unique scattering profile which can give insight into the orientation of the irradiated crystals. Based on this we have investigated a wide range of nc-Si:H samples. These samples had crystalline mass fractions ranging from the 30 to over 70% and were mainly deposited using rf PECVD. For this work we have used the (111), (110) and (100) monocrystalline silicon wafers as reference orientations and obtained distinct PRS profiles for each wafer. We have applied the superposition principle by fitting the PRS profiles of our nc-Si:H samples to a linear combination of (111), (110) and (100) profiles. Using a least-squares fitting algorithm we inferred the preferred orientation of our nc-Si:H samples by comparing the fit parameters. Our results show that most of the samples have mainly a [111] preferred orientation and this is well corroborated by XRD measurements. This approach is simple and faster than other techniques used for inferring the orientation of crystals in nc-Si:H.

7 Chapter 7

General conclusions

- As a first step towards understanding the structure and characteristics of nc-Si:H, we investigate the effect of the rf PECVD deposition conditions on the material properties of nc-Si:H and its device performance. The structure and material properties of thin film nanocrystalline silicon are strongly dependent on the deposition conditions. These material properties include the crystalline mass fraction, the growth rate, activation energy and the dark conductivity. They have been shown to be affected by such deposition parameters as deposition power, deposition pressure, substrate temperature, and silane concentration.. We demonstrate (chapter 3) that using any of the above deposition parameters as a deposition variable, it is possible to grow device grade nc-Si:H film. However, the degree of the sensitivity of the material properties to the different deposition parameters varies and device grade films are made only in a sensitive process window. For materials deposited at the amorphous-to-nanocrystalline transition, but at different deposition settings, though they have similar crystalline mass fraction, their electrical properties show a substantial variation.

- The use of Raman microscopy in thin film nc-Si:H research has mainly been limited to determining crystalline mass fraction. Unfortunately, with this method no information can be obtained on the development of the crystalline mass fraction especially from onset of growth. The laser light is absorbed in the material and only probes part of the films, depending on the absorption coefficient of the material and the used wavelength. Therefore for thick solar cells the initial growth phases close to the substrate may not be probed. In this thesis we demonstrate (chapter 4) a systematic approach that enables to obtain the profile of the crystalline mass fraction in nc-Si:H by means of depth-profile Raman measurement. This approach makes it possible to carry out ex-situ investigation of phase-change profiles in nc-Si:H. The result of the depth profile measurement gives indication about the

plasma stablilization phase in terms of the crystalline mass fraction as function of the film thickness. During the stabilization phase the film growth evolves from the amorphous silicon incubation phase into the nanocrystalline regime, after which no further change in the crystalline mass fraction is observed. This relation between crystalline mass fraction and film thickness can be useful for process control during deposition.

- The underlying substrate on which nc-Si:H is grown can play a key role in modifying the growth process hence the material properties of nc-Si:H. We show (chapter 5) that the evolution of the crystalline mass fraction in nc-Si:H depends on the nature of substrate. Possibility of modifying the substrate effect has been demonstrated. Such modification results in a rapid and uniform evolution of the crystalline mass fraction in nc-Si:H films. The results show that under normal rf PECVD, nc-Si:H growth begins with an amorphous silicon incubation layer with gradual increase in crystalline mass fraction until saturation in the full nanocrystalline regime. Applying a thin layer with high crystalline mass fraction (deposited at very high hydrogen dilution of the silane precursor gas) as seed layer reverses this order and makes it possible to grow nc-Si:H from onset of deposition without the intermediate phases. We have used this seeding technique as tool to re-modify substrate morphology for rapid nucleation and a uniform depth profile of the crystalline mass fraction. Effects of this method are summarized as follows:
    - Rapid crystal nucleation that results in high and uniform development of the crystalline mass fraction in growth direction.
    - Suppression of the effect of substrate material on the growth process of nc-Si:H.
    - Complete elimination of the amorphous silicon incubation layer during film growth.
    - Increased performance of nc-Si:H solar cell.

- Determining the preferred crystal orientation in nc-Si:H is important in order to understand the growth mechanisms of nc-Si:H. Information about preferred orientation can be used as a fingerprint to determine material quality. X-ray diffraction (XRD) and transmission electron microscopy (TEM) are commonly used methods for this purpose. These methods are complex in their

approach, expensive and can be quite sensitive to impurities. The possibility to use Raman spectroscopy for obtaining preferred orientation in nc-Si:H is demonstrated in this thesis (chapter 6). This method is based on the polarization-dependent Raman spectroscopy (PRS); a simple but sensitive approach based on correlating and comparing the polarized Raman spectra of standard silicon wafers of known orientation to that of the polarized Raman profiles of the nc-Si:H samples. Based on this we have investigated a wide range of nc-Si:H samples. These samples had crystalline mass fraction ranging from the amorphous to the highly crystalline materials and were mainly deposited using rf PECVD. For this work we have used the [111], [110] and [100] monocrystalline silicon wafers as standard test crystalline structure and obtained distinct PRS profile for each wafer. We have applied superposition principle by adding up the PRS profiles of [111], [110] and [100] crystals obtained from the test wafers and comparing the resulting profile to that of our nc-Si:H samples. Using the least square fitting algorithm we inferred the preferred orientation of our nc-Si:H samples by comparing the fit parameters. Our result show that most of the samples have mainly a [111] preferred orientation and this is well corroborated by XRD measurements. This approach to determine dominant crystal orientation in nc-Si:H is simple and can be a useful tool in investigating the structure of nc-Si:H.

8 Bibliography

[1] International Energy Outlook 2011, (US Energy Information Administration,www.eia.gov).

[2] Renewable Energy World, **2** (4), (1999).

[3] World Energy Council Report (2010), (www.worldenergy.org)

[4] K. L. Chopra, P. D. Paulson and V. Dutta, *Progress in Photovoltaics: Research and Applications* **12**, 69 (2004).

[5] S. Klein, T. Repmann and T. Brammer, *Solar Energy* **77**, 893 (2004).

[6] B. Rech, T. Roschek, T. Repmann, J. Müller, R. Schmitz and W. Appenzeller, *Thin Solid Films* **427** , 157 (2003).

[7] L. Lawrence Kazmerski, *Journal of Electron Spectroscopy and Related Phenomena* **150**,105 (2006).

[8] *R. Street, Hydrogenated Amorphous Silicon,* Cambridge University Press, Cambridge, 1991.

[9] M. Zeman, *ASDAM Conference, Smolenice Castle,* Slovakia, October 14-16, 2002.

[10] D. Staebler and C.R. Wronski, *Applied Physics Letters* **31**, 292 (1977).

[11] R. E. I. Schropp and M. Zeman, *Amorphous and Microcrystalline Solar Cells: Modeling, Materials, and Device Technology*, Kluwer Academic Publishers, 1998.

[12] J. Meier, J. Spitznagel, U. Kroll, C. Bucher, S. Faÿ, T. Moriarty and A. Shah, *Thin Solid Films* **451-452**, 518 (2004).

[13] G. van Elzakker, *Hydrogenated amorphous silicon solar cells deposited from silane diluted with hydrogen,* PhD Thesis, Delft University of Technology, Delft, The Netherlands, (2010).

[14] O. Isabella, F. Moll, J. Krc and M. Zeman, *Physica Status Solidi (a)* **207** (3), 642 (2010).

[15] S. Vep ek and V. Mare ek, *Solid-State Electronics* **11**, 683 (1968).

[16] S. Usui and M. Kikuchi, *Journal of Non-crystalline Solids* **34**, 1 (1979).

[17] P. Torres, J. Meier, M. Goetz, N. Beck, U. Kroll, H. Keppner, and A. Shah, *Proceedings, Material Research Society Symposium* **452**, 883 (1996).

[18] A. Gordijn, *Microcrystalline silicon for thin film solar cells*, PhD Thesis, University of Utrecht, (2005).

[19] D. E. Carlson, *Journal of Non-crystalline Solids* **35-36**, 707 (1980).

[20] D. Domine, *The role of front electrodes and intermediate reflectors in the optoelcectronic properties of high-efficiency micromorph solar cells*, PhD Thesis, University of Neuchatel, Switzerland (2009).

[21] T. Soderstrom, *Single and multi-junction thin film silicon solar cells for flexible photovoltaics*, PhD thesis, University of Neuchatel, Switzerland, (2009).

[22] J. Meier, S. Dubail, R. Flückiger, D. Fischer, H. Keppner, and A. Shah, *Proceedings, Ist World Conference on Photovoltaic Energy Conversion*, Hawai, 409, (1994).

[23] O. Vetterl, F. Finger, R. Carius, P. Hapke, L. Houben, O. Kluth, A. Lambertz, A. Mück, B. Rech and H. Wagner, *Solar Energy Materials and Solar Cells* **62**, 97 (2000).

[24] K. Yamamoto, M. Yoshimi, Y. Tawada, S. Fukuda, T. Sawada, T. Meguro, H. Takata, T. Suezaki, Y. Koi, K. Hayashi, T. Suzuki, M. Ichikawa and A. Nakajima, *Solar Energy Materials and Solar Cells* **74**, 449 (2002).

[25] M.A. Green, K. Emery, Y. Hishikawa, W. Warta, and E. Dunlop, *Progress in Photovoltaics: Research and Applications* **20**, 12 (2012).

[26] Banerjee A, Su T, Beglau D, Pietka G, Liu F, DeMaggio G, Almutawalli S, Yan B, Yue G, Yang J, Guha S. *37th IEEE PVSC*, Seatlle, June 2011.

[27] E. Vallat-Sauvain, U. Kroll, J. Meier, N. Wyrsch and A. Shah, *Journal of Non-crystalline Solids* **266-269**, 125 (2000).

[28] J. Bailat, E. Vallat-Sauvain, L. Feitknecht, C. Droz and A. Shah, *Journal of Non-crystalline Solids* **299-302**, 1219 (2002).

[29] J. K. Rath, *Solar Energy Materials and Solar Cells* **76**, 431 (2003).

[30] S. Guha, *Solar Energy* **77**, 887 (2004).

[31] K. Lips, P. Kanschat and W. Fuhs, *Solar Energy Materials and Solar Cells* **78**, 513 (2003).

[32] F. Finger, J. Müller, C. Malten, R. Carius and H. Wagner; *Journal of Non-crystalline Solids* **266-269**, 511 (2000).

[33] N. H. Nickel, and E.A. Schiff, *Physical Review B* **58**, 1114 (1998).

[34] A. Shah, J. Meier, P. Torres, U. Kroll, D. Fischer, N. Beck, N. Wyrsch, and H. Keppner, 26th Photovoltaic Specialist Conference, September 30 - October 3,1997; Anaheim, CA

[35] S. N. Agbo, J. Krč, R. A. C. M. M. van Swaaij, M. Zeman, *Solar Energy Materials and Solar cells* **94**, 1864 (2010).

[36] A. V. Shah, J. Meier, E. Vallat-Sauvain, N. Wyrsch, U. Kroll, C. Droz and U. Graf, *Solar Energy Materials and Solar Cells* **78**, 469 (2003).

[37] M.N. van den Donker, T. Kilper, D. Grunsky, B. Rech, L. Houben, W.M.M. Kessels and M.C.M. van de Sanden, *Thin Solid Films* **515** ,7455 (2007).

[38] N. Layadi, P. Roca i Cabarrocas, and B.Drevillon, *Physical Review B*, **52**, 5136 (1995).

[39] S. N. Agbo, S. Dobrovolskiy, G. Wegh, R. A. C. M. M. van Swaaij, F. D. Tichelaar, P. Sutta and M. Zeman, *Progress in Photovoltaics: Research and Applications* (2011)- Under review.

[40] R.W. Collins and B.Y. Yang, *Journal of Vacuum Science and Technology B* **7** 1155 (1989).

[41] R. W. Collins, A. S. Ferlauto, G. M. Ferreira, Chi Chen, Joohyun Koh, R. J. Koval, Yeeheng Lee, J. M. Pearce, C. R. Wronski, *Solar Energy Materials and Solar Cells* **78**, 143 (2003).

[42] Y. Mai, S. Klein, R. Carius, J. Wolff, A. Lambertz, F. Finger, and X. Geng, *Journal of Applied Physics* **97**, 114913 (2004).

[43] K.G. Kiriluk, D.L. Williamson, P.C. Taylor, B. Yan, G. Yue, J. Yang, S. Guha, *Journal of Non-crystalline Solids* **357**, 2587 (2011).

[44] Y. Sobajima, S. Nakano, M. Nishino, Y. Tanaka, T. Toyama, and H. Okamoto, *Journal of Non-crystalline Solids* **354**, 2407 (2008).

[45] H.S. Fong, *Journal of Material Science* **22**(7), 2363 (1987).

[46] N. Hayazawa, M. Motohashi, Y. Saito, H. Ishitobi, A. Ono, T. Ichimura, P. Verma and S. Kawata, *Journal of Raman Spectroscopy* **38**, 684 (2007).

[47] C. Smit, R. A. C. M. M. van Swaaij, H. Donker, A. M. H. N. Petit, W. M. M. Kessels and M. C. M. van de Sanden, *Journal of Applied Physics* **94**(5), 3582 (2003).

[48] K. Mizoguchi and S. Nakashima, *Journal of Applied Physics* **65**(7), 2583 (1989).

[49] T.V. Basova and B.A. Kolesov, *Thin Solid Films* **325**, 140 (1998).

[50] H. Fujiwara, M. Kondo, and A. Matsuda, *Physical Review B* **63**, 115306 (2001).

[51] O. Vetterl, M. Hulsbeck, J. Wolff, R. Carius and F. Finger, *Thin Solid Film* **427**, 46 (2003).

[52] C. Ross, Y. Mai, R. Carius and F. Finger, *Progress in Photovoltaics: Research and Application* **19**, 715 (2011).

[53] S. Veprek, *Thin Solid Films* **130** ,135 (1985).

[54] A. Matsuda, *Journal of Non-crystalline Solids* **338-340**, 1 (2004).

[55] S. Guha and J. Yang, *Journal of Non-crystalline Solids* **352**, 1917 (2006).

[56] R. W. Collins and A. S. Ferlauto, *Current Opinion in Solid State and Materials Science* **6**, 425 (2002).

[57] T. Roschek, T. Repmann, J. Müller, B. Rech, and H. Wagner, *Journal of Vacuum Science and Technology A* **20**, 492 (2002).

[58] M. Kondo, *Solar Energy Materials and Solar Cells* **78**, 543 (2003).

[59] M. Kondo, T. Matsui, Y. Nasuno, H. Sonobe and S. Shimizu, *Thin Solid Films* **501**, 243 (2006).

[60] M. Kondo, M. Fukawa, L. Guo and A. Matsuda, *Journal of Non-crystalline Solids* **266-269**, 84 (2000).

[61] L. Guo, M. Kondo, M. Fukawa, K. Saitoh and A. Matsuda, *Japanese Journal of Applied Physics* **37**, L1116 (1998).

[62] A. V. Shah, *Progress in Photovoltaic: Research and Applications* **12**, 113 (2004).

[63] A. Matsuda, *Journal of Non-crystalline Solids* **59-60**, 767 (1983).

[64] T. Matsui, M. Kondo and A. Matsuda, *Japanese Journal of Applied Physics* **42**, L901 (2003).

[65] T. Roschek, Microcrystalline silicon solar cell prepared by 13.56 MHz PECVD, PhD Thesis, Institute for Photovoltaics, Forschungzentrum Julich, (2003).

[66] R.H. Klazes, M.H.L.M. van den Broek, J. Bezemer and S. Radelaar, *Philosophical Magazine B* **45(4)** (1982) 377.

[67] J. Tauc, R. Grigorovici, and A. Vancu, *Physica Status Solidi (b)* **15**(2), 627 (1966).

[68] M. Vanecek, A. Poruba, Z. Remes, N. Beck and M. Nesladek, *Journal of Non-crystalline Solids* **227-230**, 967 (1998).

[69] J. I. Langford, *Journal of Applied Crystallography* **11**, 10 (1978).

[70] J. I. Langford, A. Boultif, J. P. Auffrédic and D. Louër, *Journal of Applied Crystallography* **26**, 22 (1993).

[71] R. Delhez, Th. H. de Keijser, and E. J. Mittemeijer, *Fresenius Zeitschrift für Analytische Chemie* **312**, 1 (1982).

[72] R. Delhez, Th. H. de Keijser, and E. J. Mittemeijer, *Surface Engineering* **3**(4), 331 (1987).

[73] S. Ram, S. Kumar and P. Roca i Cabarrocas, *Thin Solid Films* **515,** 7469 (2007).

[74] C.V. Raman and K.S. Krishnan, *Nature* **121**(3048), 501 (1928).

[75] Renishaw User guide, M/8012/1798/02).

[76] C. Droz, Thin film microcrystalline silicon layers and solar cells: microstructure and electrical performances, PhD thesis, University of Neuchatel, (2003).

[77] C. Droz, E. Vallat-Sauvain, J. Bailat, L. Feitknecht, J. Meier, and A. Shah, *Solar Energy Materials and Solar Cells* **81**, 61 (2004).

[78] T. D. Kang, Hosun Lee, S.J. Park, J. Jang, Soonil Lee, *Journal of Applied Physics* **92**, 2467 (2002).

[79] Z. Q. Lu, T. Quinn, H.S. Reehal, *Journal of Applied Physics* **97**, 033512 (2005).

[80] G. L. Squires, Practical physics, 3rd Edition, Cambridge University press, 1985.

[81] W. Hayes, R. Loudon, Scattering of light by crystals. Wiley, New York (1978).

[82] J. B. Hopkins, L. A. Farrow, and G.J. Fisanick, *Applied Physics Letters* **44**(5), 535 (1984).

[83] G. Kolb, T. Salbert, and G. Abstreiter, *Fresnel Journal of Analytical Chemistry* **341**, 166 (1991).

[84] W. Salcedo, F. Fernandez and J. Rubim, *Journal of Raman Spectroscopy* **30**, 29 (1999).

[85] M. Becker, H. Scheel, S. Christiansen, and H.P. Strunk, *Journal of* Applied Physics **101**, 063531 (2007).

[86] M. Green, Operating Principles, Technology and System Applications, University of the New South Wales, February, 1992.

[87] http://pveducation.org/pvcdrom. [Acessed on: 25 May, 2011].

[88] M. Faraji, S. Gokhale, S. Choudhari, M. Takwale, S. Ghaisas, *Applied Physics Letters* **60**, 3289 (1992).

[89] M. A. Green, K. Emery, Y. Hishikawa, W. Warta, *Progress in Photovoltaics: Research and Applications* **16**, 61 (2008).

[90] T. Kamei, M. Kondo, and A. Matsuda, *Japanese Journal of Applied Physics* **37**, L265 (1998).

[91] B. Rech, T. Repmann, J. Hupkes, M. Berginski, H. Stiebig, W. Beyer, V. Sittinger F. Ruske, *Proceedings, 20th European Photovoltaic Solar Energy Conference*, Barcelona, pp. 1481–1486, (2005).

[92] M. Python, D. Domine, T. Soderstro¨m, F. Meillaud and C. Ballif, *Progress in Photovoltaics: Research and Applications* **18**, 491 (2010).

[93] G. Bugnon, A. Feltrin, F. Meillaud, J. Bailat, and C. Ballif, *Journal of Applied Physics* **105**, 064507 (2009).

[94] E. Amanatides, D. Mataras, and D.E. Rapakoulias, *Thin Solid Films* **383**, 15 (2001).

[95] H. Miyahara, M. Takai, T. Nishimoto, M. Kondo, and A. Matsuda, *Solar Energy Materials and Solar Cells* **74**, 351 (2002).

[96] E. Amanatides, D. Mataras, D. Rapakoulias, M.N. van den Donker, B. Rech, *Solar Energy Materials and Solar Cells* **87**, 795-805 (2005).

[97] M. N. van den Donker, B. Rech, F. Finger, W.M.M. Kessels, M.C.M. van de Sanden, *Applied Physics Letters* **87**, 263503 (2005).

[98] S. N. Agbo, R.A.C.M.M. van Swaaij, M. Zeman, *Proceedings of the 11th Annual Workshop on Semiconductor Advances for Future Electronic and SENSORS (SAFE)*, Veldhoven, Netherlands, pp. 440–443, (2008).

[99] T. Matsui, T. Fujibayashi, Y. Nasuno, H. Fukuhori, Y. Kanemitsu, M. Kondo, A.Matsuda, *Proceedings of the Third World Conference on Photovoltaic Energy Conversion*, Osaka, pp. 1831–1834 (2003).

[100] S. Klein, Friedhelm Finger, and Reinhard Carius, *Journal of Applied Physics* **98**, 024905 (2005).

[101] S. Hamma and P. Roca i Cabarrocas, *Solar Energy Materials and Solar Cells* **69**, 217 (2001).

[102] S. N. Agbo, R. A. C. M. M. van Swaaij, and M. Zeman, *Proceedings of the 25th European Photovoltaic Solar Energy Conference*, Valencia, pp. 3288–3291, (2010).

[103] T. Fujibayashi, M. Kondo, *Journal of Applied Physics* **99**, 043703 (2006).

[104] T. Toyama, W. Yoshida, Y. Sobajima, H. Okamoto, *Journal of Non-crystalline Solids* **354**, 2204 (2008).

[105] S. C. Lee, *Journal of Applied Physics* **55** (12), 4426 (1984).

[106] M. Kondo, T. Matsui, Y. Nasuno, *Proceedings of the Thirty First IEEE Photovoltaic Specialists Conference*, Florida, USA, pp. 1377–1382 (2005).

[107] B. Kaplan, *Physica B* **351**, 90 (2004).

[108] S. Miyazaki, Y. Osaka, and M. Hirose, *Solar Energy Materials* **11** , 85 (1984).

[109] J. K. Rath, L. A. Klerk, A. Gordijn and R. E. I. Schropp, *Solar Energy Materials and Solar Cells* **90**, 3385 (2006).

[110] R. Vanderhaghen, S. Kasouit, J. Damon-Lacoste, F. Liu, and P. Roca i Cabarrocas, *Journal of Non-crystalline Solids* **338-340**, 336 (2004).

[111] M. N. van den Donker, B. Rech, F. Finger, L. Houben, W. M. M. Kessels and M. C. M. van de Sanden, *Progress in Photovoltaics: Research and Applications* **15**, 291 (2007).

[112] J. Koh, A. S. Ferlauto, P. I. Rovira, C. R. Wronski, and R. W. Collins, *Applied Physics Letters* **75**, 2286 (1999).

[113] A. S. Ferlauto, R. J. Koval, C. R. Wronski, and R. W. Collins, *Applied Physics Letter* **80**, 2666 (2002).

[114] A. Sarker, C. Banerjee, and A.K. Barua, *Solar Energy Materials and Solar Cells* **86**, 365 (2005).

[115] J. Zhou, K. Ikuta, T. Yasuda, T. Umeda, S. Yamasaki and K. Tanaka, *Applied Physics Letter* **71**, 1534 (1997).

[116] Y. Li, L. Li, J. Anna Selvan, A. Delahoy and R. Levy, *Thin Solid Film* **483**, 84 (2005).

[117] P. Roca i Cabarrocas, A. Fontcuberta, B. Kalache and S. Kasouit, *Solid State Phenomena* **93**, 257 (2003).

[118] N. Madhumita, P. Roca i Cabarrocas, E.V. Johnson, A. Abramov and P. Chatterjee, *Thin Solid Film* **516**, 6974 (2008).

[119] P. Roca i Cabarrocas, N. Layadi, T. Heitz, B. Drevillon, I. Solomon, *Applied Physics Letter* **66**, 3609 (1995).

[120] H. L. Hwang, K.C.Wang, K.C. Hsu, T.-R. Yew and J.J. Loferski, *Progress in Photovoltaics: Research and Applications* **4**, 165 (1996).

[121] J. Mullerova, L. Prusakova, M. Netrvalova, V. Vavrunkova, and P. Sutta, *Applied Surface Science* **256**, 5667 (2010).

[122] Y. Zhao and J. Zhang, *Journal of Applied Crystallography* **41**, 1095 (2008).

[123] M. Python, O. Madani, D. Domine, F. Meillaud, E. Vallat-Sauvain and C. Ballif, *Solar Energy Materials and Solar Cells* **93**, 1714 (2009).

[124] S. K. Ram, Md. N. Islam, P. Roca i Cabarrocas and S. Kumar, *Thin Solid Films* **516** (20), 6863 (2008).

[125] S. Schicho, F. Kohler, R. Carius and A. Gordijn, *Solar Energy Materials and Solar cells* **98** 391(2012).

[126] T. Kaneko, M. Wakagi, K. Onisawa, and T. Minemura, *Applied Physics Letters* **64**, 1865 (1994).

[127] H. Kakinuma, *Journal of Vacuum Science and Technology A* **13**(15), 2310 (1995).

[128] J. Müllerovà, S. Jurečka, and P. Šutta, *Solar Energy* **80**(6), 667 (2006).

[129] L. Houben, M. Luysberg, P. Hapke, O. Vetterl, F. Finger, R. Carius and H. Wagner, *Journal of Non-crystalline Solids* **227-230**, 896 (1998).

[130] N. Takesue and H. Chen, *Journal of Applied Physics* **76**, 5856 (1994).

[131] R.L. McCrery, John Wiley and Sons, Inc., Canada, 2000.

[132] I. De Wolf, *Semiconductor Science and Technology* **11**, 139 (1996).

[133] J. Dowdy, J.J. Hoagland and K.W. Hipps, *Journal of Physical Chemistry* **95**, 3751 (1991).

[134] N.E. Schlotter, J.F. Rabolt, *Journal of Physical Chemistry* **88**, 2062 (1984).

[135] J. Hopkins and L. Farrow, *Journal of Applied Physics* **59**(4), 1103 (1986).

[136] http://en.wikipedia.org/wiki/Crystal_structure. (Accessed: 10 November, 2011).

[137] A. Dadgar, F. Schulze, M. Wienecke, A. Gadanez, J. Blasing, P. Veit, T. Hempel, A. Diez, J. Christen and A. Krost, *New Journal of Physics* **9**, 389 (2007).

[138] M. Iqbal, An Introduction to Solar Radiation. Academic Press: Toronto, Canada, 1983.

[139] C. Huang, *Journal of Atmospheric and Terrestrial Physics* **26**, 959 (1964).

[140] http://www.phy.duke.edu/~hx3/physics/silicon/silicon.htm (Accessed: 11 September, 2011).

[141] G. Irmer, *Journal of Applied Physics* **76**(12), 7768 (1994).

[142] B. Sharma, Crystal growth-bulk and epitaxial film-part 3, http://cnx.org/content/m34202/1.2 (Accessed: 23 November, 2011).

[143] A. E. Franke, M. Sc Thesis, Massachusetts Institute of Technology, 1997.

[144] A.M. Funde, N. Ali Bakr, D.K. Kamble, R.R. Hawaldar, D.P. Amalnerkar, and S.R. Jadkar, *Solar Energy Materials and Solar Cells* **92**, 1217 (2008).

Summary

The need for electrical energy is growing fast as a result of the expanding world population and economic activities. On top of this the energy need of each individual is also growing. At present the growth in energy demand is not matched by the growth in energy generation because of insufficient energy production. This energy gap therefore needs to be bridged. In addition, most conventional means of energy generation are not environmentally-friendly and in turn affect human lives.

Solar energy is one of the alternatives for renewable energy generation. It can be extracted directly in electrical form from solar radiation using photovoltaic (PV) solar cells or solar concentrators. The PV market is dominated by crystalline-silicon based solar cells. However, thin-film silicon solar cells are becoming increasingly important, because they are deposited at relatively low temperatures and as such offer the possibility to produce flexible and light-weight solar panels. The latter can be applied on for instance the roofs of factory buildings.

Thin film nanocrystalline silicon (nc-Si:H) is an important material for application in thin-film silicon solar cells. It has been mainly developed because unlike amorphous silicon (a-Si:H) it is stable against light-induced degradation, and because with this material the solar cells have an extended spectral response up to the infrared wavelength region. Because of this extended response nc-Si:H films are used in combination with a-Si:H to form multi-junction solar cells, leading to an increased solar-cell efficiency. The focus of this thesis is on the development and characterization of nc-Si:H layers and solar cells.

In chapter 3 we present results of research on how the deposition parameters during the growth affect nc-Si:H material properties and device performance when using radio frequency plasma enhanced chemical vapor deposition. Particular attention is paid to p-type and intrinsic films and their application in nc-Si:H solar cells. For the p-layer development, the effects of deposition power, the substrate roughness, and doping are investigated. Intrinsic layer investigation focused on the effect of substrate temperature, deposition power, deposition pressure, and the gas-flow ratio. Intrinsic layers deposited at the amorphous-to-nanocrystalline transition during growth are investigated in detail. At this transition nc-Si:H films with favorable

properties for application in thin film solar cells can be made. Within our growth regime, this transition shows high sensitivity to the deposition parameters hence narrowing the process window. We show that materials deposited at the amorphous-to-nanocrystalline transition, but at different deposition settings, can have similar crystalline mass fraction while showing different electrical properties.

In chapter 4 we present how seed layers are used to enhance crystal nucleation at the onset of nc-Si:H growth. By this approach, uniform and rapid evolution of the crystalline mass fraction as a function of thickness is obtained. Our results show a possibility to grow thin-film nc-Si:H without the usual amorphous incubation layer. A depth profile Raman technique that enables the ex-situ investigation of the crystalline mass fraction depth profile in nc-Si:H films is presented. This approach reveals different growth phases in the development of nc-Si:H. From transmission electron microscopy (TEM) analyses, we observe that crystal sizes are not affected by seed layers. However, horizontal cracks are observed to dominate the early growth of nc-Si:H in p-i-n solar cells and this effect is reduced upon seeding. For the n-i-p cells the appearance of these cracks is not affected by seeding. X-ray diffraction (XRD) results indicate that the use of seed layers does not affect the crystal size, but affects the preferential orientation of the crystals. Solar-cell external parameters show that seeding of p-i-n solar cells leads to an increase in solar cell efficiency, mainly due to increase in the short-circuit current density.

The investigation of seeding on the crystallinity development is further extended in chapter 5. Here, we show that different substrates have different profile for the development of the crystalline mass fraction. For the three substrates investigated, we found a gradual development of the crystalline mass fraction, starting from the amorphous incubation layer. By means of seeding, rapid nucleation is observed as indicated by the high value of the crystalline mass fraction from the onset of growth. The effect of the substrate is reduced as all three substrates show a similar development profile of the crystalline mass fraction upon seeding.

In the last chapter of this thesis, the possibility to use Raman spectroscopy to determine the preferred crystal orientation in nc-Si:H is demonstrated. The preferred orientation of crystals in nc-Si:H can give insight into the film growth mechanism and is often determined from transmission electron microscopy and x-ray diffraction. The method presented in this thesis is based on the fact that molecular vibrations in films under polarized light give rise to polarization-

dependent Raman scattering intensity, depending on the grain crystal orientation of the irradiated material. This approach has been tested on a series of nc-Si:H samples and the results comparable with x-ray diffraction results.

Samenvatting
(Summary in Dutch)

Als gevolg van de groei van de wereldbevolking en de economische bedrijvigheid groeit de behoefte aan elektrische energie snel. Bovendien groeit de energiebehoefte per individu. Momenteel gaat de groei van de energieproductie niet gelijk op met de groei van de vraag naar energie. Deze energiekloof moet daarom worden overbrugd. Daarnaast zijn de meeste conventionele manieren van energieopwekking niet milieuvriendelijk en hebben op hun beurt invloed op het leven van individuen.

Zonne-energie is één van de alternatieven voor de opwekking van hernieuwbare energie. Het kan in elektrische vorm worden gewonnen uit zonnestraling met behulp van fotovoltaïsche (*photovoltaic*, PV) zonnecellen en zonneconcentratoren. De PV-markt wordt gedomineerd door zonnecellen gebaseerd op kristallijn silicium. Echter, zonnecellen gebaseerd op dunne lagen van silicium worden gedeponeerd bij relatief lage temperaturen en maken het mogelijk om flexibele en lichtgewicht zonnepanelen produceren. Deze kunnen bijvoorbeeld worden toegepast op het dak van fabriekshallen.

Nanokristallijn silicium (nc-Si:H) is een belangrijk materiaal voor toepassing in zonnecellen dunne silicium lagen. Het wordt voornamelijk ontwikkeld omdat het, in tegenstelling tot amorf silicium (a-Si:H), stabiel is tegen lichtgeïnduceerde degradatie en omdat het de spectrale respons van zonnecellen verbreedt tot in het infrarode golflengtegebied. Door deze bredere respons worden nc-Si:H lagen gebruikt in combinatie met a-Si:H films in zogenaamde multi-junctie zonnecellen, wat leidt tot een hoger zonnecelrendement. Dit proefschrift is geconcentreerd op de ontwikkeling en karakterisering van lagen en zonnecellen van nc-Si:H.

In hoofdstuk 3 onderzoeken we de filmgroei tijdens radiofrequentie plasma-geassisteerde chemische dampdepositie. In het bijzonder onderzoeken we de invloed van depositieparameters op de eigenschappen van het nc-Si:H en op de prestaties van zonnecellen. We besteden hoofdzakelijk aandacht aan p-type en de intrinsieke lagen en hun toepassing in nc-Si:H zonnecellen. Voor de ontwikkeling van de p-laag onderzoeken we de invloed van het depositievermogen, de ruwheid van het substraat en de dotering. Voor de groei van de intrinsieke laag onderzoeken we de invloed van de

substraat-temperatuur, het depositievermogen, de depositiedruk en de gassamenstelling. We besteden bijzondere aandacht aan intrinsieke lagen die gegroeid zijn onder omstandigheden waarbij het verkregen materiaal nabij de overgang tussen amorf en nanokristallijn ligt. Bij deze overgang kunnen nc-Si:H lagen worden gemaakt met gunstige eigenschappen voor zonneceltoepasingen. Binnen ons groeiregime vertoont deze overgang een hoge gevoeligheid voor de depositieparameters, waardoor het procesvenster klein is. We laten zien dat de elektrische eigenschappen van materialen gedeponeerd bij de overgang tussen amorf en nanokristallijn silicium afhangen van de depositie-instellingen, terwijl deze materialen een vergelijkbare kristalfractie hebben.

In hoofdstuk 4 laten we zien hoe we entlagen gebruiken om kristalnucleatie tijdens het begin van de nc-Si:H groei te beïnvloeden. Door deze aanpak wordt een uniforme en snelle ontwikkeling van de kristalfractie als functie van de laagdikte verkregen. Onze resultaten laten zien dat het mogelijk is om dunne lagen nc-Si:H te groeien zonder de gebruikelijke amorfe incubatielaag. We presenteren een techniek gebaseerd op ramanspectroscopie die het mogelijk maakt om ex-situ het profiel van de kristalfractie in nc-Si:H als functie van de laagdikte te onderzoeken. Met deze techniek laten we zien dat er verschillende groeifases bestaan tijdens de groei van nc-Si:H. Door middel van transmissie-elektronenmicroscopie (TEM) analyses hebben we vastgesteld dat de afmeting van de kristallen niet wordt beïnvloed door de entlaag. We hebben horizontale scheuren waargenomen in het begin van de groei van de nc-Si:H laag in p-i-n zonnecellen. Dit effect wordt echter verminderd door het gebruik van een entlaag. Voor de n-i-p cellen worden deze scheuren niet beïnvloed door de entlaag. Resultaten van Röntgendiffractie geven aan dat het gebruik van entlagen niet de grootte, maar wel de voorkeursoriëntatie van de kristallen beïnvloedt. Uit de externe zonnecelparameters blijkt dat het gebruik van een entlaag in p-i-n zonnecellen leidt tot een toename van het zonnecelrendement, voornamelijk als gevolg van een verhoging van de kortsluit-stroomdichtheid.

Het onderzoek naar het effect van de entlaag op de ontwikkeling van de kristalfractie wordt verder beschreven in hoofdstuk 5. Hier laten we zien dat het profiel van de kristalfractie per substraat verschilt. Bij de drie onderzochte substraten vonden we vanaf de amorfe incubatielaag een geleidelijke ontwikkeling van de kristalfractie. Bij het gebruik van een entlaag zien we een hoge

kristalfractie direct vanaf het begin van de groei, wat duidt op een snelle nucleatie. Het effect van het substraat op de ontwikkeling van de kristalfractie wordt door het gebruik van de entlaag verminderd, want alle substraten vertonen een soortgelijke ontwikkeling van kristalfractie als functie van de laagdikte.

In het laatste hoofdstuk van dit proefschrift beschrijven we hoe ramanspectroscopie gebruikt wordt om de voorkeursoriëntatie van de kristallen in nc-Si:H te bepalen. Deze voorkeursoriëntatie wordt doorgaans bepaald door middel van transmissie-elektronenmicroscopie en röntgendiffractie en kan inzicht geven in het groeimechanisme van de film. De in dit onderzoek gebruikte methode is gebaseerd op het feit dat onder gepolariseerd licht de moleculaire trillingen in films leiden tot een polarisatie-afhankelijke ramanverstrooiing die ook afhankelijk is van de kristaloriëntatie van het belichtte materiaal. We hebben deze methode getest op een reeks lagen van nc-Si:H en krijgen resultaten die vergelijkbaar zijn met de resultaten van röntgendiffractie.

List of publications related to this research

S. N. Agbo, M. Putri, R. A. C. M. M. van Swaaij, P. Sutta and M. Zeman, Investigation of crystallinity depth profile in thin film μc-Si:H on different substrates, proceedings, 26TH EUPVSEC, Hamburg, Germany, p.2653 – 2657, (2011).

S. N. Agbo, S. Dobrovolskiy, G. Wegh, R. A. C. M. M. van Swaaij, F. D. Tichelaar, P. Sutta and M. Zeman, Structural analyses of seeded microcrystalline silicon solar cell, Progress in Photovoltaic: Research and application - Under review

S. N. Agbo, R. A. C. M. M. van Swaaij, P. Sutta and M. Zeman, Preferred crystal orientation in thin-film nano-crystalline silicon determined by Raman spectroscopy, Thin Solid Films- Under review.

S. N. Agbo, J. Krč, R. A. C. M. M. van Swaaij, M. Zeman, Optimization of the p-i interface properties in thin film microcrystalline silicon solar cell, Solar Energy Materials and Solar cells 94 (2010) 1864-1868.

S. N. Agbo, R. A. C. M. M. van Swaaij, M. Zeman, Effect of seeding on the material properties of uc-Si:H layers and the spectral response on μc-Si:H solar cells, proceedings, 25TH EUPVSEC, Valencia, Spain, p.3288 – 3291, (2010).

S. N. Agbo, R. A. C. M. M. van Swaaij, M. Zeman and P. Sutta, Predicting μc-Si:H crystal orientation from Raman measurement under polarized light, Phys. Status. Solidi C 7, No. 3- 4, 708-711 (2010).

S. N. Agbo, R. A. C. M. M. van Swaaij, and M. Zeman, Effect of deposition parameters of μc-Si:H solar cell absorber layer on spectral response. Proceedings, Annual Workshop on semiconductor advances for future electronics and sensors (SAFE), Veldhoven, Netherlands (2008).

S. N. Agbo, J. Krč, R. A. C. M. M. van Swaaij, and M. Zeman, Sensitivity analysis of model parameters of μc-Si:H solar cells on textured glass/ZnO:Al substrate. Proceedings, Annual Workshop on

semiconductor advances for future electronics and sensors (SAFE), Veldhoven, Netherlands (2009).

D. Zhang, **S. N. Agbo**, M. Tijssen, R. A. C. M. M. van Swaaij, M. Zeman, Conductivity optimization of p-doped silicon layer deposition applied in HIT solar cell. Proceedings, Annual Workshop on semiconductor advances for future electronics and sensors (SAFE), Veldhoven, Netherlands (2009).

S. N. Agbo, R. A. C. M. M. van Swaaij, and M. Zeman, Sensitivity of thin film nanocrystalline silicon properties to rf PECVD parameters, *to be Submitted*.

ACKNOWLEDGEMENTS

Indeed, it has taken a journey of nearly four and half years to come to this point. It has taken not just my efforts but also the efforts and support of a number of people that I will like to appreciate and acknowledge.

First, I wish to say a very big thanks to my promoter, Prof. dr. M. Zeman for accepting me in the first place as a PhD student in his group. Thanks for the guidance and encouragements during the difficult times in the course of my PhD research. I truly gained a lot from the opportunities you gave me to attend trainings, workshops and conferences.My sincere appreciation goes to my daily supervisor and co-promoter, Dr. R.A.C.M.M. van Swaaij. Working with you was a learning process for me and I enjoyed every moment of it. We spent a lot of time discussing the results and that helped to increase my knowledge and enthusiasm about the research. Thanks for taking time to meticulously go through my thesis and for all the useful inputs. I equally appreciate Dr. Arno Smet for useful discussions. I am grateful to Martijn Tijssen, Kasper Zwetsloot, Jan Chris and Stephan Herman for always keeping the deposition facilities and the measurement equipment up and running. You were always there to give assistance with the equipment whenever you were called upon. I wish to also thank fellow PhD students in the group: Dong, Guantoa, Marinus, Klaus, Joke, Olindo, Pavel, Andrea, Mark, Lihao, Hairen, Ravi, Bas, Jimmy and all the members of the Photovoltaics Devices and Materials (PVMD) group. The team-spirit that binds us together helped me a lot. Certainly cannot forget Gijs, Michael, Karol, Janez, Rudi, Sergiy, and Serge for your friendliness and useful discussions. My regards also go to my former masters students in the group: David, Chimdi and Marinda. I am grateful to the entire staff of Delft Institute of Microsystems and Nanoelectronics (DIMES) for keeping the clean-room running and for providing training for the use of various equipment. A lot of administrative work was done in the course of my programme and for this, I want to appreciate the support of Laura, Lucy, Iris, Susy, Marysia and Marian.

My PhD studies would not have been possible if not for the fellowship I received from the Dutch Ministry of Foreign Affairs, through the Netherlands Fellowship Programme. Indeed, I am grateful to the Dutch government. My appreciation also goes to Veronique of the CICAT department of TUDelft for the day-to-day administration

of the fellowship. I appreciate the support I got from my home institute in Nigeria; National Centre for Energy Research and Development, University of Nigeria, Nsukka especially during the last few months of my PhD programme. I am particularly grateful to the former vice chancellor of University of Nigeria, Prof. Chinedu Nebo and his deputy, Prof Mosto Onuoha for providing the platform under which I was admitted into TU Delft. I am also grateful to the incumbent vice chancellor, Prof B. Okolo, and his deputy (academics), Prof I.U. Asuzu for their role in securing funding for the last four months of my stay in the Netherlands. Many thanks to the pioneer coordinator of the UNN-TU Delft linkage, Prof A.N. Nzeako, the current coordinator, Prof. D. Obikwelu and all the members of the team.

During the period of this programme, I enjoyed the support of my colleagues and friends at the Energy Research Centre, University of Nigeria, Nsukka. Though I was away, I always felt your support and encouragement each time I visited home or read your emails. I wish to say a big 'thank you' to the director, Dr P. Ugwuoke and the entire management team of the centre. I very much appreciate all your support. And to you fellow researchers and other technical, admin, accounts and all staff of the centre I say, "Chukwu gozie unu!".

I owe a lot to my mother, Justina and the rest of the members of Agbo's family and all my in-laws. Time and space will fail me to mention you all by name. Please accept my appreciation for your love and prayers for me. I really can't quantify all you mean to me. God bless you richly!

I will like to thank all the members of Mount Zion Parish of the Redemned Christian Church of God, Delft. It was always refreshing to have fellowship with you all. Thanks for your prayers and for all the support you gave me and my family these past years. Thank you Pastors Hyacinth and Helena, Jide, Sam and Chinelo Menkiti, Obioma, Tari, Clint and Naomi, Juliet, Gabriel, the Dawatolas and all the other church members. It was really nice having fellowship and doing the work of the Lord together. The relationship that exists among the African students community made a lot of difference. I express my gratitude to Austine, Sam, Sandra, Innocent, Ijeoma, Beckley, Peter, Frank, Tony, and host of you that I may not be able to mention here.

I am grateful to my home church in Nigeria, Church of God Mission, Nsukka and the Student Christian Movement, for the sound Christian tutelage I received under you. I appreciate Pastor Ogbonnaya

and his family, the Asusus, the Ubachukwus, the Ejeres, the Ugurus, the Oziokos, the chibukos, the Ekesons, the Anekes, the Ibezims, the Komolafes, the Orjis, the Okontas, the Agbajes, Eunice, Oby and the entire members of these congregations. I cannot forget the Omeje's family. You are a wonderful family.

While in Delft, myself and my family enjoyed the love of a number of our friends. Thanks to Uju Okereke for making out time to visit us in Delft. Thanks to Mr Kyrian and his family. Our Dutch neighbour, Mr. Wim, I am very grateful. You were always available each time I had need and you shared with me a lot from your experiences. Thanks to Amie for the warm African hand of fellowship you extended to us. I am also grateful to Dr. Van Nood and her family and the Janssens' family for the good relationship we shared in Delft and for providing a good atmosphere for my children to relate with yours. My friends Festus, Aniekan, Sam and Edwin, you were friends in deed. Those moments we shared together were really inspiring and I look forward for more of such times in the future.

And what do I say to you my lovely daughters: Praise, Pearl, Treasure and Goodness and my one-and-only, Oge. You give my life a meaning and I owe the completion of this work to the love, comfort, joy, understanding and succour you provided. By the grace of God, we shall share the joy of better days ahead.

To the almighty God, I give all the glory, all the honour, all praise and thanks for provision, for life, for good health, for sound mind and indeed for everything. I believe He alone brought me this far.

About the Author

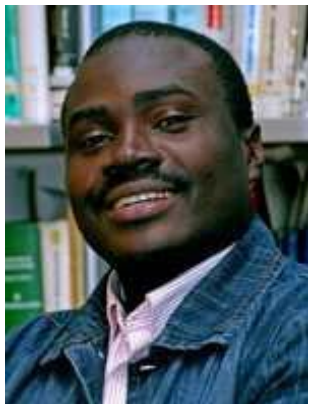

Solomon.N. Agbo was born at Nsukka, Nigeria in 1975. He had his secondary education at St. Teresa's college, Nsukka. After graduation from this college, he was admitted to the University of Nigeria, Nsukka where he studied Physics and graduated in 1999. From June, 2000 till July 2001, he took part in the compulsory one year National Youth Service in Nigeria. Within this time, he was a Physics and Mathematics teacher at a community secondary school in Rivers state, a job he enjoyed doing. In 2002, Solomon was employed as a research fellow at the National Centre for Energy Research and Development, University of Nigeria, Nsukka. His work mainly was focused on the growth of thin film semiconductors for solar application using chemical bath method and the development of solar thermal systems(water heaters and crop driers). In 2005, he obtained his Master of Science degree in Solar Energy Physics from the University of Nigeria, Nsukka. Solomon joined the prestigious Photovoltaics Materials and Devices (PVMD) group of the Delft University of Technology in 2007 as a PhD researcher to work on the MuSiC project. The MuSiC project involved the development and optimization of thin film nanocrystalline silicon materials and device for multi-junction solar cell application. This was facilitated by a research fellowship he received from the Dutch government under the Netherlands Fellowship Programme. Solomon is passionate about photovoltaic development in Africa. He is a board member of lightingnigeria, a Dutch-based NGO that promotes the use of photovoltaic technology for electricity generation in Nigeria. He is also a member of the European Union Energy Initiative for the development of photovoltaics for rural electrification in Africa.